Modeling Organ-on-Chip Microsystems:
In-device Toxicokinetics and Metabolite Detection

By

Kazi Mahmuda Tasneem

Dissertation
Submitted to the Faculty of the
Graduate School of Vanderbilt University
in partial fulfillment of the requirements
for the degree of

DOCTOR OF PHILOSOPHY
in

Chemical and Biomolecular Engineering

January 31, 2021

Nashville, Tennessee

Approved:

M. Shane Hutson, Ph.D.
Lisa J McCawley, Ph.D.
Peter Cummings, Ph.D.
Marjan Rafat, Ph.D.

Dedicated to my Creator who grows Sabr in me

ACKNOWLEDGMENTS

First of All, I pay my deepest gratitude to Almighty Allah for His graciousness, benevolence and unlimited blessings.

This research work was performed in support of the Vanderbilt-Pittsburgh Resource for Organotypic Models for Predictive Toxicology, Environmental Protection Agency (EPA) Grant 83573601, and Measuring Toxicokinetics for Organ-on-Chip Devices, EPA Grant Number 84003101.

I feel privileged to express my indebtedness and sincere thanks to my advisor Prof. M. Shane Hutson for his invaluable suggestion and guidance throughout this research work. I sincerely acknowledge the intellectual support and academic guidance of Dr. Lisa McCawley and Dr. Dmitry Markov. I would like to thank my committee members for their time and guidance. I would also like to extend my gratitude to Dr. David Cliffel and Ethan McClain for their support and collaboration for a part of my research work. I solemnly convey my gratitude to Phillip Fryman and Gloria Bazilevich for their technical assistance with experiments.

My very special thanks and gratefulness goes to my family, friends, and colleagues for their cordial cooperation and support. There is no word to thank my father and mother who believed in me, my brother Dr. Tawhid who is my life-long troubleshooter, and my sister Zeenat who is my confidante. I'm deeply indebted to my best friends Dr. Afifa and Dr. Zohra for their unconditional emotional support during my journey in grad school. Each one related directly or indirectly to this dissertation work deserves thanks for their assistance without which it would be impossible.

Last, but not the least, I am wholeheartedly thankful to my husband Dr. Baig Abdullah Al Muhit for helpful discussions and insights. His intellectual and emotional supports have been my source of inspiration to carry out the study.

TABLE OF CONTENTS

Page

LIST OF TABLES

LIST OF FIGURES

NOMENCLATURE

ATR	Attenuated Total Internal Reflection
BSA	Bovine Seram Albumin
DMSO	Dimethylsulfoxide
FTIR	Fourier Transform Infrared Spectroscopy
GOx	Glucose oxidase
LOx	Lactate Oxidase
logP	octanol/water partition coefficient
k_{cat}	Enzymatic rate constant
k_F	Forward rate constants
k_R	Backward rate constants
K_m	Michaelis Menten Constant
μCA	Microclinical Analyzer
OCM	Organ-on-chip Microsystem
PBS	Phosphate Buffered Saline
PDMS	Polydimethylsiloxane
PFA	Perfluoroalkoxy
PFOA	Perfluorooctanoic Acid
S_0	Surface carrying capacity
TPSA	Topological polar surface area
VIIBRE	Vanderbilt Institute for Integrative Biosystems Research and Education
V_{max}	Maximum rate of Michaelis Menten reaction

CHAPTER 1

INTRODUCTION

1.1. Overview and Specific Aims

Organ-on-chip microsystems (OCMs) have proven useful to evaluate chemical toxicity in human cells cultured in appropriate 3D heterotypic microenvironments. These microsystems are often fabricated from polymeric materials such as polydimethylsiloxane (PDMS), which has high affinity for small hydrophobic molecules. When potential toxicants are tested in such microdevices, hydrophobic chemicals may partition into PDMS surfaces and diffuse into the bulk PDMS and reduce the dose that reaches the cultured cells, severely impacting dose-response curves. Such chemical-PDMS interaction and undesirable sequestration of chemicals by PDMS need to be investigated for the prediction of chemicals' in-device toxicokinetics.

OCMs are advantageous for their ability to recreate physiological functions of tissues/organ in response to chemicals. Just as important as the system platform itself, are the techniques that used to analyze the metabolic functions including consumption of oxygen, glucose, and glutamate and production of lactate. The ability to accurately measure cellular uptake within OCMs is essential for identifying changes in cellular metabolism through the measurement techniques. For doing so, OCMs are also needed to be coupled with improved measurement techniques. One of the detection techniques uses electrochemical sensors based on electrical measurement against the change in metabolite concentration[1]. Such electrochemical sensing techniques developed at the Vanderbilt Institute for Integrative Biosystems Research and Education (VIIBRE) are: 1) microphysiometer, with sensor electrodes embedded with cells in the same chamber allowing *in situ* detection, and 2) microclinical analyzer (μCA), sensor chamber

placed downstream of the cell chamber allowing downstream detection. For monitoring dynamic chemical-dependent changes in variety of organ-chip systems, its integration with downstream μCA show promises, but requires detailed understanding for the downstream metabolite detection.

To address the research needs, computational approach has been taken to develop predictive models for 1) the in-device toxicokinetics of PDMS-based organ-on-chip microsystems and 2) the cellular metabolite detection using downstream microclinical analyzer. The specific aims of this work are summarized below:

Aim 1: Investigating the impact of chemical-PDMS interaction on in-device toxicokinetics in PDMS-based organ-on-chip microdevices. An experimental technique was established to measure chemical binding kinetics with PDMS and transport kinetic parameters. These parameters were used to model the in-device toxicokinetics using realistic microdevice geometry. Predictive model will be validated by experimental set ups allowing real time chemical exposure to the PDMS-based microdevices.

Aim 2: Evaluating the performance of microclinical analyzer in metabolite detection when located downstream of the organ-on-chip device. A detailed computational framework was developed for the detection of cellular metabolism using enzyme-based sensors. The goal is to model the stop-flow and continuous flow measurements with the microclinical analyzer developed at the Vanderbilt Institute for Integrative Biosystems Research and Education (VIIBRE). Details analysis of downstream detection will provide insights on the application of microclinical analyzer for assessing metabolic functions within organ-on-chip devices in response to toxic exposure.

1.2. Background and Significance

1.2.1. Organ-on-chip microsystems

Microfabricated microfluidic platform offers the opportunity to understand the cell behaviors and functionally in *in vitro* organ on chip system which allows precise control of the microenvironment surrounding the cells[2–5]. Study reveals small percentage of preclinical trials eventually approved by regulatory agencies due to the failing of the expensive late phases of clinical trials[6]. To overcome the problem of cell-based assays, organ on chip systems has gained increasing attention in pharmaceutical industries[7].

Advancements in organ-on-chip microsystems (OCMs) enable the recapitulation of the microarchitecture and functionality of the living organ tissue constructs to mimic human microenvironments[8–11]. The devices are fluidically interconnected microchambers with cultured cells and fluid medium reservoirs for drug supply, enables opportunity for drug toxicity studies. The transparent material used in manufacturing OCMs enables real-time imaging and monitoring of the cells. In order to identify the potential toxicity, drugs are allowed to flow through the micro-channels of PDMS to observe its metabolic effect on cells within the microsystem.

Such microsystems offer a platform for testing the beneficial and adverse effects of drugs, chemicals, and pharmaceuticals[12]. These microdevices include microchambers with *in vitro* on-chip cell cultures and fluid medium reservoir for continuous perfusion of nutrient media (Figure 1.1). Also, fluid flow in microfluidic channels in the vicinity of the cells allows nutrients to be delivered to the cells besides exposing them to physiologically relevant fluidic shear and flow dynamics similar to the microenvironment inside the human body. The microsystems maintain a minimum required fluid volume for tissue culture[9,13] and is capable of delivering a controlled dosage of drug compounds with organ-organ interactions to better model the human drug response,

with the goal of eventually eliminating or greatly reducing the use of animal models in drug toxicity studies and drug development[8,14]. OCMs have been used to evaluate the effects of chemicals for a variety of biological systems: e.g., liver,[15] fetal membrane,[16] neurovascular model,[17] lung,[18] mammary gland,[19] and multiorgan coupling.[20]

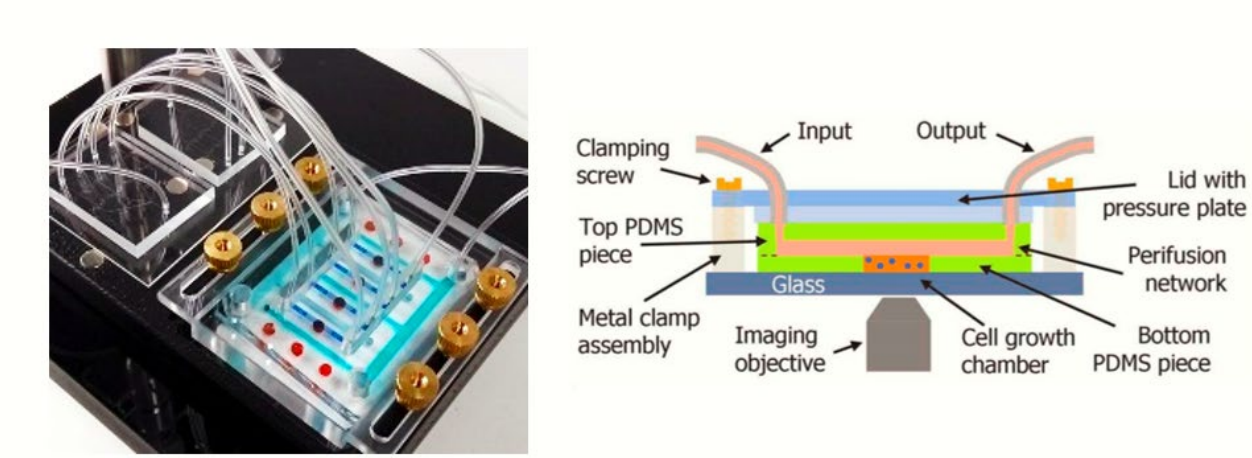

Figure 1.1 (left) mammary gland on a chip prototype. the bioreactor was filled with blue and red dyes indicating microfluidic channels (blue) and the cell chambers (red); (right) OCM indicating major components with supply network.[19]

Advances in microfabricated OCM devices have led to the design of interconnected PDMS devices that link organoids for toxicant assessment. However, the quantification of the drug or toxicant concentration, essentially exposed to the cells, are still an intrinsic challenge due to its significant adsorption onto PDMS channels[21,22]. It has several advantages including its porosity, biocompatibility, optical transparency, permeability to oxygen, and ease of fabrication.[23,24] PDMS also provides relevant mechanical stability at the sub micro-level soft tissues.[24] Devices using PDMS are becoming the preferred polymer for fabrication of microfluidic devices due to its optical transparency, gas permeability, molding properties, and ease of fabrication[24]. Additionally, rigid glass or plastic substrates do not accurately replicate the elastic environment cells encounter[25,26].

PDMS forms a porous network of linked siloxane monomers that have been shown to allow small molecules to diffuse through the bulk and has even been used as a molecular sorting material[27]

1.2.2. Chemical-PDMS interaction in organ-on-chip microsystems

Despite the convenience in its use, one obvious downside of PDMS is its hydrophobicity – a well-known tendency to bind and sequester hydrophobic compounds[19,21–23,28,29]. Potentially toxic chemicals are largely hydrophobic small molecules which binds with PDMS material surfaces.[30–32] This interaction of chemicals with PDMS results in alteration of chemical dose responses.[33] The strengths of organ-on-a-chip systems and their ability to reproduce cellular microenvironments come with this potentially problematic issue when used in chemical toxicity screening.

This potential problem is exacerbated by the small channel dimensions in such devices' microfluidic perfusion systems, which yield high surface-area-to-volume ratios. These ratios are on the order of 1-10 cm^{-1} for well-plate systems, but can range from 100-1000 cm^{-1} for organ-on-a-chip systems. The orders-of-magnitude larger relative surface area means that partitioning of a chemical into the PDMS surfaces of microfluidic channels can drastically change a chemical's concentration in the perfusing solution[34,35].

Limited studies on the absorption of chemicals by PDMS have been published for a handful of chemicals by multiple research groups[21,30,36]. PDMS absorption was first investigated by Toepke et al. by qualitative examination of absorption with fluorescent molecules[37]. They demonstrated the absorption of hydrophobic molecules in microchannels, showing how the common fluorophore Nile Red absorbed into PDMS channel walls within minutes, accumulated in the channel walls when more Nile Red was added, and remained stable and irreversibly absorbed even after repeated

rinsing. Since then, Wang et al. established a potential relationship between small molecule absorption and the octanol/water partition coefficient (log P)[36]—a measure of hydrophobicity. Van Meer et al. established a related relationship between absorption and topological polar surface area (TPSA)[30]—considered a measure of a molecule's ability to penetrate biological membranes. This major concern when using organ-on-chip devices based on PDMS is that absorption of small molecules could affect dose-response curves and estimation of Lowest Observed Adverse Effect Levels (LOAEL)[30,36], and excessive absorption and adsorption of these molecules could lead to significant bias in the interpretation of drug toxicity results. To interpret the results of toxicity studies using such chemicals, it is crucial to accurately predict their in-device toxicokinetics[34,35].

1.2.3. Computational modeling for organ-on-chip microsystems

Microfluidic OCM devices, comprised of microfluidic channels, chambers containing cells of interest, fluidic medium, fluidic reservoirs, are gaining attention in human drug toxicology studies which appears promising to eliminate the necessity of the critical clinical trial phase with animal testing. Computational Fluid Dynamics (CFD) simulation is becoming an invaluable tool to visualize and analyze the consequences of fluid flow and stresses on the cells. Moreover, computational models will hold great promise in terms of understanding the different parameters that influence cell behavior and make those more predictive. As fluid dynamic behavior, fluidic shear stresses within the micro-chambers have direct implications on cellular response and functionality, CFD has become potential candidate for the studies of microfluidic organ on chip system[38]. CFD simulation has been utilized to obtain residence time distribution of microfluidic mixers[39] and to design optimize the alveolus analog body on a chip system[5]. It has been widely accepted the laminar flow from small channels contributes to lower sheer stress and better

differentiation in an organ chip model[40]. Details of fluid mechanics, nutrient transport, and drug interaction with cells can be achieved via the use of CFD simulation.

Coupled with experimental validation, computational methods can potentially provide more realistic, predictive data sets for accurate cellular exposure within OCMs. Furthermore, prediction of fluid shear stress associated with such platform and measurements of velocity and pressure within micrometer dimensions that necessarily influence cell behavior can be theoretically analyzed; thereby, engineering design optimization can be possible at the early stage. Limited studies on modeling of chemical transport in the OCMs have been published by multiple research groups[41,42], however, to properly interpret dose-response curves from organ-on-a-chip systems, it is critical that the modeling should include the chemical-PDMS interaction, enabling accurate prediction of the chemical's in-device toxicokinetics[34,43]. This research gap was addressed in this dissertation.

1.2.4. Chemical detection techniques for cellular metabolism

Cellular metabolism is the process by which cells undergo nutrient uptake such as glucose and oxygen and convert these into energy and waste product. The waste products are, in general, acids such as carbonic acid and lactic acid. Experimental observations revealed that the rate of nutrient conversion and the rate of the acid and byproduct production are correlated. So, by studying the end-products, it is possible to monitor the nutrients. Cell metabolism consists of a large number of metabolic cycles. In the cells of mammals these include the three primary aerobic cycles: the phosphate cycle, the glycolysis cycle and the citric acid cycle[1,44]. In the glycolysis cycle, glucose and glutamine are converted to pyruvate based on the concentrations. Depending on the concentrations and reaction rates, part of the glucose is also converted to lactate. The other

two cycles involve the conversion of oxygen to water and waste products with the help of Adenosine tri-phosphate (ATP)[44,45]. The main waste products are lactic acid and carbonic acid.

This dissertation will discuss the detection of two metabolites: glucose and lactate, relevant to the metabolite cycle described above. In addition, another metabolite, glutamate, which is the principal excitatory amino acid in the central nervous system[46,47], will also be discussed.

1.2.5. Electrochemical measurement of metabolites

Since living organisms are not static systems, the ability of a measurement technique to render measurement of dynamic cellular processes in real-time is also highly desirable[48,49]. One method that is capable of meeting all these requirements is electrochemistry. Electrochemical measurements can be performed noninvasively, and for metabolites that are electrochemically active, or those that can be detected with chemically-modified electrodes, electrochemical measurements provide a relatively simplistic and rapid means with which to perform metabolic analyses[50].

Electrochemical biosensors provide a useful means to analyze the content of a living cells by the direct conversion of the chemical change into an electronic signal[51]. In the electrochemical detection technique, the measurement of electrical properties for the extraction of biological information is usually electrochemical in nature, where a bio-electrochemical component serves as the main transducing element. Although sensing devices employ a variety of recognition elements, electrochemical detection techniques use predominantly enzymes, due to their specific binding capabilities and biocatalytic activity, such as glucose oxidase (GOx) for glucose and lactate oxidase (LOx) for lactate detection[1,52,53].

Typically, the enzymatic reaction generates a measurable current (amperometric) between electrodes that is proportional to the chemical changes. Since reactions are generally detected only in close proximity to the electrode surface, the electrodes themselves play a crucial role in the performance of electrochemical sensors. These electrodes should be both conductive and chemically stable. Therefore, platinum, gold, carbon (e.g., graphite) and silicon compounds are commonly used, depending on the analyte[51]. Sometimes surface modification is necessary for improved detectability and the prevention of biofouling[1,44,51].

Electrochemical sensing usually requires a combination of reference electrode/ counter (inert) electrode and a working electrode as sensing or redox electrode. The reference electrode, commonly made from Ag/AgCl, is kept at a distance from the reaction site in order to maintain a known and stable potential. The working electrode serves as the transducer for measuring the current changes due to the enzymatic reaction, while the counter electrode establishes a connection to the electrolytic solution so that a current can be applied to the working electrode. With such a three-electrode setup, the output of the electrochemical sensor is the current for an applied electric potential.

One of the widely used electrochemical sensors are amperometric glucose sensors. In a glucose sensor, an enzyme acts as catalyst for recognizing the glucose molecules. These enzyme molecules are located on an electrode surface, acting as transducer. As soon as the enzyme recognizes the glucose molecules, it catalyzes to produce gluconic acid and hydrogen peroxide from glucose. The electrodes consume the electrons transferred due to hydrogen-peroxide oxygen coupling. The resulting electron flow is proportional to the peroxide concentration which is proportional to the glucose present in the fluidic phase. More detailed working principle of enzyme-based sensor will be discussed in Chapter 4. Such enzyme-based electrochemical sensors

offer capabilities to monitor metabolic dynamics in near real time with analytical data as a function of analyte concentration and exposure time.

1.2.6. Microphysiometer vs microclinical analyzer

Upon chemical exposure, cells inside the organ-on-chip devices undergo metabolic changes including consumption of oxygen and glucose, and production of lactate and glutamate.[48] Understanding of these complex biological processes can be gained through experimentally accessible electrochemical sensing devices.[1,46,54] Microphysiometry provides a non-invasive means for electrochemically measuring the change in metabolite concentration in real time. In a microscale platform, small sample volume (few microliters) enhances the sensitivity of small metabolic changes.[1,46,54] Examples of such analytical devices include electrochemical measurement technique using microphysiometer and microclinical analyzer.

For real-time monitoring of the cellular responses, two different measurement devices can be coupled with cell chambers- 1) microphysiometer with sensor electrodes embedded with cells in the same chamber allowing in situ detection and 2) microclinical analyzer (μCA) with sensor chamber placed downstream of the cell chamber allowing downstream detection (Figure 1.2). A significant effort has been put forward to designing chemical sensors that can be integrated within the OCMs. In such microfluidic platform, microphysiometer is already well suited to the application of in-situ measurement techniques that can provide high resolution data due to change in cellular microenvironment within OCMs[46,54–57]. On the other hand, μCA is advantageous for being adjustable to variety of cell culture constructs with easy pumping and valve systems.[1] Therefore, in an effort to evaluate the performance of downstream measurement using μCA, a detailed computational approach has been taken.

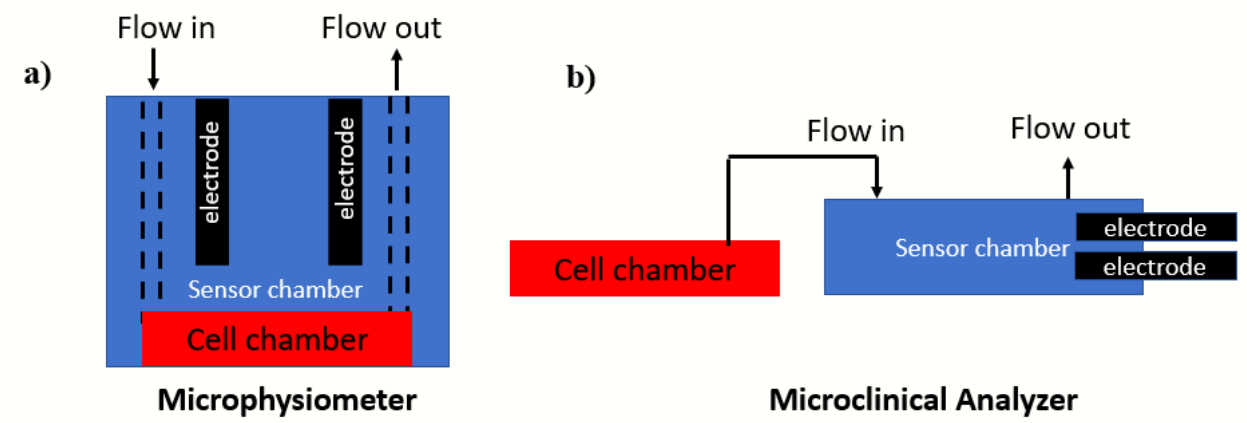

Figure 1.2 Simple schematic of different arrangement for metabolite detection – a) in-situ detection: microphysiometer where cells and sensor electrodes are colocalized, yielding improved temporal and spatial resolution of detection; b) downstream detection: μCA where cells and sensor electrodes are located in adjacent separate chambers, providing flexibility of assembling with variety of cell types in microfluidic devices

The microphysiometer is capable of real-time electrochemical analysis through the enzymatic modification of a sensor electrode that could be placed within a microfluidic chamber containing a cell-coated transwell[48,54]. This platform has the ability to plug in enzymatically modified electrodes to the microfluidic cell chamber – allowing for flexibility in analyte detection. While platform utilizing such in situ detection provide a high temporal and spatial resolution, their design and assembly can be complex and system specific dedicated to one cell-type chamber. Thus, the development of downstream detection platform compatible with variety of OCMs with different cell-types could provide versatility of chemical and metabolite detections.

Downstream detection refers to real-time chemical analysis of an OCM by the direct connection of the OCM with the detection method. Some detection platforms, such as μCA, are designed to allow for integration with variety of OCM devices with easy pumping and valve systems[1] (see Figure 1.3). The downstream electrodes can be easily accessible for enzyme modification, providing flexibility in analyte detection, such as, glucose, lactate, glutamate, etc.

the platform can be coupled with any microfluidic OCM device by the use of tubing systems to perfuse over the electrode within the OCMs. However, the metabolite detection downstream of the OCMs in this manner poses some challenges, as effluent may be affected by the diffusional mixing while perfusing with lower flow rates – compromising the resolution of the collected data.

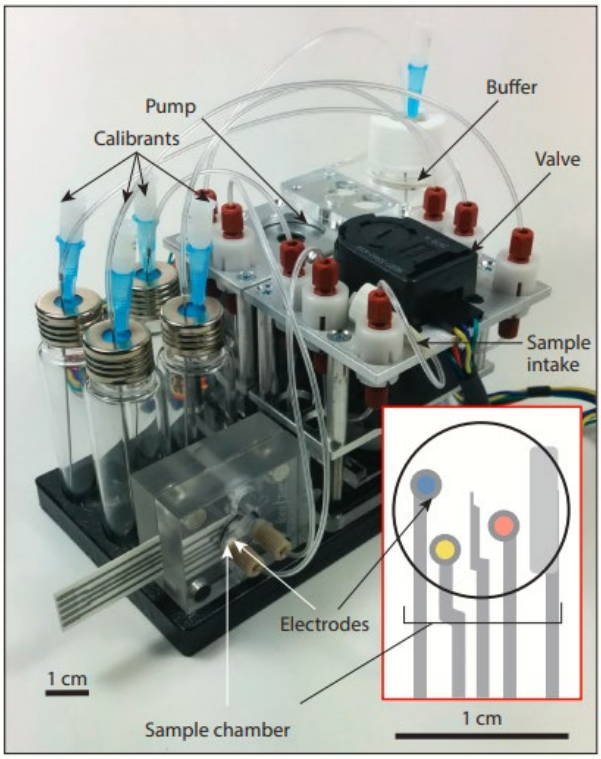

Figure 1.3 Microclinical analyzer with pump and valve together to flow 26 µL of buffer, calibrants, and/or sample into the sample chamber containing the electrodes. (inset) schematic of a screen-printed electrode.[Courtesy of Davis et al (2017)[1]

Despite its flexibility and ease of use, microclinical analyzer's distant coupling between the sensor chamber and the cell chamber may hinder instantaneous detection, compromising the temporal and spatial resolution. To evaluate the time-dependent chemical detection using microclinical analyzer, it is critical to understand the chemical transport and kinetics around the cells and sensor electrodes. This investigation will guide whether we should consider

implementing a biosensor module with downstream detection instead of the conventional *in situ* one.

Besides the development of cellular microenvironments of human tissue or organs using OCMs, its ability to monitor and analyze the real-time cellular responses to drug and toxicants are critical. For this reason, coupling of monitoring tools or devices with wide variety of OCMs are essential for the successful application of such organoid models. In this context, this dissertation focused on the implementation of miniaturized electrochemical sensors integrated in-line with the OCMs for the real-time measurement of cellular responses to the chemical exposure.

1.3. Organization of the Dissertation

Apart from this chapter, the remainder of the dissertation has been divided into four chapters. Chapter 2 presents both experimental approach and computational modeling for toxicokinetics of chemical-PDMS interaction and its impact on organ-on-chip microsystems. The experimental technique has been established to measure chemicals' PDMS-binding kinetics and to use these measured kinetic parameters to model chemical transport in PDMS- based devices for the prediction of time-dependent cellular exposures.

Chapter 3 discusses how the toxicokinetic model can be developed further to validate the actual microsystem platform, including an extended modeling approach and its validation under different experimental conditions. This chapter also includes preliminary experimental observation and discusses about the lesson learned that would be useful for future experimental plans.

Chapter 4 presents the details of the computational framework developed for modeling enzyme-based electrochemical sensors, including numerical technique to extract enzymatic kinetic parameters. The modeling approach provide insights on how cells consumed chemicals inside and

chamber, and the change in concentration can be predicted by downstream chemical sensor microclinical analyzer.

Finally, Chapter 5 summarizes the major conclusions of the study and also provides recommendations for the further study. Attempts are made to draw conclusions from various findings of the study and recommendations provide a basis of further study.

CHAPTER 2

PREDICTION OF TOXICOKINETICS IN ORGAN-ON-CHIP MICROSYSTEMS

Published Article:

Auner, A.W.*, Tasneem, K.M.*, Markov, D.A., McCawley, L.J., and Hutson, M.S., "Chemical-PDMS binding kinetics and implications for bioavailability in microfluidic devices," *Lab on a Chip*, 2019, *equally contributed first authors. This chapter presents both experimental approach and computational modeling for toxicokinetics of chemical-PDMS interaction and its impact in organ-on-chip microsystems. Part of the experimental work including majority of the chemical analysis and molecular property investigations were solely the contribution of Auner, A.W.

2.1. Abstract

Microfluidic organ-on-chip devices constructed from polydimethylsiloxane (PDMS) have proven useful in studying both beneficial and adverse effects of drugs, supplements, and potential toxicants. Despite multiple advantages, one clear drawback of PDMS-based devices is binding of hydrophobic chemicals to their exposed surfaces. Chemical binding to PDMS can change the timing and extent of chemical delivery to cells in such devices, potentially altering dose-response curves. Recent efforts have quantified PDMS binding for selected chemicals. Here, we test a wider set of nineteen chemicals using UV-Vis or infrared spectroscopy to characterize loss of chemical from solution in two setups with different PDMS-surface-to-solution-volume ratios. We find discernible PDMS binding for eight chemicals and show that PDMS binding is strongest for chemicals with a high octanol-water partition coefficient (LogP > 1.85) and low H-bond donor number. Further, by measuring depletion and return of chemical from solution over tens to

hundreds of hours and fitting these results to a first order model of binding kinetics, we characterize partitioning into PDMS in terms of binding capacities per unit surface area and both forward and reverse rate constants. These fitted parameters were used to model the impact of PDMS binding on chemical transport and bioavailability under realistic flow conditions and device geometry. The models predict that PDMS binding could alter in-device cellular exposures for both continuous and bolus dosing schemes by up to an order of magnitude compared to nominal input doses.

2.2. Introduction

Microfluidic organ-on-chip devices have proven useful in studying both beneficial and adverse effects of drugs, supplements, and potential toxicants through improved response times and reduced costs in bioactivity screens.[58] Such devices have also been used to investigate chemical effects in models for a range of biological systems and processes: e.g., mammary glands;[59] lungs;[60] hepatotoxicity;[61] renal differentiation;[62] and multi-organ coupling.[63] The primary polymer used to fabricate microfluidic devices has been polydimethysiloxane (PDMS). The advantages of PDMS range from its optical transparency to its gas permeability to its ease of fabrication.[64] In addition, compared to rigid glass or plastic substrates, PDMS-based devices provide cultured cells with a more porous and less stiff mechanical environment – still artificial, but closer in mechanical properties to soft tissues.[25,26]

Despite these advantages, one clear drawback of PDMS is its hydrophobicity. This disadvantage is particularly worrisome in chemical screening applications because hydrophobic compounds can bind to or become sequestered within PDMS. Such binding causes a discrepancy between the nominal inlet concentration and actual cellular exposures,

affecting dose-response curves.[33] The aims of this study are to characterize those chemical properties that are predictive of PDMS binding, to present a simple protocol for experimentally measuring the on- and off-rate PDMS-binding kinetics, and to show how the measured kinetic parameters can be used to model chemical transport in PDMS-based devices to predict and/or design actual cellular exposures.

The binding and sequestration of hydrophobic compounds by PDMS was first investigated qualitatively using fluorescent molecules.[19,21] Subsequent quantitative studies suggested relationships between a compound's degree of PDMS binding and its octanol/water partition coefficient (LogP) or its topological polar surface area (TPSA). One study suggested a LogP threshold – strong binding for highly hydrophobic compounds with LogP > 2.62.[36] The follow-up, which only tested compounds above the LogP threshold, suggested a linear correlation of stronger binding with smaller TPSA.[30] These two studies were limited to evaluation of just 5 and 4 compounds, respectively. To further investigate the link between molecular properties and chemical partitioning into PDMS, we have chosen a larger, more diverse sample of 19 test compounds. These chemicals have a range of uses – from pesticides to pharmaceuticals to the manufacture of consumer products – and were selected due to their use in current organ-on-chip toxicology studies. As detailed in Table 2.1, many of the test compounds have been linked to endocrine disruption and developmental or reproductive toxicity; others serve as negative controls with no known toxicity in mammals.[11-39] To interpret the results of toxicology studies using these compounds in PDMS-based microfluidic devices, it is crucial that we can accurately predict their in-device bioavailability.

Table 2.1 Commercial use and toxicity references for chemicals tested here

Chemical name	Use	Toxicity in mammals	Ref.
Perfluorooctanoic acid (PFOA)	Teflon™ manufacturing	endocrine disruptor	65–72
Bisphenol A	Plastic manufacturing	endocrine disruptor	65,73–81
Diethylstilbestrol	Synthetic non-steroidal estrogen	endocrine disruptor	82
Genistein	Pharmaceutical/supplement	endocrine disruptor	83–86
Secoisolariciresinol diglucoside (SDG)	Pharmaceutical/supplement	non-toxic	87
Doxorubicin	Chemotherapy	cytotoxic	88
Docetaxel	Chemotherapy	cytotoxic	88
Rhodamine B or 6G	Chemical dye	cytotoxic	89,90
Propiconazole	Fungicide	reproductive	65
Aminopyralid	Herbicide	developmental	91
Molinate	Herbicide	reproductive	65,92
Ethofumesate	Herbicide	non-toxic	93
Imazaquin	Herbicide	non-toxic	91
Hexazinone	Herbicide	reproductive	91
Foramsulfuron	Herbicide	non-toxic	91
Sulfentrazone	Herbicide	reproductive	65
Acetamiprid	Insecticide	reproductive	65
Formetanate	Insecticide	neurotoxin	91

Such predictions will rely on computational models. Here we provide a simple method for measuring the needed model parameters for reversible and irreversible PDMS-binding kinetics. These include the forward and backward rate constants, as well as chemical-specific carrying capacities per unit of PDMS surface area. Previous approaches to this problem explicitly modelled diffusional transport of chemicals within PDMS;[34] however, we find that the combined effects of partitioning at the solution-PDMS interface and diffusion into the PDMS bulk are well described by rate constants and carry capacities over tens to hundreds of hours. For all but one tested compound, we used time-resolved UV-Vis absorption spectroscopy to monitor depletion (and later return) of chemical from (to) a solution in contact with either a PDMS disk or the walls of a PDMS microfluidic channel. The exception was perfluoorooctanoic acid (PFOA), which had insufficient light absorption within an accessible UV-Vis spectral window. As an alternative, we measured PFOA's infrared absorption in attenuated total reflectance (ATR) mode to directly measure

its accumulation on PDMS surfaces. Once the binding parameters are measured, we then present a model that combines computational fluid dynamics (CFD) with PDMS-binding kinetics to predict chemical bioavailability in a simple microfluidic device. These predictions include temporally- and spatially-varying chemical concentrations in the perfusion media, as well as the effective surface density of bound chemical throughout the device. We use this model to highlight what typical PDMS-binding parameters imply for bioavailability. Our approach complements prior work that focused on microfluidic design considerations for minimizing the impact of sequestration in PDMS.[34] These design considerations depended on the properties of the chemicals to be tested – *e.g.*, partition and diffusion coefficients – and are thus not as useful when designing a single microfluidic system to test a wide range of drugs or potential toxicants. Explicitly modeling bioavailability for each chemical is thus a key step towards pharmacokinetics for organ-on-chip or microphysiological systems.

2.3. Experimental design

2.3.1. PDMS preparation

PDMS Sylgard 184 (Dow Corning, Auburn, MI) was mixed with a 1:10 weight ratio of curing agent to elastomer. For disk-soak experiments, PDMS was cast in a 5-mm thick layer, cured for 24 hours, and cut into cylindrical disks (6-mm in diameter). For channel-soak experiments, PDMS was cast in a 3-mm thick layer over a channel mould, which was fabricated using standard photolithography on a Si wafer with SU8-2050 photoresist. After curing the PDMS for 24 hours, inlets were formed by punching 1.5-mm diameter cylindrical reservoirs at both ends of the channel. To reversibly seal channels for long-duration chemical exposures, channel-containing PDMS

layers were sandwiched between two other 3-mm thick PDMS layers and subjected to continuous pressure from a weighted plate. Channel dimensions are given in Figure 2.1B.

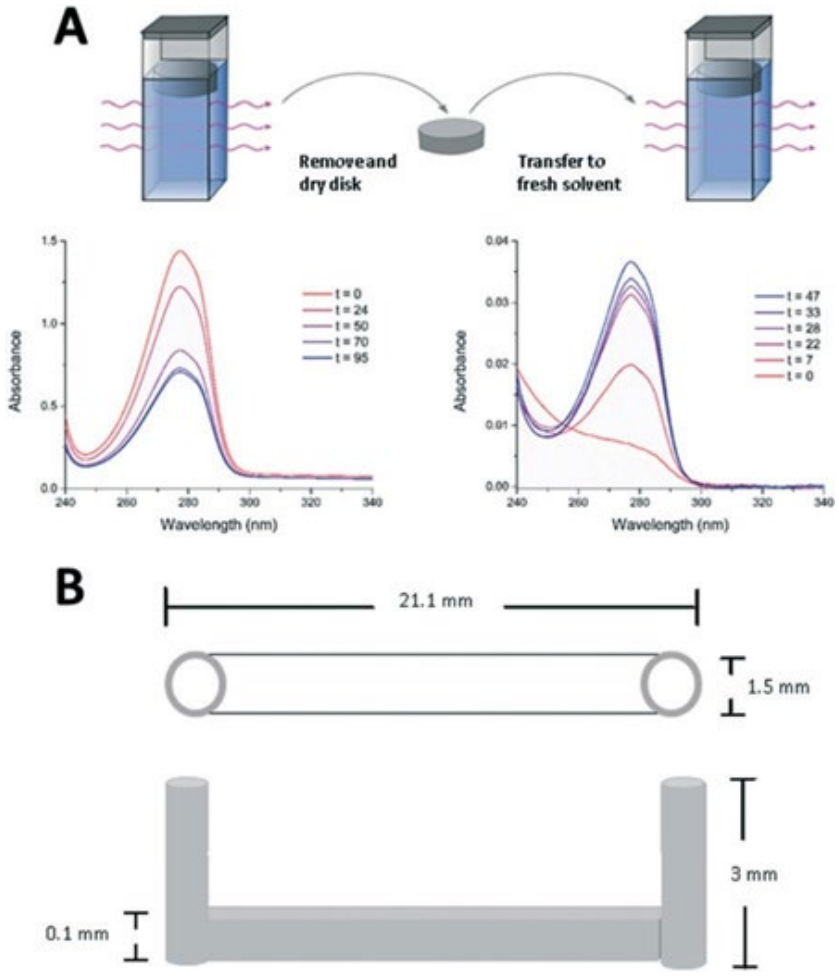

Figure 2.1 PDMS-binding and desorption experiments with example spectra for ethofumesate. (A-left) UV-vis spectra showing depletion of ethofumesate from bulk solution as it partitions into a PDMS disk floating in the cuvette. (A-right) UV-vis spectra showing return of ethofumesate to bulk solution as it desorbs into fresh solvent from a pre-soaked PDMS disk. (B) Dimensions of the microfluidic channel used in channel-soak experiments.

2.3.2. Chemical preparation

All chemicals were purchased in powder form (except liquid molinate) from Sigma Aldrich (Saint Louis, MO). Chemicals to be tested were dissolved in either molecular biology grade water or a 1X phosphate buffered saline (PBS) solution with added dimethyl sulfoxide (DMSO) to

increase solubility of hydrophobic compounds (LogP >1). For most chemicals, the final DMSO fraction was 0.1%, but 10% was used for docetaxel. Chemicals were diluted in their respective solvent to starting concentrations that yielded a peak UV-Vis absorbance of one or as close as solubility allowed. Molecular properties cited here were from the EPA Chemistry Database,[91] Canadian Institute of Health Toxin Database,[94] University of Hertfordshire Pesticide Properties Database,[95] and select publications for genistein.[96] For most chemicals, cited LogP values were from database-reported experimental measurements; for three chemicals (PFOA, formetanate, and SDG) experimental values were not available and we instead cite database-reported values for calculated LogP (cLogP).

2.3.3. Assessing PDMS binding via UV-vis measurements

For disk-soak experiments, we conducted both on- and off- rate experiments. On-rate experiments were designed to measure the rate at which each chemical partitioned out of solution and onto or into a PDMS disk. In brief, each sample solution was placed in a 4-ml quartz cuvette and a PDMS disk was carefully placed on the surface. Due to the relative densities of water and PDMS, such disks float with a reproducible volume above and below the surface. Cuvettes with disks were placed on an orbital shaker to keep solutions well mixed. Periodically, cuvettes were moved to a UV-vis spectrometer to have spectra measured with disks still floating above the spectrometer light beam (Figure 2.1A). Chemical binding to the floating PDMS disk was tracked via depletion of chemical from solution. At the end of an on-rate experiment, if there was evidence of chemical binding to the PDMS disk, then the disk was removed from its sample-solution cuvette, dried with gaseous nitrogen, and carefully floated on the surface of fresh solvent in a new cuvette (Figure 2.1A). Shaking and periodic UV-vis measurements were then performed as above

to conduct an off-rate experiment that tracked the rate at which surface-bound chemical partitioned back off the PDMS disk and into solution.

UV-vis absorbance spectra for on- and off-rate experiments were measured against matched cuvettes with appropriate solvent using a Cary 5000 dual-beam UV-vis spectrometer (Agilent, Santa Clara, CA; scan rate = 24 nm min^{-1}; resolution = 1 nm). To control for chemical stability, spectra were also measured periodically for positive control cuvettes containing sample solutions without PDMS disks. To correct for instrumental baseline drift, spectra were concomitantly measured for negative control cuvettes containing appropriate solvent only.

For channel-soak experiments, each channel was filled with a chemical solution and pressure-sealed against other PDMS layers. After a predetermined soak time, the channel was opened, the chemical solution was pipetted out, and its UV-vis spectrum was measured using a Nanodrop 2000C spectrophotometer (Thermo Fisher, Waltham, MA). Time-resolved measurements were thus obtained by sealing individual channels for different periods of time. Each time-point measurement was repeated in triplicate.

To convert UV-vis absorbance to chemical concentration, a clearly discernible peak of interest was selected from spectra of each chemical at several dilutions and used to construct a linear calibration curve (measured independently for each spectrometer and in triplicate for each chemical).

2.3.4. Assessing PDMS binding via FTIR measurements

The UV-vis absorption band for one tested chemical, PFOA, was too near the edge of UV detection for reliable measurement. As an alternative, we took IR spectra to measure PFOA bound to PDMS disks using a Nicolet IS5 FTIR spectrometer (Thermo Fisher, Waltham, MA) with a

single-reflection diamond ATR attachment. Measurements were averaged 100 times with a resolution of 4 cm^{-1} and with the evanescent wave covering a 1.5-mm diameter area. For these measurements, PDMS disks were floated as detailed above in a solution of PFOA for 48 hours, removed from solution, dried with nitrogen, and placed directly onto the diamond ATR. Both PFOA-soaked disks and control solvent-soaked disks were measured in triplicate to confirm homogeneity of surface binding. Since FTIR spectra were measured at a single time point, they were only used to estimate the amount of PFOA bound and not its binding kinetics. To convert from IR absorbance to concentration, we used the strong PFOA vibrational mode at 1209 cm^{-1}, which corresponds to a (CF_2) + (CF_3) asymmetric stretch,[97] and measured calibration spectra of diluted PFOA solutions in pure DMSO. The contribution of PDMS to FTIR spectra of soaked disks was minimized by weighted subtraction of a spectrum of a control solvent- soaked disk and a constant baseline offset, with weights determined by least squares minimization of the resultant spectrum in a region with no PFOA vibrational bands (990–1040 cm^{-1}).

2.3.5. Computational model

Modelling of chemical transport in a microfluidic device, including binding and desorption from PDMS surfaces, was conducted using COMSOL Multiphysics (Burlington, MA). The modelled geometry was a single longitudinal plane through a simple rectangular microchannel (length = 8 mm, width = 1.5 mm, and height = 0.1 mm). Since channel width was much greater than height, variations in velocity and concentration along the channel width were neglected and a well-developed parabolic flow velocity was imposed vertically. Symmetry allowed for a reduction in computation time by explicitly modelling only the bottom half of the channel. Conditions were assumed to be isothermal, with convective flux boundary conditions specified at

both device inlet and outlet. The model scheme was validated by simulating disk-soak experiments under well-mixed conditions to reproduce the experimental binding and desorption kinetics.

2.4. Results

The primary method used here to measure chemical binding to PDMS was quantifying the loss of chemical from a solution in contact with a PDMS disk or channel surface using UV-Vis absorbance (Figure 2.1). Control experiments on matched solutions without PDMS disks confirmed that all but one tested chemical had no significant PDMS-independent loss from solution. That exception was molinate, likely due to its high volatility.[95] Its loss from control samples was measured and its binding to PDMS was assessed as the excess depletion observed in disk-soak experiments.

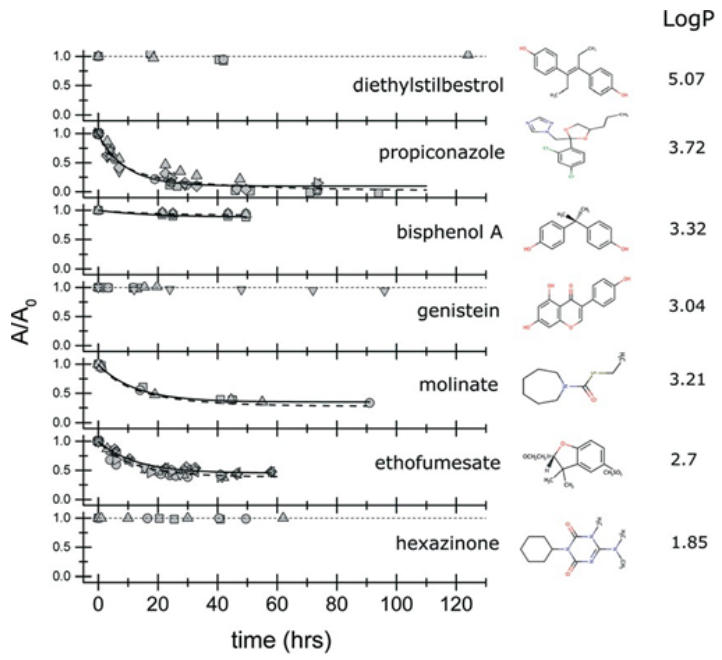

Figure 2.2 Time-dependent depletion of selected chemicals from bulk aqueous solutions in PDMS disk-binding experiments. *A*/*A*0 = fraction remaining. Results ordered via descending logP (listed beside each chemical structure). Data points with different symbols indicate different sample replicates. Solid lines are best fits to an empirical description (Equation 2.1); dashed lines are fits to a microscopic model for binding kinetics (Equation 2.3b). Dotted lines show a normalized value of 1.0 for chemicals with no discernible depletion.

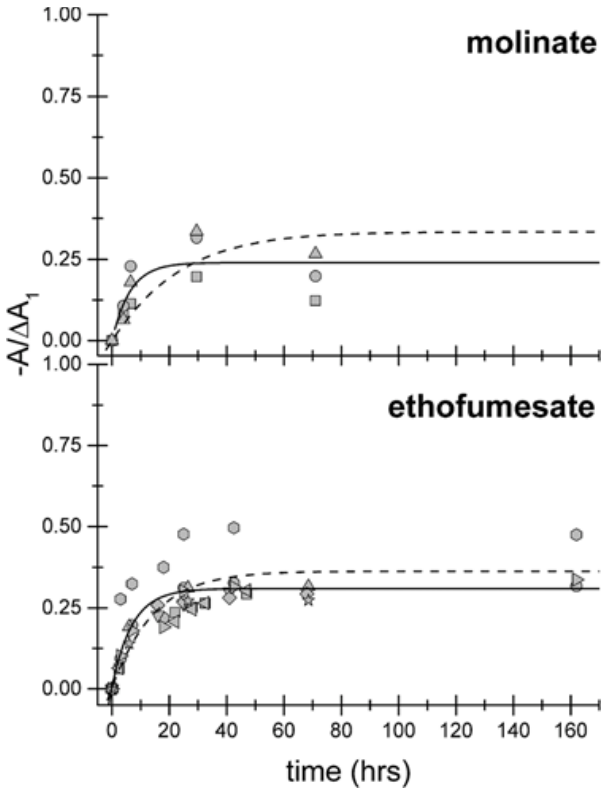

Figure 2.3 Time-dependent return of chemicals into bulk aqueous solution via desorption from previously-soaked PDMS disks. Different symbols denote different sample replicates. Solid lines are best fits to an empirical description (Equation 2.2); dashed lines are fits to a microscopic model of binding kinetics (Equation 2.3b). Concentration is normalized to the amount depleted from solution, and thus bound to the disk, in the previous soaking experiment ($\Delta A1 = -44.4$ μM for ethofumesate; −53 μM for molinate).

In disk-soak experiments, we observed no PDMS binding for any tested chemical with logP < 2.5. On the other hand, four of the seven most hydrophobic chemicals tested in these experiments were lost from solution following exponential decays over tens of hours – see Figure 2.2 for molinate, ethofumesate, propiconazole, and to a lesser degree, bisphenol A. This behavior was not universal: other hydrophobic chemicals with logP > 2.5, such as diethylstilbestrol, genistein and rhodamine 6G, showed no evidence of depletion from solution and thus no binding to PDMS. The most hydrophobic compound tested, PFOA, had no appropriate UV-vis absorption, which precluded measuring its binding kinetics, but we were able to measure the degree to which

it bound PDMS at a single time point using ATR-FTIR spectroscopy. We found that 24% of the PFOA originally in solution had bound to the surface of a PDMS disk after soaking for 48 hours.

When pre-soaked PDMS disks were transferred to fresh solvent, we found that two tested chemicals desorbed from PDMS and returned to solution: molinate and ethofumesate. As shown in Figure 2.3, their desorption followed a roughly exponential approach to a new equilibrium between bound and free chemical. Molinate never reached a steady level, but instead appears to decrease after 40 hours because the correction for its PDMS-independent loss could not be implemented for off-rate experiments. Nonetheless, about 1/4 and 1/3 of the molinate and ethofumesate bound to a PDMS disk respectively returned to solution within 48 hours. The other two chemicals for which we could measure PDMS- binding kinetics, namely propiconazole and bisphenol A, bound irreversibly with no evidence of desorption in fresh solvent.

To empirically quantify the PDMS-binding kinetics of each chemical, we fit the disk soak results to exponential approaches to equilibrium:

$$A = A_0 + \Delta A_1(1 - e^{-t/\tau 1}) \qquad \text{(Equation 2.1)}$$

$$A = \Delta A_2(1 - e^{-t/\tau 2}) \qquad \text{(Equation 2.2)}$$

Equation 2.1 fits experiments in which an initial amount of chemical A_0 is depleted from solution with time constant τ_1 to approach a final value of $A_0 + \Delta A_1$ (in which $\Delta A_1 < 0$). Equation 2.2 similarly fits experiments in which an amount of chemical $\Delta A_2 > 0$ returns to solution as it desorbs from a pre-soaked disk with time constant τ_2. For each chemical that bound PDMS, Table 2.2 lists the time constants (τ_1, τ_2), the fraction bound at equilibrium, $f_{B,eq} = -\Delta A_1/A_0$, and the fraction eventually returned to solution, $\Delta A_2/A_0$. The "fraction bound" is also listed for chemicals that did not exhibit significant loss from solution for which it is based solely on the percent change

in concentration between the start and end of experiments. Some of the non-binding chemicals have experimentally estimated values of $f_{B,eq}$ that are negative, but these are all within a few standard deviations of zero. Note that these are empirical descriptors specific to the stated experimental conditions.

Notably, rhodamine B did not show significant binding to PDMS in disk-soak experiments despite visibly dying the disk surface. Since rhodamine B has a high extinction coefficient, this visible dying could result from a very small amount bound. To quantify binding for chemicals like rhodamine B that partitioned into PDMS to a lesser extent, we thus conducted additional experiments in which solutions were sealed inside a microfluidic channel (dimensions as in Figure 2.1). These channel-soak experiments had a much larger surface-to-volume ratio (116 cm^{-1} *versus* 0.3 cm^{-1}), which allowed detection of less extensive binding. Results from both types of experiments are compared in Table 2.2. Due to the shorter effective pathlength of the Nanodrop spectrophotometer, several chemicals had too little absorbance even at their solubility limit to have their PDMS binding measured using channel-soak experiments (diethylstilbestrol, propiconazole, molinate, ethofumesate, docetaxel).

Table 2.2 Summary of key molecular properties, experimental details and results for all chemicals tested: N = number of sample replicates; A_0 = initial chemical concentration; $f_{B,eq}$, ΔA_1, τ_1, ΔA_2, τ_2 from empirical fits to Equation 2.1 and Equation 2.2 as defined in main text. Experiments not conducted and parameters that could not be estimated marked by dashes. The PDMS-surface-to-solution-volume ratio α is noted for each class of experiments

				Disk-soak experiments(α=S/V=0.3 cm^{-1})						Channel-soak experiments(α=S/V=116 cm^{-1})						
Molecular properties				Expt. detail	Empirical fit parameters					Expt. detail	Empirical fit parameters					
Chemical name	log *P*	TPSA (Å^2)	H-Bond donors	N	A_0 (μM)	$f_{B,eq} = -\Delta A_1/A_0$	τ_1 (h)	$\Delta A_2/A_0$	τ_2 (h)	N	A_0 (μM)	$f_{B,eq} = -\Delta A_1/A_0$	τ_1 (h)	$\Delta A_2/A_0$	τ_2 (h)
PFOA	6.3	37.3	1	5	589	26 ± 4%	—	—	—	—	—	—	—	—	—
Rhodamine 6G	5.2	59.9	2	3	20	1.7 ± 0.3%	—	—	—	5	189	8 ± 3%	—	—	—
Diethylstilbestrol	5.07	40.5	2	3	89	4 ± 3%	—	—	—	—	—	—	—	—	—
Propiconazole	3.72	49.2	0	9	336	90 ± 2%	9.7 ± 1	—	—	—	—	—	—	—	—
Bisphenol A	3.32	40.5	2	3	97	8 ± 2%	17.6 ± 1	—	—	3	488, 3100	78 ± 1%	3.12 ± 0.03	11.8 ± 2%	0.2 ± 0.2
Genistein	3.04	87.0	3	3	38	1 ± 1%	—	—	—	3	38	4 ± 4%	—	—	—
Molinate	3.21	45.6	0	3	113	50 ± 10%	13.6 ± 2	12 ± 2%	6.1 ± 1	—	—	—	—	—	—
Ethofumesate	2.7	70.2	0	9	75	59 ± 4%	11.3 ± 1	19 ± 1%	11.0 ± 2	—	—	—	—	—	—
Docetaxel	2.40	224.0	5	3	12	−0.1± 0.8%	—	— —	—		—	—	—	—	—
Rhodamine B	1.95	52.8	1	3	10	2.05 ± 0.05	—	— 3	—		177	80 ± 5%	2.6 ± 0.7	5 ± 2%	1.5 ± 0.8
Imazaquin	1.86	91.6	2	3	17	−1.0± 0.4%	—	—	—	3	16	13%	3.5 ± 0.8	—	—
Hexazinone	1.85	56.2	0	3	40	1.1 ± 0.6%	—	—	—	3	40	37 ± 7%	2.8 ± 0.6	—	—
Doxorubicin	1.27	206	6	3	60	6 ± 1%	—	—	—	2	60	5 ± 8%	—	—	—
Sulfentrazone	0.99	90.5	1	3	26	−1.1± 0.6%	—	—	—	2	26	−8.00 ± 0.02%	—	—	—
Acetamiprid	0.8	52.3	0	3	45	0.1 ± 0.1%	—	—	—	2	45	−1 ± 8%	—	—	—
Formetanate	0	53.9	2	3	39	−2 ± 3%	—	—	—	2	39	−9 ± 3%	—	—	—
Foramsulfuron	−0.78	177.0	3	3	32	−0.8 ± 0.2%	—	—	—	2	32	7 ± 3%	—	—	—
Aminopyralid	−2.87	76.2	2	3	50	−2 ± 1%	—	—	—	3	50	−14 ± 7%	—	—	—
SDG	−2.93	258	10	3	58	0 ± 3%	—	—	—	2	58	11 ± 9%	—	—	—

Between the two sets of experiments, nine chemicals in our test set measurably bound to PDMS: PFOA, rhodamine 6G, propiconazole, bisphenol A, molinate, ethofumesate, rhodamine B, imazaquin and hexazinone. All had high logP (≥1.8) and low TPSA (≤91.6 $Å^2$). These results are consistent with data from two previous studies by Wang *et al.* and Van Meer *et al.* that linked PDMS absorption to measures of high hydrophobicity.[30,36] On the other hand, our larger test set identified several chemicals with similarly high logP and/or low TPSA that did not measurably bind to PDMS, *e.g.*, diethylstilbestrol and genistein (logP of 5.07 and 3.04 respectively; see Table 2.2). We thus investigated whether any additional molecular property would distinguish the hydrophobic non- binders. The only combination we found that discriminated binders from non-binders was logP and the number of H-bond donors. This discrimination is shown in Figure 2.4A and B, which separately compare results for disk-soak experiments and channel-soak experiments. Previous studies had surface-to-volume ratios closer to our channel-soak experiments and are thus reported alongside those results in Figure 2.4B. Whenever there was a discrepancy in reported logP values, we plotted data points at both values and connected them with a horizontal line. There is clearly a threshold logP (in the range of 1.27–1.85), below which chemicals do not bind PDMS. Above this threshold, chemicals may bind PDMS, but the strength of this binding decreases for molecules having more H-bond donors. An exception to this trend was rhodamine 6G as tested by Wang *et al.*[36] We tested rhodamine 6G in both our experimental setups and found very little binding to PDMS. This discrepancy will be revisited in Discussion.

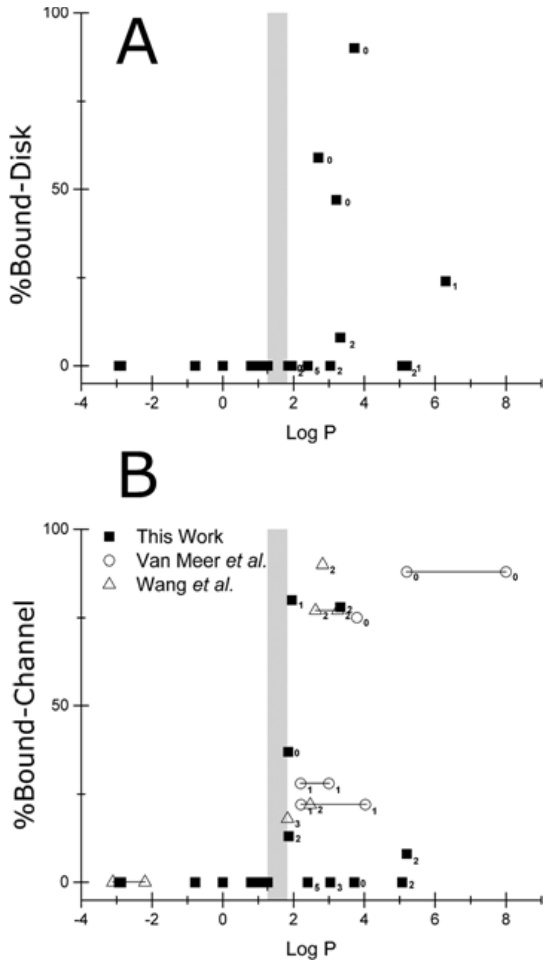

Figure 2.4 Correlation of PDMS binding affinity (% Bound) with chemicals' LogP and number of H-bond donors (subscript). Shaded region represents the LogP threshold for significant chemical absorption. (**A**) Disk-soak experiments. (**B**) Channel-soak experiments reported in this work (■), in van Meer *et al.*[43] (○), or in Wang *et al.*[42] (△). Data points connected with horizontal lines denote discrepancies in reported LogP values.

2.4.1. Predicted impact of chemical-PDMS binding

As noted above, the empirical descriptors of PDMS binding are useful, but specific to limited experimental conditions. To find parameters more useful for modelling chemical- PDMS interactions over a wider range of concentrations and PDMS surface areas, we fit the data to a microscopic model of 1st order binding kinetics.

This model considers a reaction between chemical *A* and PDMS-surface site *S*, *i.e.*, $A + S \rightleftharpoons A_{bound}$. Allowing for reversible interactions, the reaction kinetics follow

$$\frac{d[A]}{dt} = -k_F[A][S] + k_R[A_{bound}] \qquad \text{(Equation 2.3a)}$$

where brackets denote concentrations and k_F, k_R are the forward and backward rate constants. Dropping the brackets, making the time-dependent terms explicit, and casting [*S*] and [A_{bound}] in terms of A(*t*) yields:

$$\frac{dA(t)}{dt} = -k_F A(t)\left(\frac{S_0}{\alpha} - \left(A_{tot} - A(t)\right)\right) + k_R(A_{tot} - A(t)) \qquad \text{(Equation 2.3b)}$$

where A_{tot} is the total amount of chemical divided by the solution volume, S_0 is the initial surface density of binding sites, and α is the ratio of solution volume to PDMS surface area. For a given chemical, binding and desorption experiments were fit simultaneously with shared parameters. Binding experiments were fit to analytic solutions to Equation 2.3b using boundary condition $A(0) = A_{tot}$ = the stated starting concentration. Desorption experiments were fit to solutions with $A(0) = 0$ and A_{tot} being a concentration equivalent to desorbing all chemical bound to the disk's surface in the previous on-rate binding experiment. For chemicals that bound irreversibly, the desorption experiment was simply taken to yield $k_R = 0$. Microscopic model fits are shown alongside the empirical fits of binding/desorption kinetics in Figure 2.2 and Figure 2.3. Parameters from the microscopic model fits are compiled in Table 2.3.

Table 2.3 Summary of microscopic model fit parameters

Chemical	k_F (10^{-4} h^{-1} μM^{-1})	k_R (10^{-2} h^{-1})	S_0 (nm^{-2})
propiconazole	3.7 ± 0.7	0	7300 ± 600
bisphenol A	0.3 ± 0.2	4.6 ± 0.7	500 ± 300
molinate	5 ± 1	0.9 ± 0.2	2500 ± 300
ethofumesate	5 ± 2	2.27 ± 0.4	2000 ± 1000
rhodamine B	3.2 ± 0.3	0.003 ± 0.002	8.0 ± 0.3
imazaquin	1.5 ± 0.5	0	0.13 ± 0.03
hexazinone	7 ± 2	0	0.7 ± 0.1

These microscopic model fit parameters were then used in a computational fluid dynamics (CFD) model combining mass transport and surface reactions to predict the sequestration of chemicals in a PDMS-based microfluidic device (geometric details under Experimental design). This model is very similar to those used in biosensor applications.[98–102] Chemical transport in the bulk fluid is described by a convection–diffusion equation:

$$\frac{\partial c}{\partial t} = D\left(\frac{\partial^2 c}{\partial x^2} + \frac{\partial^2 c}{\partial y^2}\right) - \frac{\partial c}{\partial x} \cdot \vec{u} \qquad \text{(Equation 2.4)}$$

where c is the time-dependent chemical concentration, D is diffusivity of a chemical species in bulk fluid, and u is the position- and time-dependent fluid velocity. Chemical transport and reaction on the PDMS surface are governed by a reaction–diffusion equation:

$$\frac{\partial c_s}{\partial t} = D_s\left(\frac{\partial^2 c_s}{\partial x^2} + \frac{\partial^2 c_s}{\partial y^2}\right) + k_F c(S_0 - c_s) - k_R c_s \qquad \text{(Equation 2.5)}$$

where c_s is the bound species surface density, D_s is its surface diffusivity, S_0 is the binding capacity per unit of PDMS surface area, and k_F, k_R are the forward and backward rate constants for surface binding respectively. The surface reaction expression in Equation 2.5 includes the bulk

concentration, c, at the reacting surface. This coupling with mass balance in the bulk is obtained at the flux boundary according to

$$D\left(\frac{\partial c}{\partial y}\right) = k_F c(S_0 - c_s) - k_R c_s \qquad \text{(Equation 2.6)}$$

Although this model does not explicitly consider diffusion into bulk PDMS, such diffusion must occur, especially for chemicals for which PDMS has a larger binding capacity. For example, the fitted binding capacity for molinate is 2500 molecules per nm^2. If molinate molecules were truly packed on a PDMS surface at this density, each molecule would occupy an area of just 4×10^{-4} nm^2, which is much too tightly packed to be reasonable. Instead, molinate and other chemicals with S_0 > O (1 nm^{-2}) must penetrate into PDMS and S_0 should be considered as effective density per unit of geometric surface area.

To explore the potential range of binding and chemical sequestration in a microfluidic device, we ran this model for three tested chemicals: ethofumesate, which binds reversibly; propiconazole, which binds irreversibly; and rhodamine B, which is minimally adsorbed by PDMS. Since these chemicals were of similar size, their diffusivities were taken to be the same: 10^{-9} m^2 s^{-1} in aqueous solution (D) and 10^{-11} m^2 s^{-1} along the PDMS surface (D_s). Each model considered parabolic flow with a maximum velocity, u_{max} = 100 μm s^{-1}. We model a hypothetical device in which a cell culture chamber begins at the end of an 8 mm long channel; cellular exposure is thus taken as the chemical concentration just above the PDMS surface at the end of this channel. We investigated effects under both continuous injection of chemicals (starting from t = 2 hours) and bolus injections (from t = 2 to 6 hours) over a wide range of inlet concentrations from 10^{-2} to 10^{-7} M. Inlet concentrations for ethofumesate and propiconazole were limited to ≤10^{-4} M due to their low aqueous solubility. Predicted cellular exposures are shown for all three chemicals for continuous and bolus injections in Figure 2.5A–C and Figure 2.6A–C, respectively. These figures

also include the corresponding degree to which PDMS binding sites are saturated (Figure 2.5D–F and Figure 2.6D–F).

Under continuous dosing, the differential impacts of reversible and irreversible PDMS binding can be seen by comparing Figure 2.5A and D and B and E. For a reversible binder like ethofumesate, the predicted cellular exposure gradually increases with time and asymptotically approaches the inlet concentration (Figure 2.5A). This occurs for all inlet concentrations once the on- and off-rates for PDMS binding approach equilibrium. For the highest inlet concentration simulated (10^{-4} M), this equilibrium occurs at nearly 70% surface saturation (Figure 2.5D). On the other hand, for an irreversible binder like propiconazole, the predicted cellular exposures only approach the nominal inlet concentrations once the surface be- comes fully saturated (Figure 2.5B and E). Even at the highest dose simulated (10^{-4} M), reaching saturation can take several hundred hours. For doses that do not yield surface saturation within the simulated time window (200 h), the predicted cellular exposure remains an order of magnitude less than the nominal inlet concentration.

Additional impacts arise under bolus dosing. For a reversible binder like ethofumesate, exposure was at lower levels (less than 30% of inlet exposure) for all of the 4-hour bolus period (Figure 2.6A and D). Even more interestingly, once a bolus dose ended, cellular exposure continued. This extended exposure was due to gradual chemical desorption from the surface. It could initially be as large as 5% of the bolus exposure and gradually diminished to less than 1% after 48 hours. Such extended exposures were absent for an irreversible binder like propiconazole, but it too had effects that were highly dependent on the nominal inlet concentration. Only at the highest simulated dose (10^{-4} M) was propiconazole able to saturate the device's PDMS surfaces during the bolus period and thus yield cellular exposures approaching the nominal inlet

concentration. For all other simulated doses, the exposures were an order of magnitude less than the nominal dose.

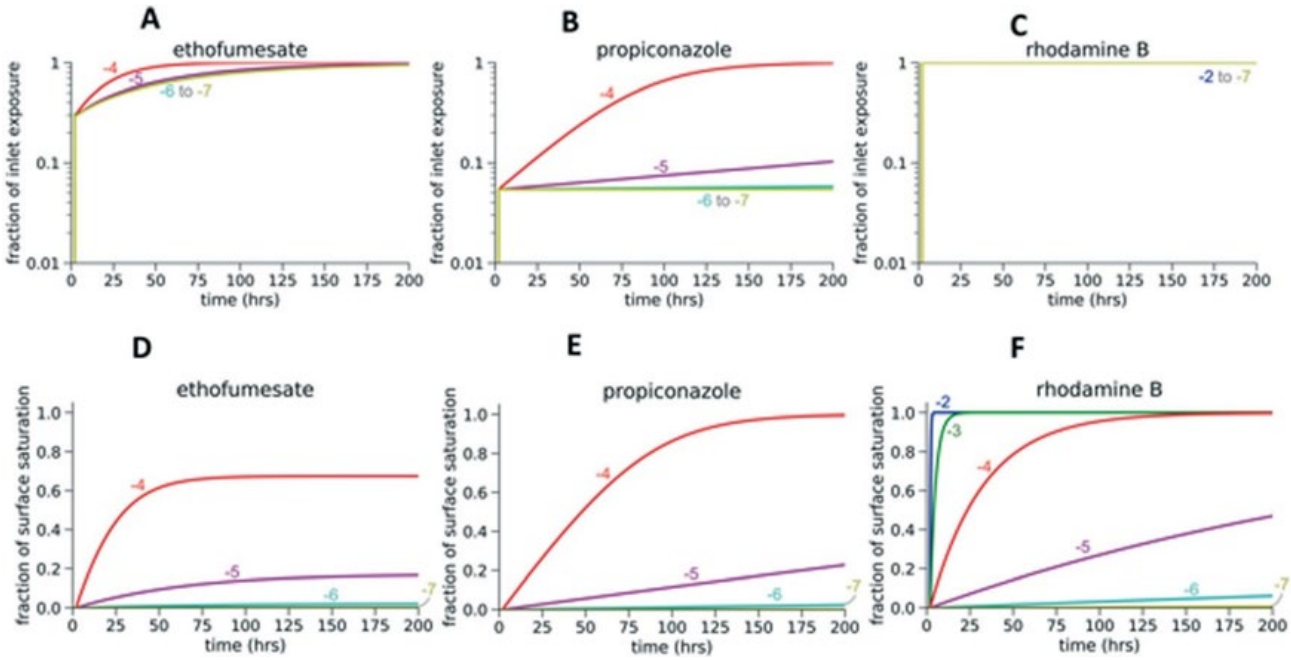

Figure 2.5 CFD model predictions for continuous dosing with inlet concentrations from 10^{-7} to 10^{-2} M: (A–C) predicted cellular exposures as a fraction of inlet exposures; (D–F) predicted degree of PDMS surface saturation. Chemical classes represented by ethofumesate with strong reversible binding, propiconazole with strong irreversible binding, and rhodamine B with weak reversible binding. The number next to each curve is log of the inlet concentration.

For weaker binding chemicals like rhodamine B, cellular exposures closely match inlet concentrations. This is true for all simulated doses under both continuous (Figure 2.5C and F) and bolus exposures (Figure 2.6C and F). At low inlet concentrations (10^{-7} to 10^{-5} M), the on-rate for binding is so low that there is little impact on cellular exposures under the modelled flow conditions. At higher inlet concentrations (10^{-2} to 10^{-4} M), binding is more rapid and the system quickly reaches surface saturation (Figure 2.5F), but the low binding capacity of the surface again results in little change in chemical concentrations throughout the perfusate.

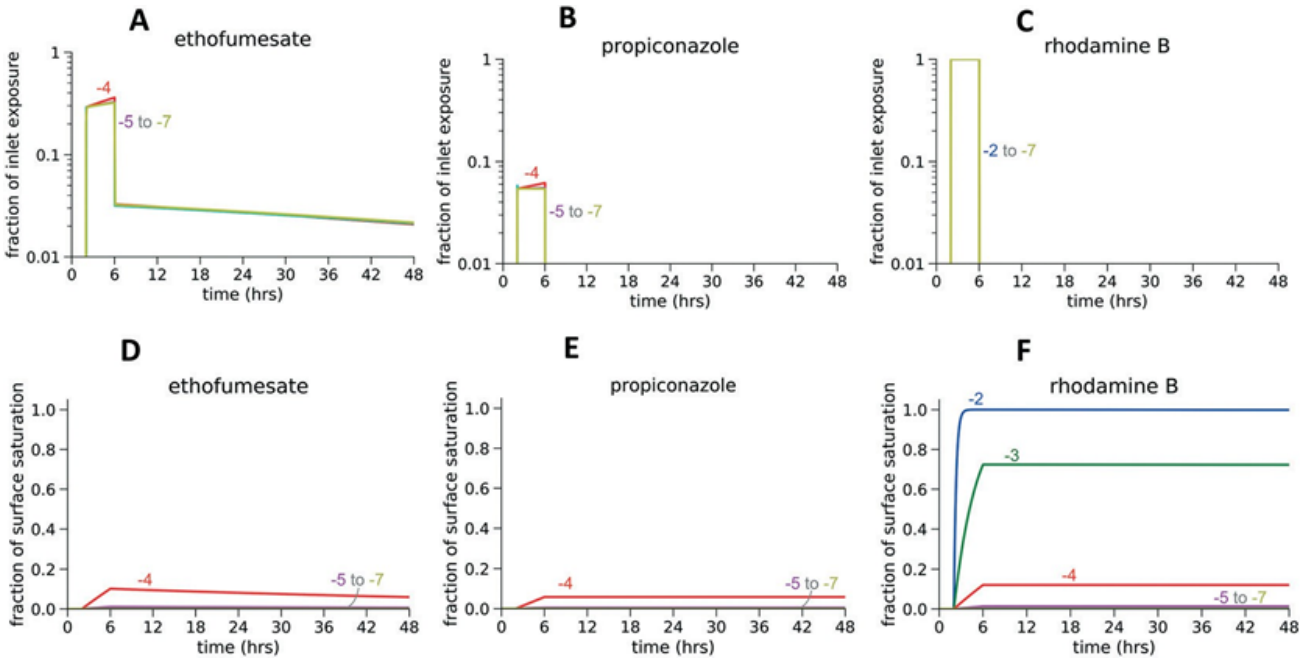

Figure 2.6 CFD model predictions for 4 h bolus dosing with inlet concentrations from 10^{-7} to 10^{-2} M: (A–C) predicted cellular exposures as a fraction of inlet exposures; (D–F) predicted degree of PDMS surface saturation. The number next to each curve is log of the inlet concentration.

2.5. Discussion

Here we have investigated binding to PDMS surfaces for 19 chemicals of interest in environmental toxicology. This set of test chemicals covers a wider range of molecular properties than previous studies and allows us to further delineate those characteristics most closely associated with binding to PDMS. In addition, for those chemicals that did bind, we have more fully characterized the on- and off-rate kinetics to facilitate predictive modelling of chemical sequestration and actual cellular exposures in PDMS-based microfluidic devices.

Importantly, we used two experimental setups, disk soaks and channel soaks, to fully characterize both weak and strong PDMS affinities. Only one compound in our test set, *i.e.*, bisphenol A, was amenable to kinetic characterization in both setups. Given the different surface-to-volume ratios and starting concentrations, the two experiments for bisphenol A yielded quite different empirical parameters (% bound and time constants); however, all of the bisphenol A data

could be fit well simultaneously with a single set of microscopic kinetic parameters (k_F, k_R and S_0) (Figure S1). This consistency is an important validation of the approach taken here.

In terms of the molecular properties that influence PDMS binding, we also find a key role for measures of chemical hydrophobicity. Wang *et al.* tested five compounds and noted an apparent logP threshold separating chemicals that bound PDMS strongly (≥2.62) from those that did so weakly or not at all (≤2.47).[36] Van Meer *et al.* tested four other chemicals – all with logP above the apparent threshold – and instead noted a linear correlation between the percent remaining unbound to PDMS and the compounds' TPSA, another measure of hydrophobicity.[30] Once we add our data, these measures are no longer fully predictive of PDMS binding over the combined data set of 26 chemicals. We find that insufficient hydrophobicity is still a useful predictor of chemicals that do not partition into PDMS. Both logP and TPSA can be used to establish such a threshold at less than 1.85 for logP or greater than 91.6 $Å^2$ for TPSA. Note that these results were obtained using unmodified PDMS; plasma treatments used to reduce PDMS surface hydrophobicity could alter the logP and TPSA binding thresholds.

Despite agreement on thresholds, we find that the degree of PDMS binding for chemicals with logP above (or TPSA below) threshold is no longer linearly related to TPSA. Neither is it related to molecular weight (range from 187 to 808 g mol^{-1}) or polarizability (range from 17 to 980 $Å^3$). Among those and 15 other molecular properties catalogued by ChemSpider (http://www.chemspider.com), the best predictor of PDMS binding was logP above the noted threshold and the number of H-bond donor groups (*T*-test P-value = 0.0037). Highly hydrophobic compounds with no H-bond donor groups were strongly sequestered by PDMS, those with one tended to be sequestered more modestly, and those with two or more were affected weakly if at

all. One chemical right at the logP threshold (hexazinone) with zero H-bond donors did not partition appreciably into PDMS in disk-soak experiments, but did so in channel soaks.

As noted above in Results, the large PDMS-binding capacities (S_0) for some chemicals show that substantial sequestration requires both surface partitioning and diffusion away from the surface into the PDMS bulk. Although logP is a reasonable measure of how well a chemical partition from aqueous solution into PDMS,[103] this partitioning is only at equilibrium near the interface. As has been shown previously, larger sequestration in PDMS-based microfluidics is associated with larger chemical diffusivity in PDMS,[34] and diffusion through PDMS membranes is slower for chemicals with a larger number of H-bond donors.[104] It is thus insightful, but not surprising, that the number of H-bond donors in a molecule can affect its sequestration by PDMS.

As shown in Figure 2.4, one notable exception to the above trend is rhodamine 6G. This compound has two H-bond donor groups, and yet Wang *et al.* concluded that it bound PDMS strongly.[36] When we tested rhodamine 6G in our experimental setup, we found a conflicting result with little to no PDMS binding. Both setups were depletion experiments, *i.e.*, measuring the amount of chemical left in bulk solution after some duration of exposure to PDMS, but the experiments differed in the method used to measure chemical concentration. Our experiments used UV-vis absorption, whereas Wang *et al.* used fluorescence intensity. Fluorescence is more sensitive, but also subject to photobleaching or quenching, which could explain the discrepancy by yielding an apparent depletion of rhodamine 6G even in the absence of PDMS binding. We thus consider absorption spectroscopy a more robust measure of chemical concentration. Of note, rhodamine 6G was the only compound that Wang *et al.* quantified *via* fluorescence; the others were measured *via* radiolabels that are not subject to the same complications.[36]

Beyond elucidating the molecular properties that correlate with PDMS binding, our experiments quantify binding to PDMS in a way that provides new insights. First, for three of the five PDMS-binding chemicals tested here, the carrying capacity of PDMS exceeded 1000 molecules per nm^2. Such carrying capacities are obviously much too large to represent pure surface packing and it is well known that small molecules can diffuse into the PDMS bulk.[27] Building on the model presented by Shirure and George,[34] one would expect the carrying capacity to increase with a chemical's diffusivity within PDMS. Such diffusivity is however difficult to measure directly for non-fluorescent molecules. Carrying capacity thus provides an alternative and more easily measurable parameter for bioavailability modelling that is valid at least over tens to hundreds of hours. This time regime is longer than the measured time constants associated with binding and desorption, which ranged from 2 to 18 hours.

These time constants are in a range that complicates the evaluation of multi-day chemical screening for targeted and/ or adverse responses in microfluidically cultured cells and tissue constructs. Based on our modelling, the complications are three-fold. First, even if the nominal inlet concentration is constant, cellular exposure to a drug or potential toxicant will be time-dependent. Furthermore, the time needed to reach a steady-state exposure will be longer for lower inlet concentrations. Second, for chemicals that bind PDMS reversibly, even the steady-state cellular exposure will be less than the nominal dose – an order of magnitude less given the values we observe for the example of ethofumesate. Third, the delivery of acute doses of reversibly binding chemicals will be complicated by long tails of extended low-dose exposure long after a bolus injection. Our modelling approach shows that these complications can be estimated and thus considered in evaluating cellular responses. It may also be possible to use this modelling approach

in a reverse manner to design a time-dependent inlet concentration profile that yields a targeted time-dependent cellular exposure.

2.6. Conclusions

We have established a technique to measure chemicals' PDMS-binding kinetics and a method to use these measured kinetic parameters to model chemical transport in PDMS- based devices and thus predict time-dependent cellular exposures. Further, we have found that binding to PDMS is not only correlated with measures of hydrophobicity such as logP or TPSA, but also increases for compounds with fewer hydrogen-bond donor groups. This finding can serve as an exclusion criterion for compounds likely to have strong interactions with PDMS and thus difficult to interpret effects on cells in PDMS-based devices.

CHAPTER 3

EXTENDED MODEL FOR VALIDATING IN-DEVICE TOXICOKINETICTS

3.1. Modeling In-Device Toxicokinetics

As described in Chapter 2, computational fluid dynamics models were developed to estimate in-device toxicokinetics based on reversible binding of chemicals onto PDMS surface with chemical specific surface binding capacity. Those key chemical-PDMS interaction parameters were experimentally measured from the time dependent depletion of chemicals from solution in contact with PDMS surfaces and its return from the PDMS surfaces to fresh solvent. The geometry was modeled for different length scales based on surface-area-to-volume-ratios: low ratio for disk soak experiment with PDMS disks floating in solution in small vial and high ratio for channel soak experiment with solution filled channels in larger PDMS blocks. The original modeling approach considered lumped surface binding capacity that cannot separate the contribution of binding of chemical onto PDMS surface and diffusion of that chemical into PDMS bulk. This combined contribution of surface partitioning and diffusion into the PDMS bulk may be an inadequate descriptor of the appropriate phenomena involved in chemical-PDMS interaction in different time and length scale. This discrepancy led to further analysis on how the model can be extended and validated with the experimental observation.

3.2. Implementing Diffusion into Bulk PDMS in the Toxicokinetic Model

An extension of the model was developed that allows diffusion into bulk PDMS. For doing so, additional PDMS bulk layers were modeled on top and the bottom of the microchannel as shown in Figure 3.1a. First, the original model was kept with the reversible surface binding parameters and was revised by adding diffusion coefficient through the PDMS bulk, referring to

as surface reaction model. Second, the fixed binding capacity parameter was replaced with a PDMS-water surface partitioning coefficient and a bulk PDMS diffusion coefficient, referring to as partitioning model. The original model was then compared with the surface reaction model and the partitioning model by simulating disk- and channel- soak experiments.

Surface reaction model, when compared with the original model, the final concentrations were found to be same. This is because of these two models' similar approach of applying binding kinetics at the PDMS surface, with an exception in surface reaction model by an additional diffusion into the bulk. In both cases, the same amount of chemical bound to the surface, with an additional observation that the bounded amount in surface model found to diffuse through the PDMS layer. This consistency validates the modeling set-up for the extension.

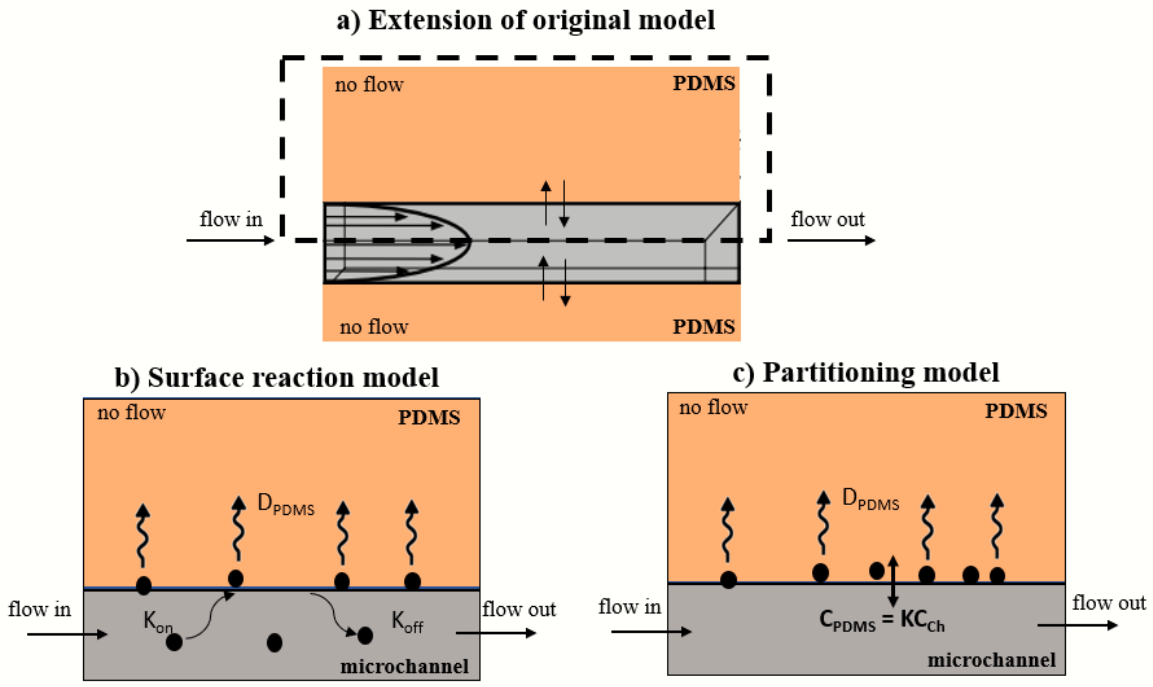

Figure 3.1 a) Extension of the original model by including PDMS bulk section on top and below the microchannel (the dotted box represents the section of the geometry that are shown in b and c; b) surface reaction model: original model with the binding kinetics of chemical-PDMS was extended by adding diffusion into the PDMS bulk; c) partitioning model: replacing fixed binding capacity parameter with a PDMS-water partitioning coefficient and diffusion into the PDMS bulk.

3.3. Geometry Development in Extended Models

For simulating disk-soak and channel-soak experiments, geometries were developed in COMSOL using the dimensions as described in Chapter 2. In the disk-soak model, a cylindrical PDMS disk (6 mm in diameter and 5 mm in height) was soaked in a 4-mL cuvette as shown in the Figure 3.2. The interface between solution phase and PDMS phase was defined with the partitioning coefficient for the chemical partitioning to PDMS bulk. In the channel-soak model, 0.1 x 1.5 x 21.1-mm long channel was inserted in the PDMS block. For modeling in both set-ups, diffusivity into the PDMS was defined. These channel-soak model had a much larger surface-to-volume ratio compared to disk-soak model (70 cm^{-1} versus 3 cm^{-1}).

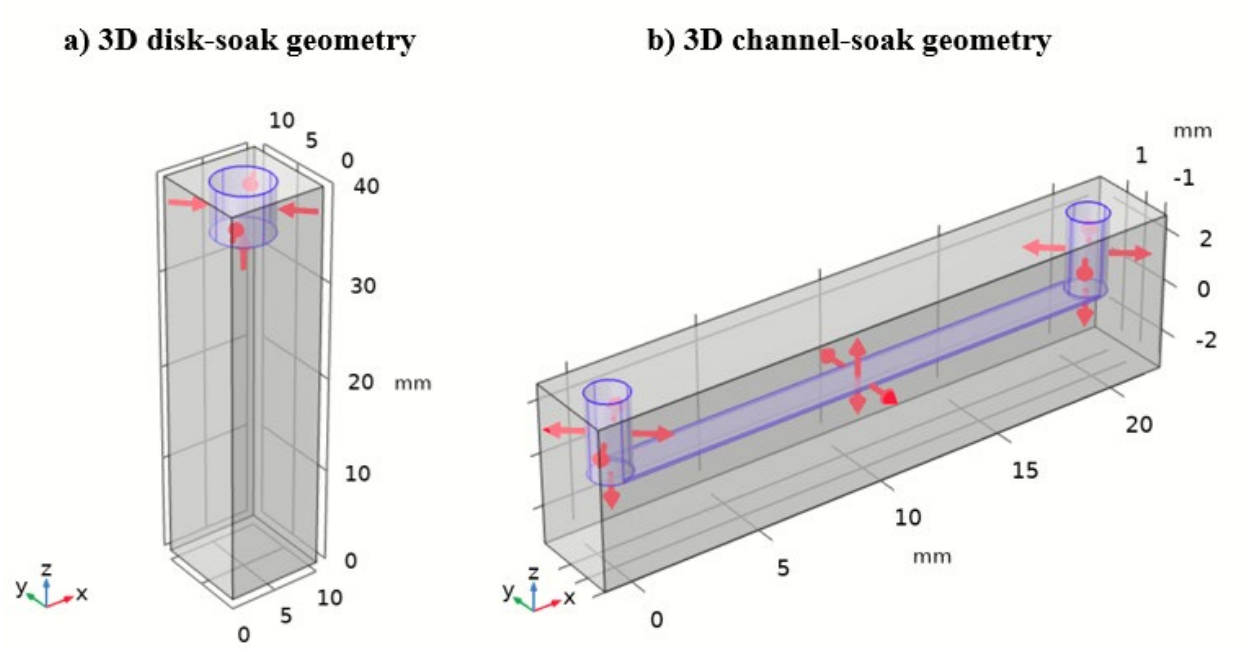

Figure 3.2 3D geometries of disk-soak and channel-soak experiments: a) disk-soak: a cylindrical PDMS disk (6 mm in diameter and 5 mm in height) was soaked in a 4-mL cuvette; b) channel-soak: 0.1 x 1.5 x 21.1-mm long channel was inserted in the PDMS block; red arrows in each figure denotes the transport of chemicals through the PDMS bulk.

3.4. Preliminary Analysis of Extended Modeling Approaches

The preliminary analysis included modeling of disk- and channel-soak experiments for two chemicals: Bisphenol A and Ethofumesate for which PDMS interaction parameters have been measured as described in Chapter 2. Bisphenol A was tested via disk- and channel-soak experiments in Auner et al. (2019) and found to have significant PDMS interactions. Ethofumesate, tested via disk-soak only, exhibited a significant binding and unbinding characteristics with PDMS[43].

The extended models were developed to include surface binding capacity in the surface reaction model and partitioning coefficient in the partitioning model (as mentioned in the previous section). The surface reaction modeling approach has already been fairly applicable to the disk-soak length scale[43]. The task was to find out the caveats (in any) of using both surface reaction and partitioning approaches considering both length scales. If the model results complement each other, that will confirm the validity of the two modeling approaches. In this analysis, partitioning coefficient was derived from the surface reaction model and applied into the portioning model for both disk- and channel- soak experiments. The coefficient thus derived was referred to as effective partitioning coefficient (partitioning coefficient, $K = \frac{concentration\ in\ the\ PDMS\ bulk}{concentration\ in\ the\ solution\ phase}$). One example of such calculation was included in supplementary section S.2. For these chemicals with similar size, their diffusivities were taken to be 10^{-9} m^2/sec in aqueous solution and 10^{-11} m^2/sec into the PDMS bulk (D_{PDMS}). Whether this assumption of D_{PDMS} is valid will be discussed later.

3.4.1. Bisphenol A

Bisphenol A was modeled with starting concentration of 97 µM and 3000 µM, similar to the concentration used in the disk- and channel- soak experiments, respectively. With a simulation

time of 48 h, surface reaction model in disk-soak set-up predicted very small depletion. This was an expected observation because of bisphenol A's known weaker partitioning into PDMS in disk-soak length scale. The portioning model was then run using the effective partitioning coefficient of 0.45. Using the effective partitioning coefficient, the modeled concentration appeared to be consistent with the surface reaction model (see Figure 3.3).

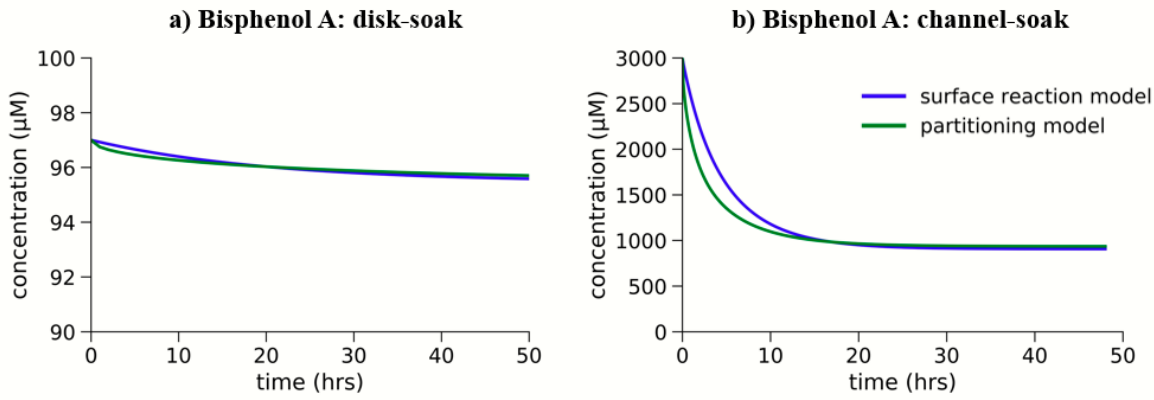

Figure 3.3 Predicted concentration depletion of bisphenol A for simulating experiment in different length scales: a) disk-soak (starting conc. = 97 µM, effective partitioning coefficient = 0.45) and b) channel-soak (starting conc = 3000 µM, effective partitioning coefficient = 0.064) experiments; Surface reaction model and partitioning model appears to be consistent when appropriate effective portioning coefficients were used.

Similarly, surface reaction model was run for simulating channel-soak experiment, with a starting concentration of 3000 µM. Unlike, disk- soak result, predicted concentration depletion was large in channel soak length scale – as expected due the larger surface-area-to-volume ratio. The effective partitioning coefficient was calculated to be 0.064 which is much smaller than the former one (0.064 vs 0.45). In fact, effective partitioning coefficient is not the universal description, rather depends on the starting concentration and the length scale – the variability in this calculated parameter is reasonable. After the simulation of channel-soak experiment, the predicted concentration depletion was fairly consistent, with a small discrepancy in the rate at

which those two models predicted the depletion. Such discrepancy may arise from the diffusion coefficient being selected based on assumption. Deeper understanding of diffusivity of the chemicals into PDMS bulk is necessary.

Apart from the modeling of disk-soak and channel-soak experiment, bisphenol A was also modeled for hypothetical situation where surface-area-to volume ratio (α) were varied for channel-soak setting. The goal was to investigate the concentration depletion against a wide range of α by modifying the geometry by changing the microchannel dimension as shown in the Figure 3.4. The wider the microchannel, the lower the surface-area-to volume ratio. With a starting concentration of 3000 μM in the surface reaction model, higher depletion was predicted with the higher α (Figure 3.5). Similar observation of chemical interaction with device materials with respect of the device aspect ratios was described by Jenke and Rabinow et al (2017)[105].

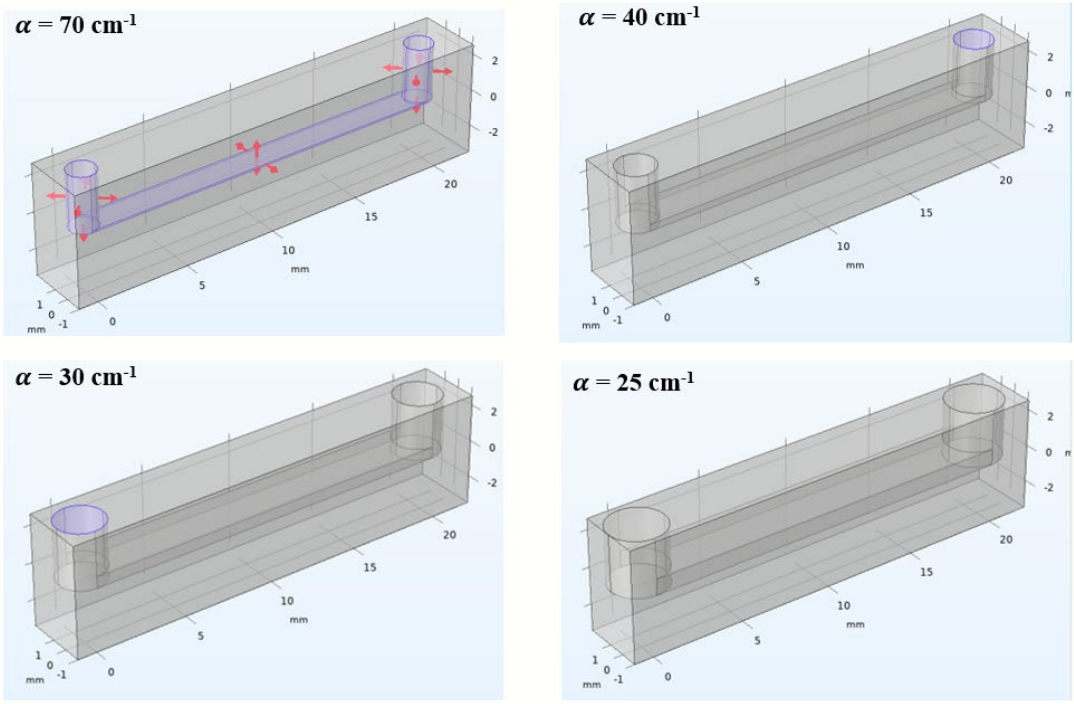

Figure 3.4 Geometry modification similar to channel-soak experiment, surface-area-to volume ratio (α) was modified by changing the microchannel dimensions; red arrows in denotes the transport of chemicals through the PDMS bulk.

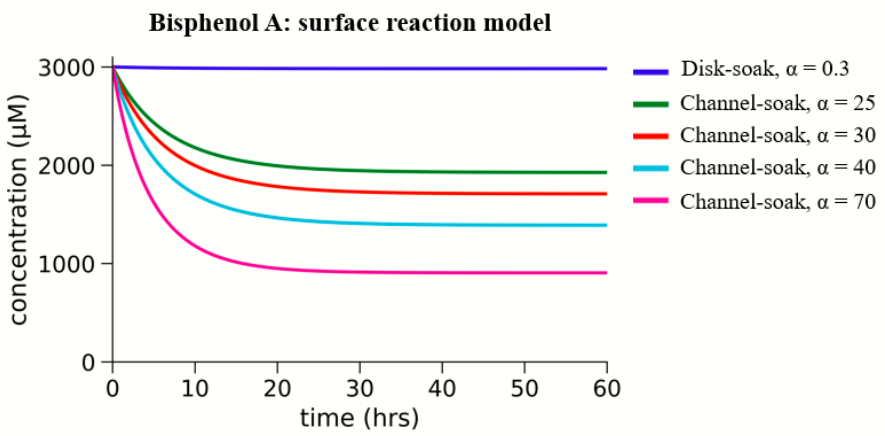

Figure 3.5 Depletion of bisphenol A using surface reaction model; the larger the surface-area-to-volume ratio, the higher the degree of partitioning.

3.4.2. Ethofumesate

Similar to the modeling approaches for bisphenol A, surface reaction and partitioning model was developed for ethofumesate to simulate both disk- and channel- soak experiments. Unlike bisphenol A, same starting concentration (175 μM, based on the maximum solubility of ethofumesate) was used for ethofumesate. By taking similar starting concentration, the intention was to investigate if similar partitioning parameter can be applied to both length scales. Figure 3.6 shows the predicted depletion of ethofumesate for disk- and channel- soak experiment. The prediction from partitioning model was fairly in agreement with the surface model results for disk-soak simulation, with an effective partitioning coefficient, K = 19.5 (Figure 3.6a). In channel-soak simulation in Figure 3.6b, the surface model predicted very steep depletion which may indicates the impact of high surface capacity parameter of ethofumesate. By running the partition model with the K value of 19.5, strong partitioning of ethofumesate was also evident. Similar to what was observed for bisphenol A, the discrepancy in the initial depletion rate seems to arise from the diffusion coefficient through the PDMS bulk, which was an assumed value and may not be an appropriate one.

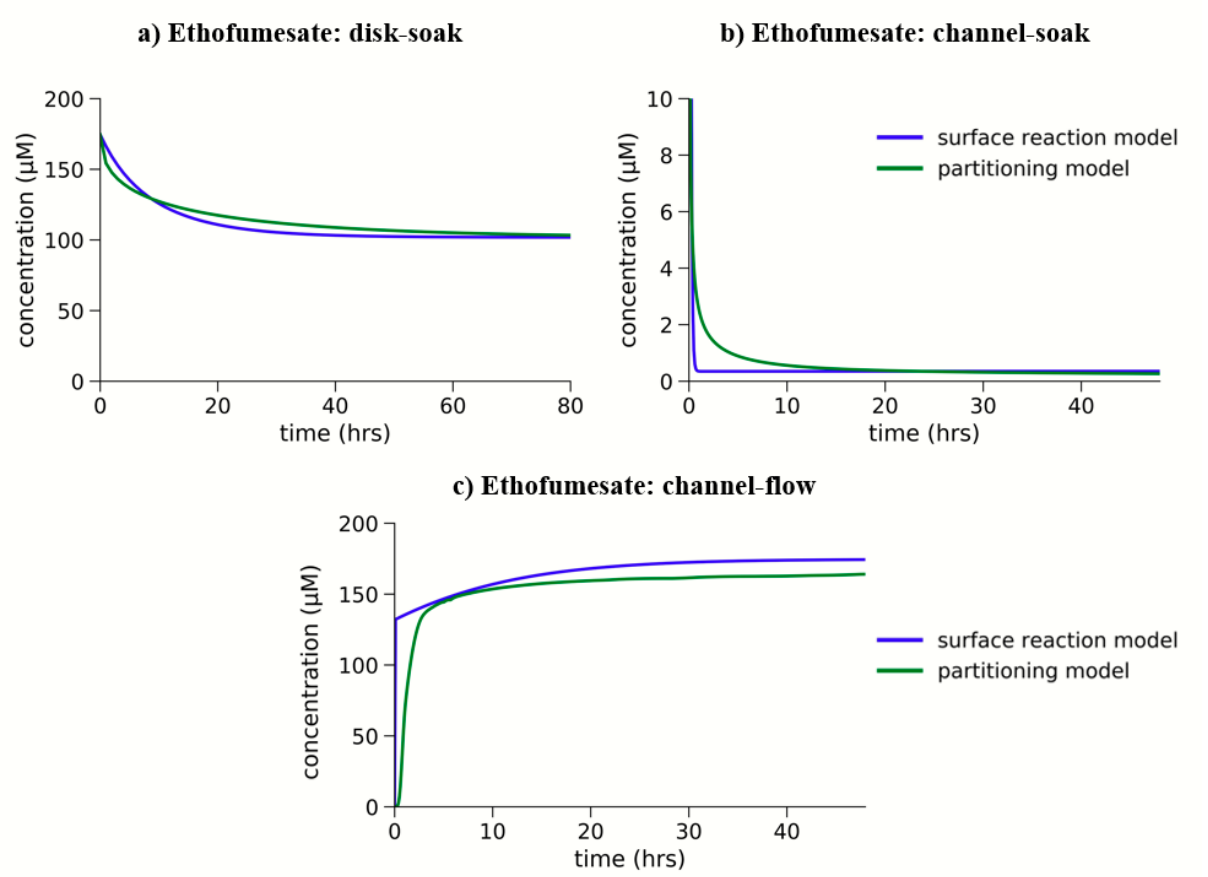

Figure 3.6 Predicted concentration depletion of ethofumesate for simulating experiment in different length scales and conditions: a) disk-soak, b) channel-soak, c) channel-flow experiments; for similar starting concentration of 75 µM (nominal concentration for channel-flow simulation), same effective portioning coefficient (K =19.5) can be used to pursue partitioning modeling approach.

In addition to disk- and channel- soak simulation, a model was developed for ethofumesate depletion in the channel-flow experiment, particularly for predicting the concentration at the channel outlet as done in the real microfluidic experiments. Nominal concentration was set to 175 µM at a flow rate of 10^{-10} m^3/sec (6 µL/min) for simulation time of 48 h. Due to the continuous exposure of ethofumesate, both surface reaction and partitioning model predicted the concentration to reach the nominal concentration (Figure 3.6). These models were developed using surface binding capacity extracted from the prior modeling approach. And the proper understanding of the

diffusivity of chemicals into PDMS is still missing. The findings under flow-condition, therefore, cannot be conclusive without further analysis and validating with channel-flow experiments.

3.5. Preliminary Experimental Design for Model Validation

The extended modeling approach works well for disk soak and channel soak experiments, but has not been validated against channel flow experiments with measurements in perfused organ-on-chip devices. So, an experimental scheme has been implemented to validate in-device toxicokinetics. The preliminary experiment was performed with two chemicals with strong chemical-PDMS binding: ethofumesate and molinate.

To examine the effect of chemical-PDMS binding, chemicals were introduced to PDMS microchannel in a real device and the effluent were collected from the channel outlet at specified time intervals. Chemicals were administered using syringe pump at a flow rate of 36 µL/h (maximum velocity, $u_{max} = 10^{-4}$ m/sec). Following the exposure, the hourly samples were collected in microcentrifuge tubes for the first 24 h and daily thereafter until the effluent concentration no longer changes. Hourly collected sample's UV-Vis spectra were measured using Nanodrop 2000C Spectrophotometer. Dilution series standards were also measured for all tested chemicals, and calibration curves were generated to translate absorbance into concentration.

Experimental protocol was developed for forward kinetics and reverse kinetics. Experiments for forward kinetics included real measurement with chemicals perfused to saturated PDMS using PFA tubing, positive control with chemical perfusion only through PFA tubing (no PDMS), and negative control with water (solvent) perfusion into PDMS using PFA tubing. For reverse kinetics, chemical flow was stopped in real measurement and water was allowed to flow to see if any chemical comes back into solution in the channel (i.e., the reverse Kinetics). During

the long-hour preliminary experiment (n=1), positive and negative controls were good for both chemicals. While complete loss of molinate was observed, ethofumesate concentration stayed at 50% of the injection concentration though out the experimentation. In the reverse experiment, non-measurable desorption was anticipated. Overall, a constant sequestration of chemical from the solution was evident in the long-term binding experiment which is also not consistent with the predicted concentration in Auner et al (2019) and the model presented here in Figure 3.6c. It implies that the chemical-PDMS interaction is far from saturation as a result of rate limiting binding-unbinding kinetics of chemicals with PDMS. This observation needs further investigation.

Sone challenges were experienced in performing the validation experiments. Chemicals were found to have interaction with tygon tubing system which was later replaced with the more chemical resistant perfluoroalkoxy (PFA). Care should be taken when testing highly volatile chemical like Molinate. In that situation, experiments should be designed under confined setting.

3.6. Discussion

From the preliminary modeling analysis, it has been observed that both surface reaction and partitioning model can be fairly in agreement across different length scales with an effective partitioning coefficient. Surface reaction model is, in fact, just an extension of the original model by including PDMS bulk diffusion. In the partitioning model, the binding-unbinding kinetics was replaced a fast kinetics of partitioning of chemicals into PDMS. This partition coefficient used, however, is not chemical specific, rather very specific to experimental/modeling condition.

Regardless of the modeling approaches, it has also been tested that, chemical depletion and strong partitioning is obvious with the higher surface-area-to-volume ratio, in other word, in smaller length scale. This potential problem is worsened by the small channel dimensions in such

devices' microfluidic perfusion systems, which yield high surface-area-to-volume ratios. These ratios can range from 100-1000 cm^{-1} for organ-on-a-chip systems. The orders-of-magnitude larger relative surface area means that partitioning of a chemical into the PDMS surfaces of microfluidic channels can drastically change a chemical's concentration in the perfusing solution[34,43].

In this chapter, efforts have been made to validate different modeling approaches in different length scales. Details of validity and applicability of different models in different length scales are summarized in Table 3.1.

Table 3.1 Summary of modeling approaches and their applicability in different length scale

Experiment	**Original model**	**Surface Reaction Model (adding PDMS bulk Diffusion)**	**Modeling with Partitioning coefficient**
Disk-soak	Model results are consistent with the experimental observation	Outlet concentration is similar to the original model. Chemical retained on the surface diffuses through the PDMS. (no additional impact)	Model can reproduce experimental results (with effective partitioning coefficient calculated from surface reaction model)
Channel - soak	works well with surface reaction model.	works well with surface reaction model.	Partition model closely follow the surface reaction model.
Channel - flow	Model results don't follow experimental findings. Outlet concentration quickly reaches the injection concentration	Outlet concentration is similar to the original model. Outlet concentration quickly reaches the injection concentration	Doesn't seem to achieve steady state

As also discussed in Chapter 2, the prior modeling approach didn't provide any means to separate the contributions of surface partitioning of a chemical into PDMS and its diffusion into the PDMS bulk. The binding capacities for some of the chemical in the prior work were too large to represent a true surface carrying capacity which thus implies a significant diffusion into the PDMS bulk. The inconsistency and discrepancy in those models and the lack of knowledge on the

paramter values (including PDMS diffusivity and the partition coefficient) clearly shows the need for experimentally measured parameters to make the model more predictive of the real scenario of chemical partitioning into PDMS under microfluidic condition.

3.7. Conclusion

Two physical phenomena are involved in chemical-PDMS interaction: surface binding-unbinding and diffusion into PDMS. The rate limiting kinetics will govern the degree of chemical sequestration into the PDMS. The preliminary experiment, showed constant sequestration of chemicals (Ethofumesate) that means saturation never achieved. It could be the result of rate limiting binding-unbinding kinetics of chemicals. Instead of using the prior modeling approach with lumped surface binding parameter, a hybrid model should be developed that includes the distinct contribution of the binding and unbinding kinetics with more realistic surface binding capacity and the appropriate diffusion coefficient into the PDMS. This challenge certainly seeks for further experiment to find out the diffusion coefficient for the chemicals under fluidic condition.

CHAPTER 4

COMPUTATIONAL MODEL FOR DOWNSTREAM METABOLITE DETECTION

4.1. Introduction

Organ-on-chip microsystem (OCM) shows promises to recreate the dynamics of cellular functions in response to chemicals and drugs. To achieve its full potential, it is essential to integrate detection techniques with high spatial and temporal resolution, for monitoring cellular metabolic responses, such as glucose or glutamate uptake and lactate production. One of the techniques of detection is electrochemical sensors based on electrical measurement against chemical concentration[1]. Such electrochemical sensing techniques developed at the Vanderbilt Institute for Integrative Biosystems Research and Education (VIIBRE) are: 1) microphysiometer, with sensor electrodes embedded with cells in the same chamber allowing *in situ* detection, and 2) microclinical analyzer (μCA), sensor chamber placed downstream of the cell chamber allowing downstream detection.

While *in situ* detection using microphysiometer has already demonstrated its capability for instantaneous measurement[48,54,106], their design can be complex and system specific. On the other hand, μCA, a comparatively newer and versatile design under investigation, is advantageous for being adaptable to variety of cell culture microsystems with easy pumping and valve system.[1] The application of μCA can be possible with detailed understanding of its ability to measure the metabolic signals downstream, without compromising the resolution. In this work, a detailed computational approach has been taken to evaluate the performance of μCA in detecting cellular metabolism using enzyme-based sensors.

4.2. Enzyme-based Sensors for Metabolite Detection

The majority of electrochemical sensors are enzymatic sensor which are very selective to particular interaction with specific metabolite in the heterogenous environment of cells. Coating of enzyme onto the sensor electrode enables detection of chemicals that can be enzymatically oxidized. Oxidase enzymes, glucose-, lactate-, glutamate-oxidase have all been used for electrochemical detection.[46] Enzymes are deposited on electrode head that is exposed to the solution to be analyzed. This layer also includes bovine serum albumin (BSA) and the crosslinker glutaraldehyde[46,48,106]. If the electrode is biased at a correct voltage, the rate of conversion of O_2 to peroxide (H_2O_2) in the sensor electrode region can be described by,[106]

$$O_2 + 2e^- + 2H^+ \overset{pt}{\rightarrow} H_2O_2 \qquad \text{(Equation 4.1)}$$

The enzyme layer onto the electrode is porous medium allowing the chemical/analyte (A) to diffuse though it. The chemical reaction occurring in the enzyme layer is described by the Michaelis Menten kinetics:[106]

In the glucose-oxidase enzyme layer:

$$glucose + O_2 + H_2O \rightarrow gluconic\ acid + H_2O_2 \qquad \text{(Equation 4.2a)}$$

In the lactate-oxidase enzyme layer:

$$lactate + O_2 + H_2O \rightarrow pyruvate + H_2O_2 \qquad \text{(Equation 4.2b)}$$

In the glutamate-oxidase enzyme layer:

$$glutamate + O_2 + H_2O \rightarrow glutamic\ acid + H_2O_2 \qquad \text{(Equation 4.2c)}$$

An additional thin layer of Nafion polymer is deposited on the enzyme layer that limits the escape of peroxide and increase the signal[48]. Generated H_2O_2 diffuses through the enzymatic layer

to the electrode to generate the signal following the reaction in Equation 4.3. The peroxide donates two electrons and then oxidizes back to water and oxygen.

$$2H_2O_2 \overset{pt}{\rightarrow} O_2 + 2e^- + 2H^+ \qquad \text{(Equation 4.3)}$$

Electrochemical signal are proportional to the peroxide consumption across the sensor electrode[106,107]. To determine the peroxide consumption, the flux can be calculated using Equation 4.4 where I is the current generated by peroxide, n is the number of electrons transferred in the reaction (n =2 for redox couple of metabolites and respective enzymes), F is the Faraday's Constant. W is the working area (in this case, circular head of the electrodes), and J is the molar rate of transfer.

$$I = nFWJ \qquad \text{(Equation 4.4)}$$

The molar rate (J) can be evaluated from the peroxide production rate using enzymatic reaction expression. The Michaelis Menten type reaction in the enzyme layer can also be described by $[A] + [E] \underset{k_R}{\overset{k_F}{\Leftrightarrow}} [EA] \xrightarrow{k_{cat}} [P] + [E]$ where rate of peroxide production can be expressed as:

$$\frac{dP}{dt} = \frac{V_{max}}{K_m + c_s} \qquad \text{(Equation 4.5a)}$$

$$K_m = \frac{k_r + k_{cat}}{k_f} \qquad \text{(Equation 4.5b)}$$

Here brackets denote concentrations, A is the chemical/analyte (glucose/lactate/ glutamate), P is the peroxide (H_2O_2), E is the enzyme, k_F, k_R, and k_{cat} are the reaction rate constants, V_{max} is the maximum rate of the reaction and K_m is the Michaelis Menten constant equal to the analyte concentration at which the reaction rate is half of V_{max}. By combining Equations 4.4 and

4.5a, current signal can be expressed as the Equation 4.6 that shows signal's dependence on the analyte concentration.

$$I = nF\frac{V_{max}\cdot[A]}{K_m+[A]} \qquad \text{(Equation 4.6)}$$

The measured current signal resulting from the change in glucose, lactate, or glutamate concentration at the enzyme-modified electrodes generates analytical data as current vs time. This data can be translated in terms of analyte concentration and exposure time, providing information on metabolic activities in real-time.

4.3. Microclinical Analyzer Modeling using COMSOL

Modeling of convective-diffusive-reactive transport in μCA, including enzymatic reaction on the sensor surface, was conducted using COMSOL Multiphysics (Burlington, MA).

4.3.1. Geometry for the metabolite detection

Chemical transport was modeled through two μCAs (Radius = 6 mm, Height of each chamber = 0.23 mm, volume = 26 μL) and three electrode heads (area = 1.8 mm^2) on the bottom of the chamber surface. Two μCAs were connected with 150 mm tubing where the upstream μCA chamber mimicked the cell chamber and the downstream μCA chamber represented the sensor chamber (see Figure 4.1). Such arrangement with two μCAs also allowed for comparative analysis of in situ and downstream signals.

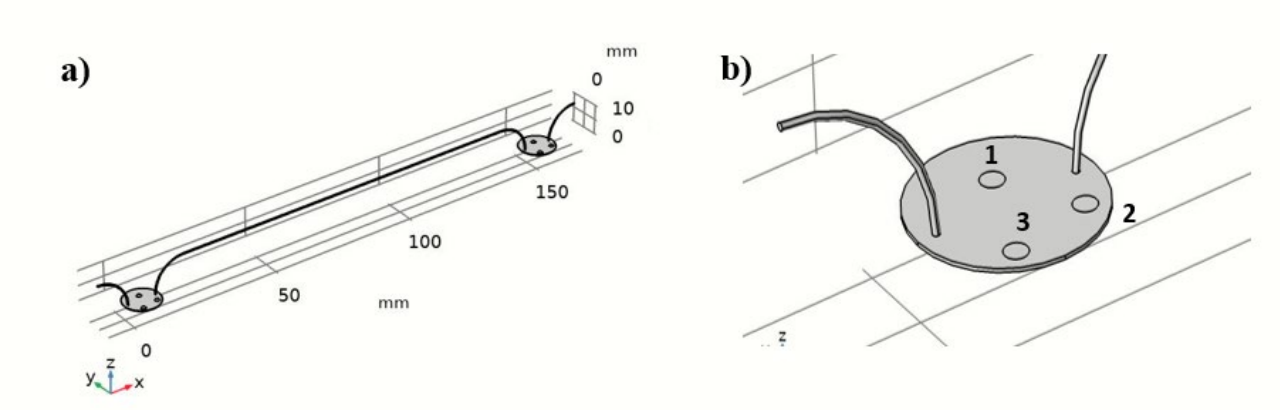

Figure 4.1 a) COMSOL geometry of two µCAs (radius = 6 mm, height of each chamber = 0.23 mm) connected with 150 mm tubing – upstream chamber mimicked the cell chamber and the downstream chamber mimicked the µCA; b) circular section in the chamber shows circular area of three electrodes (area = 1.8 mm^2).

4.3.2. Modeling enzymatic reaction in µCA

For enzyme-based metabolite detection, the geometry was extended to include the Michalis Menten type metabolic reaction around the sensor surface area. The geometry was slightly modified by adding a cylindrical volume just above the sensor electrodes to create the volume required to allow the Michalis Menten type metabolic reaction to take place (Figure 4.2). The layer thicknesses were simplified by making a best guess of the enzyme height of 40 µm. The additional Nafion layer is neglected in the model. This added reaction feature of computational model simulated the cylindrical volume above the electrodes for the enzymatic reaction: $[A] + [E] \underset{k_R}{\overset{k_F}{\Leftrightarrow}} [EA] \xrightarrow{k_{cat}} [P] + [E]$.

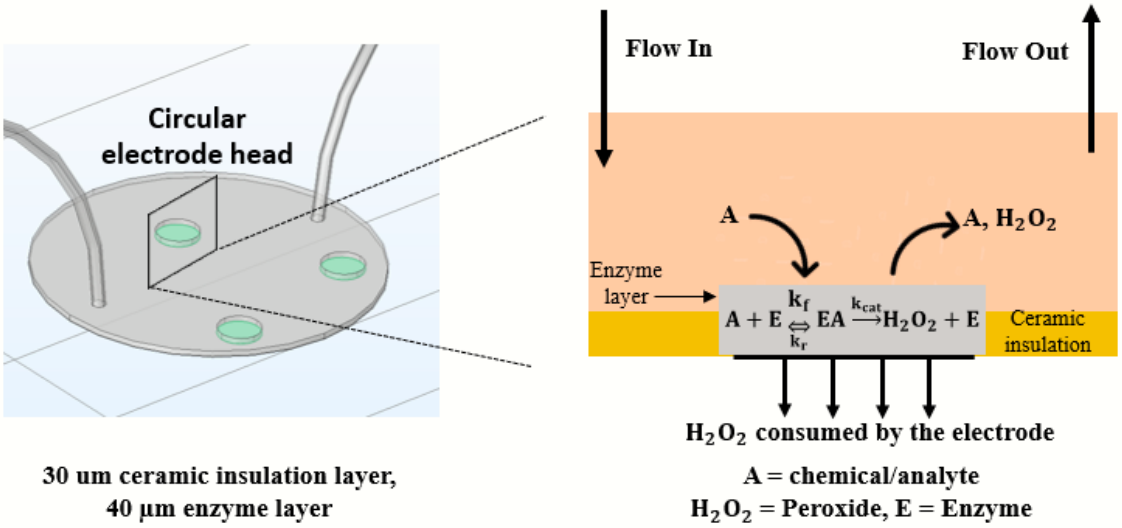

Figure 4.2 Modeling enzymatic layers for metabolite detection: three enzymatic sensor electrodes placed on the bottom of the µCA (left); simple 2D schematic showing the enzyme layer on the top of the electrodes where the Michaelis Menten type reaction occurs and produced peroxide gets consumed by the electrodes (right).

4.3.3. Boundary conditions

The modeling was performed using a number of boundary conditions to mimic the cellular consumption and the sensor. The sensor surface boundary condition is set to zero concentration based on ideal sensor theory[107], indicating complete consumption of analytes by the sensor electrodes (Figure 4.3). Isothermal condition was assumed throughout the modeling, with convective flux boundary conditions specified at both device inlet and outlet. In the solution phase, diffusion coefficients of glucose, lactate, glutamate, and peroxide were taken from the study of Velkovsky et al (2011). In the porous enzyme layer, diffusivities of these chemicals were assumed to be significantly low as reported in the literature[108–110].

Measurement with µCA is performed under two flow conditions: stop-flow and continuous flow[48,111]. For modeling continuous perfusion of analytes, steady state fluid field was used, and for

stop-flow perfusion, transient state fluid field imposed. A brief discussion on these two types of perfusion has been in included in the supplementary document (S.4).

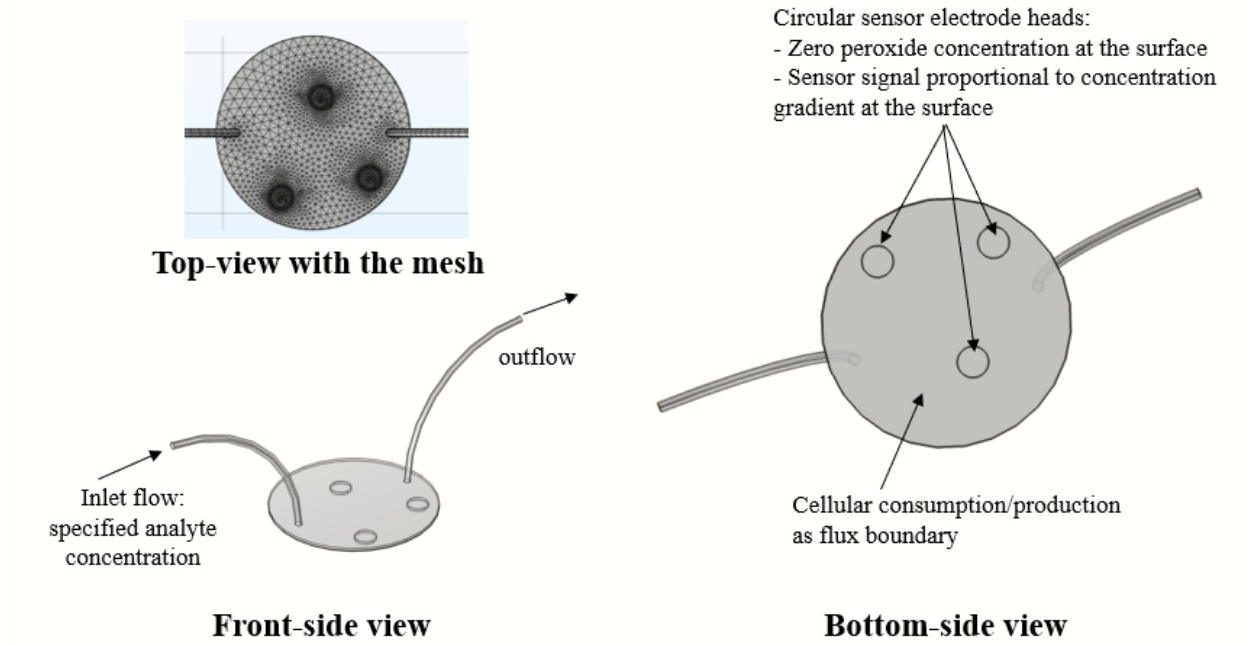

Figure 4.3 Mesh and boundary conditions to model transport in µCA. Fine fluid dynamics meshing was applied to the geometry, including µm-scale size of the mesh elements on the sensor surface (top view); convective flux boundary conditions specified at both device inlet and outlet (front view); boundary condition was set to zero concentration of peroxide at the sensor surface, assuming complete consumption by the electrode, cellular consumption or production was set as a flux across the bottom surface of the µCA.

The transport of chemical species i from the cell chamber to the sensor chamber can be defined as convective-transport-reaction equation: $\frac{\partial C}{\partial t} = D_i \Delta^2 C_i - u\Delta C_i + R$, which is very similar to Equations. 2.4 and 2.5. The reaction term R is a sink (or source) term representing cellular consumption (or production) rate for glucose/glutamate (or lactate). The consumption of glucose and glutamate were defined as the molar flux (mol/m^2.sec) at the electrode surface and those terms were normalized with the initial concentration. Lactate production terms was defined as a function of glucose production rate, including a degree of anaerobicity (x%) of the cellular

microenvironment[1,112]. One mole glucose can convert to two moles of lactate in anerobic condition. This reaction can be defined by Equation 4.7, and the lactate flux can be written as the Equation 4.8.

[glucose] → 2[lactate]: $\frac{d[G]}{dt} = -2\frac{d[L]}{dt}$ (Equation 4.7)

$\text{Flux}|_{\text{lactate}} = \text{Flux}|_{\text{glucose}} \times 2 \times x\%$ (Equation 4.8)

The enzymatic reaction was modeled within the volume section defined as enzyme layer. The peroxide concentrations were used as sensor signals by taking integration over its consumption flux across the electrode surface.

The modeling scheme was validated by simulating a simple consumption experiment in μCA and by reproducing the experimental signals. This proof-of-concept study (Supplementary S.5) successfully demonstrate the potential of computational development of transport through μCA.

4.4. Estimation of Kinetic Parameters for Enzymatic Reaction

The modeling of enzymatic reactions needs the kinetic parameters such as K_m and V_{max}. Such parameters are often extracted by fitting to the experimental calibration plots (signal vs analyte concentration)[46,111]. The measured signal depends on the degree at which peroxide produces and reaches to the electrode surface, and thus combines the contribution of the reaction kinetics and the transport kinetics of peroxide. If kinetic parameters are obtained from the such experimental data, those are not fully predictive of the enzymatic reactions – more of a representation of the combined kinetics of the enzymatic reactions and the transport of peroxide

on the surface of the electrode, overestimating the reaction parameters. In an effort to find the reaction kinetic parameters, an additional numerical analysis has been performed.

The Nelder-Mead simplex method[113,114] is a commonly applied direct search method used to find the minimum or maximum of an objective function in a multidimensional space. In this work, computational modeling for glucose, lactate, and glutamate sensors were performed iteratively with best, next-to worst, and worst guessed K_m and V_{max} values. For each set of parameters, it was possible to model the calibration plots similar to the those of the previous studies. The objective function was defined as the goodness to fit (sum of squared residual) of the modeled calibration plots with the experimental data points (see Figure 4.4). The iterations were continued until the objective function minimized, and the parameters were selected from the final iteration. The estimated kinetic parameters were slightly lower than those reported in the published study (see Table 4.1).

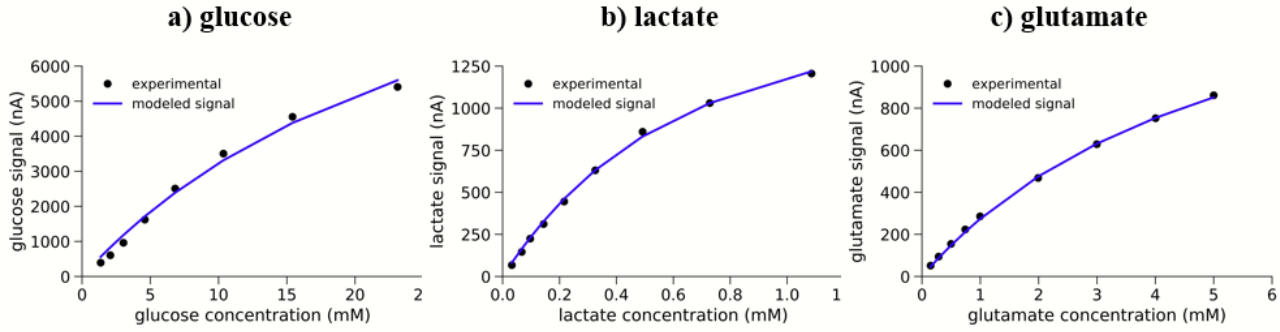

Figure 4.4 Using Nelder-Mead Simplex method of kinetic parameter search. Calibration data points from the experiments were fitted to find out the Michaelis Menten kinetic parameters for a) glucose, b) lactate, c) glutamate.

For a given chemical, data from the calibration experiments were fitted to the Equation 4.6 and goodness-to-fit was assessed for comparing with the quality of the literature results and this numerical approach. These results were compared with those obtained from the numerical analysis

as shown in the Table 4.1. The details of the numerical method and the iteration results have been included in the supplementary figure (S.6) and tables (S.7, S.8, S.9). The K_m and V_{max} values of the enzymatic reactions appeared to be smaller than those from the literatures, implying that these parameters described the sole contribution of Michalis Menten type enzymatic reactions. This numerical approach for finding the reaction kinetic parameters appears to be convincing with the improved goodness to fit – making those parameters appropriate for the modeling of enzymatic reactions, mimicking glucose, lactate, and glutamate sensors within μCA.

Table 4.1 Estimation of reaction kinetic parameters: Nelder-Mead Simplex method was used to search the kinetic parameters for the enzymatic reactions. In this work, parameters were estimated using iterative modeling approach, and compared with those reported in previous studies[46,111]. The approach taken here appears as a means to improve the prediction of parameters as evident by the goodness to fit values.

Parameter	Glucose		Lactate		Glutamate	
	Melow et al (2020)	Nelder-Mead Method	Melow et al (2020)	Nelder-Mead Method	Miller et al (2018)	Nelder-Mead Method
K_m (mM)	33	24.7	0.67	0.42	5.3	4.86
V_{max} (mM/sec)	1.02	1.57	0.14	0.23	2.13	0.22
Goodness to fit	263900	251714	3895	1983	417	583

4.5. Downstream Metabolite Detection for Continuously Perfused System

Microclinical analyzer can be used under the continuous flow condition. With continuous perfusion with buffer, chemicals along with the buffer are injected as pulse input and changes in signal can be observed due to the exposure.

4.5.1. Predicted impact of flowrates in continuous perfusion

In the real-time measurement of analytes using microphysiometer and μCA, calibrations are often done at high flow rate, but experiments are run at low flow rates[46,48,54,111]. It is important to understand the degree to which a calibration done at one flow rate is valid at other flow rates.

To analyze the consequence of calibration at different flow rates, glucose sensor has been modeled and calibration curves were generated at various concentrations ranging from 1 to 25 mM and under the continuous flow condition of 10, 20, 100 µL/min (Figure 4.5).

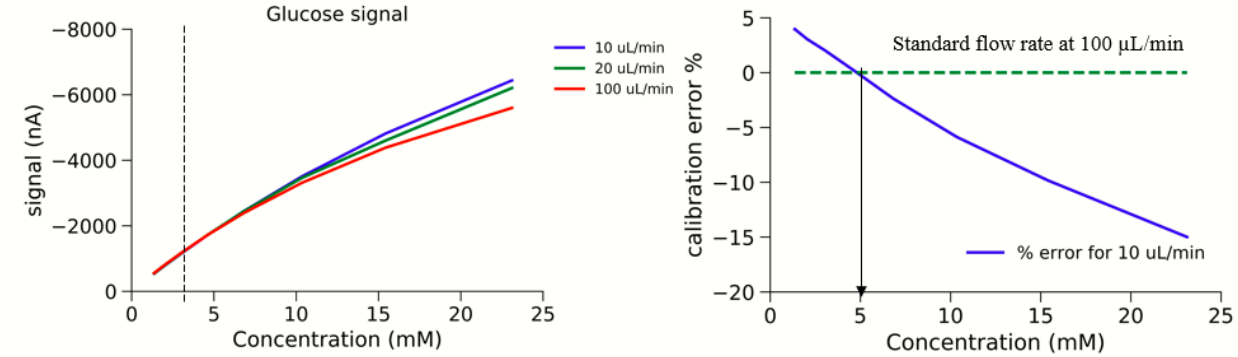

Figure 4.5 Calibration plot (Concentration vs time). (left) Variation in flow rate impacted the calibration curve. The impact is higher at high concentration. (right) For high concentration, measurement at low flow rate is subject to calibration error up to 15%.

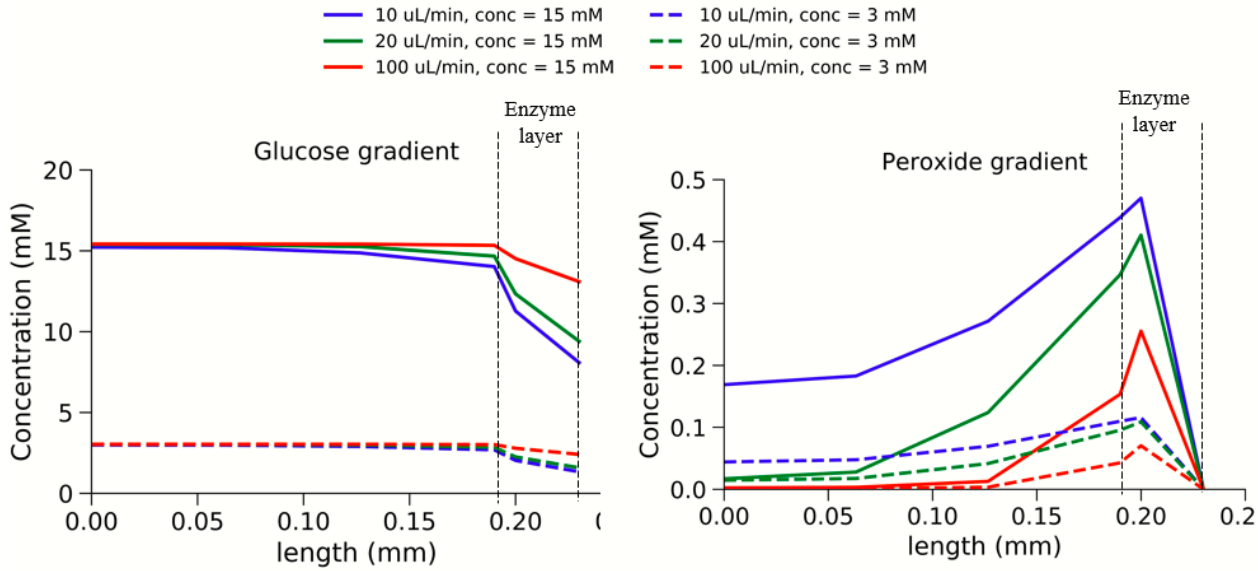

Figure 4.6 (left) glucose gradient across the enzyme layer. (right) peroxide gradient across the enzyme layers.

At low concentrations (<5 mM), modeled glucose signals were found to be slightly higher at high flow rate (100 µL/min), but at higher concentrations (>5mM), signals were higher at low

flow rates (10, 20 μL/min). This behavior is like to be attributed to the availability of glucose for the enzymatic reaction and peroxide production rate (Figure 4.6). Higher flow rate causes higher supply of chemicals and low flow rates provides higher residence time for the reaction to happen. At low concentration, higher flow rates yield higher signal due to faster availability of the glucose. At high concentration, lower flow rate causes higher residence time for more peroxide production, increasing the signal. If the flow rate of 100 μL/min is considered as standard one, calibration at 10 μL/min would cause an error up to 15% at higher concentration (Figure 4.5).

4.5.2. Modeling Crosstalk in Metabolite Sensing

Microclinical analyzer is a multianalyte system, offering a platform for simultaneous measurement of different analytes, for example, real-time measurement of cellular consumption of glucose as well as its production of lactate at the same time. In the enzymatic reaction, such measurements are done by evaluating the peroxide consumption at the electrode surface, not the original analytes such as glucose or lactate. So, the peroxide produced in glucose sensor might interfere with the signal generated in the lactate sensor and vice versa. Such cross-talk has been modeled here.

In order to investigate any possible signal crosstalk, a glucose and a lactate sensor have been modeled within the same μCA. Sensors were specified in two different arrangements: two sensors in the same side of the flow and in the opposite side of the flow (Figure 4.7). For both arrangements, lactate sensor was kept behind the glucose signal, assuming physiologically relevant higher glucose signals are more subject to interfere with comparatively weaker lactate signal.

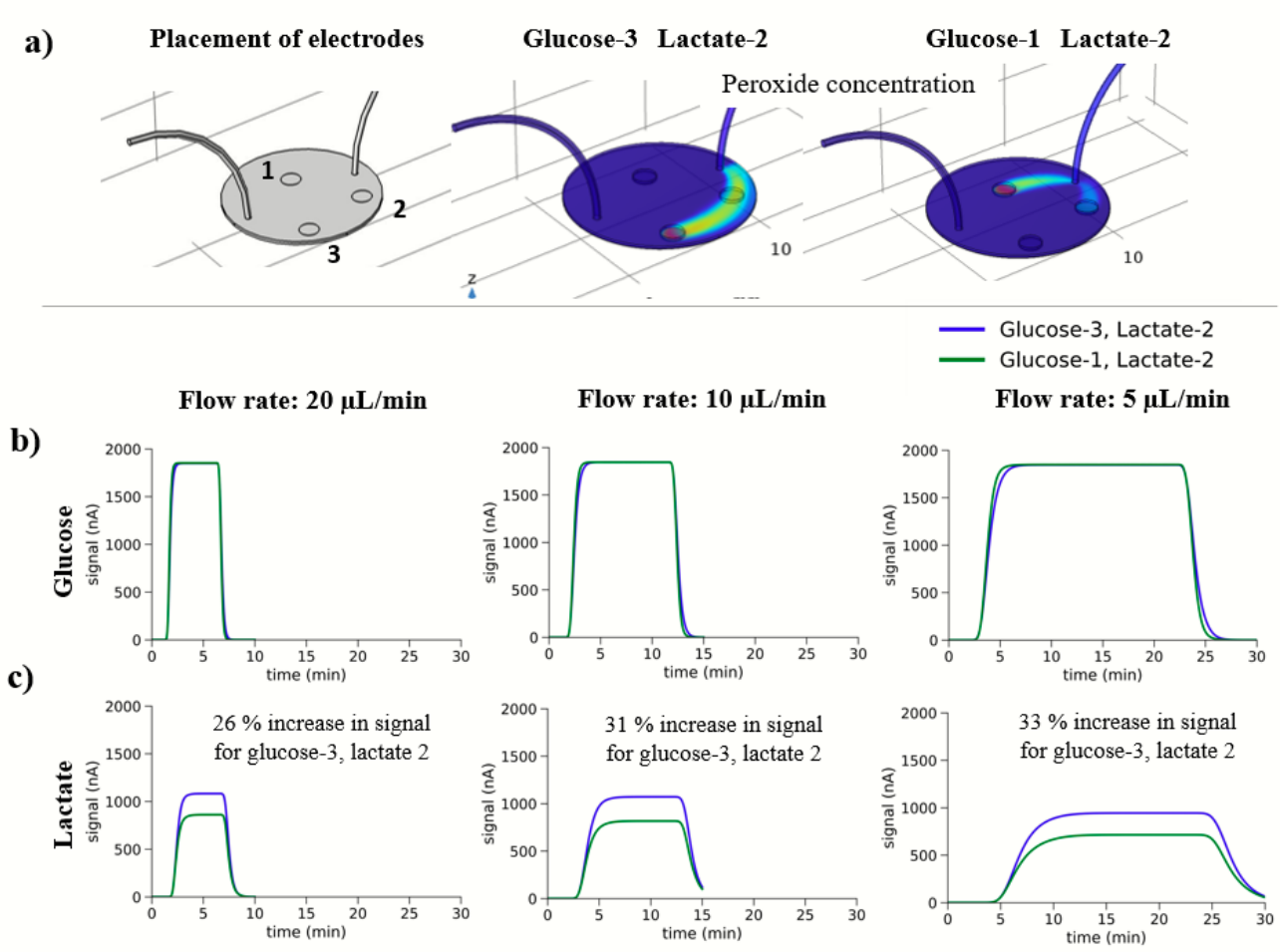

Figure 4.7 The change in signal resulting from the consumption of glucose and production of lactate are measured simultaneously and plotted as signal vs time. In the arrangement where two electrodes are positioned at the same side of the flow, the glucose signal interfere and increase the lactate signal more than 20%, even higher with lower flow rate.

Modeling was performed with the injection of 5 mM glucose, and 0.5 mM lactate (mimicking on and off with appropriate buffer solution) and under flow conditions of 20 µL/min with 5-min pulses, 10 µL/min with 10-min pulses, and 5 µL/min with 20-min pulses. There is no discernible change in glucose signals in any of the arrangement of sensors. but the lactate signal was found to increase when placed at the same side of the glucose sensor. Lactate signal was found to increase by 26, 31, and 33% under the flow condition of 20, 10, 5 µL/min, respectively. Peroxide produced in the upstream glucose sensor interfered with that produced in the downstream lactate

senor and overestimated the lactate signal. However, other possible arrangements with glucose and lactate sensor were modeled too, but the results were not presented here because of no evidence of crosstalk between sensors signals in those arrangements.

4.5.3. Modeling Downstream Glutamate Consumption

It have been experimentally observed that the μCA is an easy-to-use and versatile sensor for the in-situ monitoring of cellular response to glutamate [46]. Miller et al. (2018) reported μCA's use for the glutamate detection by immobilized enzyme glutamate oxidase on a platinum-disk electrode colocalized with the neuronal cells. When the cells were incorporated within the μCA, the glucose starved cells took up to an average of 210 nmoles of glutamate during the exposure for 30 minutes at 20 μL/min. The system thus allowed for quantitative real-time measurement of in-situ cellular bioenergetics.

While the in-situ measurement appears promising, the design of μCA requires further testing to evaluate its potential in downstream detection by the effluent from the various organotypic culture within upstream OCMs. In this work, a glutamate consumption model has been developed using COMSOL to simulate two μCAs (μCAs) – representing one as upstream cellular chamber (mimicking glutamate consuming cells) and the other one downstream μCA for the downstream detection (Figure 4.8). Modeling was performed with the injection of 1 mM glutamate (on and off with appropriate buffer solution) and under flow condition of 20 μL/min with one 30-min pulse. Cellular consumption was mimicked as flux boundary condition at the bottom of the chamber surface, assuming cells are spread on the bottom of the chamber. The consumption flux was calculated from the experimentally found cellular uptake of average of 210 nmoles of glutamate[46]. Glutamate detection was modeled as enzymatic reaction occurring in an

appropriate thickness of enzyme layer on the top of the electrodes. The enzymatic reaction produced peroxide that translates into the signal on the electrode surface.

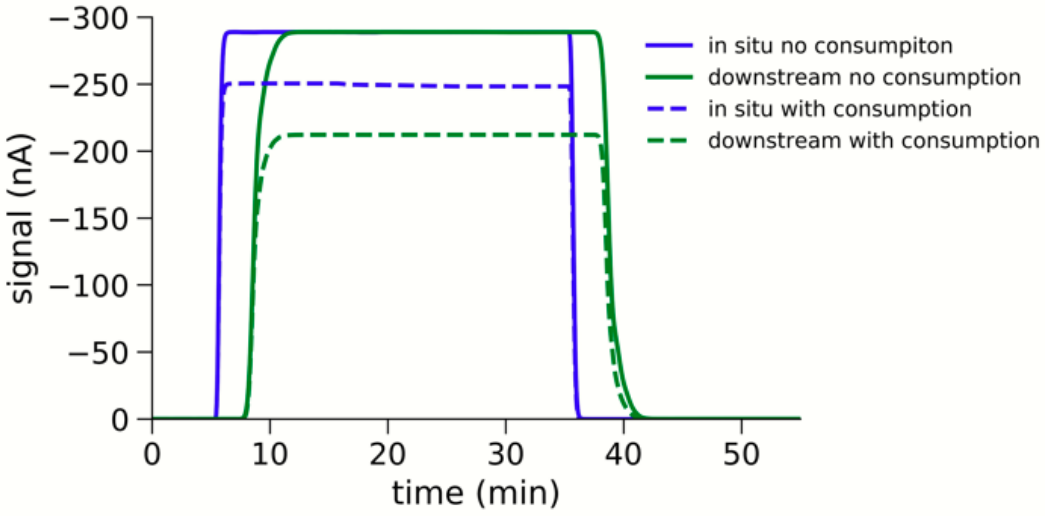

Figure 4.8 downstream detection of glutamate uptake by neuronal cells under continuous flow condition. Model showed that *in situ* cellular uptake of glutamate is 177.5 nmoles compared to downstream measurement of 177 nmoles.

Glutamate was injected at a concentration of 1 mM. Without cells in the chamber the current signal was found to be 290 nA which is consistent with the calibration curves. Due to the cellular uptake of glutamate, the in-situ signal was found to be 248 nA and the downstream signal was 212 nA. In-situ and downstream both signals were calculated and compared for evaluating uCA's potential for using as downstream detection device. Modeling outcome appears fairly consistent with the experimental observation. Model observation showed that total cellular uptake of glutamate is 177.5 nmoles compared to experimental consumption of 210 nmoles. The consumption flux used in the model was normalized by the glutamate concentration inside the chamber (normalization factor = $\frac{glutamate\ conc|_t}{glutamate\ conc|_{t=0}}$) – that yields a slight difference in total consumption in situ. The total consumption was then evaluated from downstream current signal

which is 177 nmoles, similar to the in-situ measurement. So, given the flow condition and exposure time, it was possible to simulate the experimental consumption in situ and to detect the glutamate consumption downstream of the cellular chamber without any discrepancy.

4.6. Modeling Metabolite Signals in Stop-flow Perfusion

In previous studies, microphysiometer was used with stop/flow pump cycle to periodically supply the analytes for *in situ* detection. In this work, effort has been made to model μCA with stop-flow protocol for downstream measurement of glucose and lactate. The model tested with stop-flow cycles of 200s on/40s off and 80s on/40s off at 100 μL/min to estimate concentrations of glucose and lactate.

Similar to the continuous flow system, the model geometry included two μCAs connected with 150 mm tubing where the upstream μCA chamber mimicked the cell chamber and the downstream μCA chamber represented the sensor chamber (μCA). (Figure 4.1). Glucose consumption flux was assumed to be $5 \times 10^{-6}\ \frac{mol}{m^2 sec}$ and 10% anaerobic lactate production was considered. Two different flow protocols have been tested, complete 6 stop-flow cycles of 80s on/40s off and 200s on/40s off at 100 μL/min. Glucose consumption has been modeled to decrease gradually from 100% to 25% in the first 4 cycles, and consumption was set to zero to mimic dead cells in the last 2 cycles. Lactate production was also set to zero in the last 2 cycles (Figure 4.9).

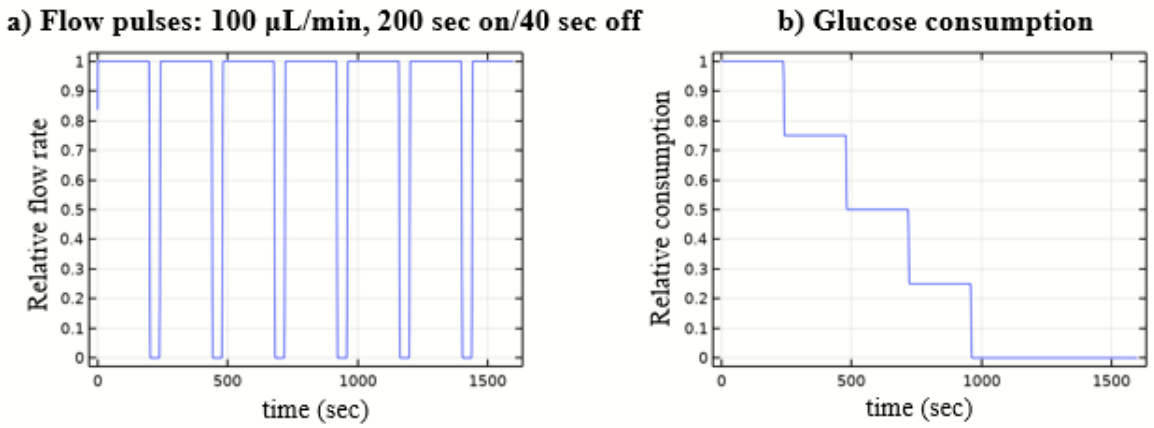

Figure 4.9 a) stop/flow protocol of 6 cycles with 200s on/40s off at 100 µL/min. b) glucose and lactate flux with rates decreasing with time to simulate live-cell environment and no rates in last two cycles mimicking dead cells

During the flow phase peroxide produced from the enzymatic reaction of glucose and lactate, but the peroxide flushed away leaving the signal as baseline. With the available glucose and lactate, during the stop phase, an increase in the glucose signal occurred due to the accumulation of produced peroxide at the electrode surface. Once the medium from the cell culture area passes the electrode, the lactate signal increases due to the lactate produced by the cells during the stop phase. The glucose signal dropped in the flow phase (starting from the 2nd cycle) due to the consumption on the upstream cell chamber in the prior stop phase. The sharp rise of the lactate signal in the stop phase occurred due to the production of the lactate in the stop phase of the prior cycle. This behavior can be observed in Figure 4.10 and Figure 4.11. The rise/drop of the glucose and lactate peaks is a distinct characteristic signal that the downstream measurement was able to capture. Here the lactate production and glucose consumption during the stop phase can be determined by the peak height in the flow phase. However, the baseline is slightly increasing the glucose signals in successive cycles.

To calculate the glucose consumption rate in one cycle, one needs to consider the baseline of the same cycle. In the first cycle, total consumption rate 0.54 nmoles/sec based on nominal concentration. The measurement through *in situ* detection is 0.45 nmoles/sec, taken as current change over time. From the downstream detection, the glucose signal in the stop phase was used to calculate the area under the curve which give the glucose consumption flux of 0.41 nmoles/sec. A slight discrepancy has been observed in downstream measurement.

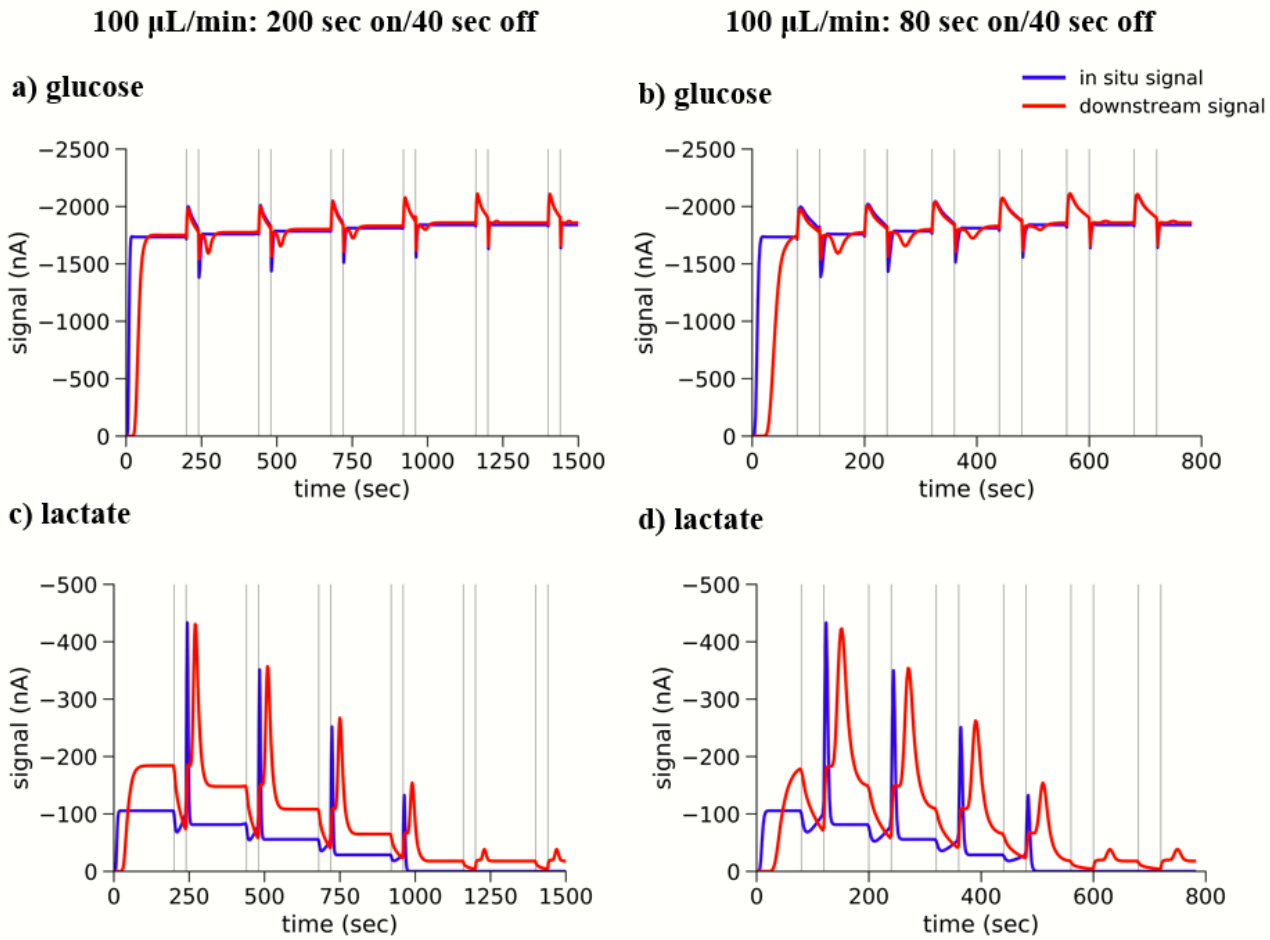

Figure 4.10 Stop/flow (100 µL/min) measurement mimicking metabolism: a, b) glucose signals in two protocols; c, d) lactate signals in two protocols - complete 6 stop-flow cycles of 80s on/40s off and 200s on/40s off at 100 µL/min. First 4-cyles was set with gradual decrease in glucose consumption, hence lactate production; last 2 cycle was set with no cellular consumption and metabolite production mimicking dead-cells; longer duration of flow phase is desirable to completely flush the system so the signals don't get overlapped as clearly evident in c and d.

Under same stop-flow protocol, the differential impacts of the duration of flow phase can be seen in Figure 4.10. For both of the protocols (80s on/40s off and 200s on/40s off at 100 µL/min), Glucose and lactate signals were clearly transient signals with longer flow phase (200s on/40s off). Although glucose signals were distinctive, lactate signals were slightly overlapped in shorter flow phase (80s on/40s off system). The minimum time of the flow has to be enough to flush the chamber completely to acquire the desired metabolic signals as observed for the 200s on/40s stop-flow protocol.

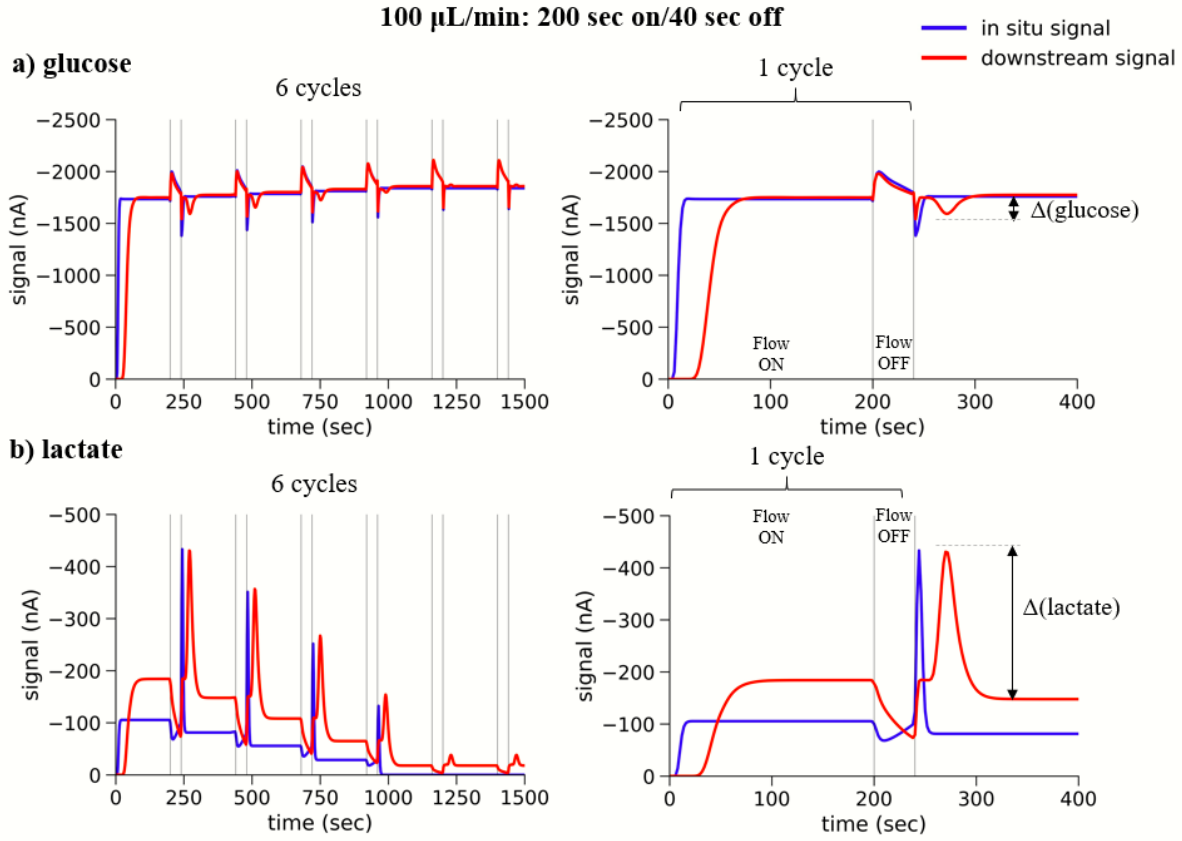

Figure 4.11 Stop/flow (100 µL/min) measurement mimicking metabolism: complete 6 stop-flow cycles of 80s on/40s off and 200s on/40s off at 100 µL/min. First 4-cyles was set with gradual decrease in glucose consumption, hence lactate production; last 2 cycle was set with no cellular consumption and metabolite production mimicking dead-cells; glucose consumption (a) and lactate production (b) during the stop phase can be determined by the peak height in the flow phase.

Additional impact arises when the flow rates were varied. The flow sensitivity is prominent with a flow rate of 100 µL/min as seen in the sharp drop in the glucose signal at the moment of stopping the flow. Unlike the high flow rate condition, when the flow protocol was changed to 15 µL/min with the same stop-flow cycles (200s on/40s off), the flow sensitivity was decreased (Figure 4.12). Sharp transient signals were no longer available in the measurement under the low flow rate.

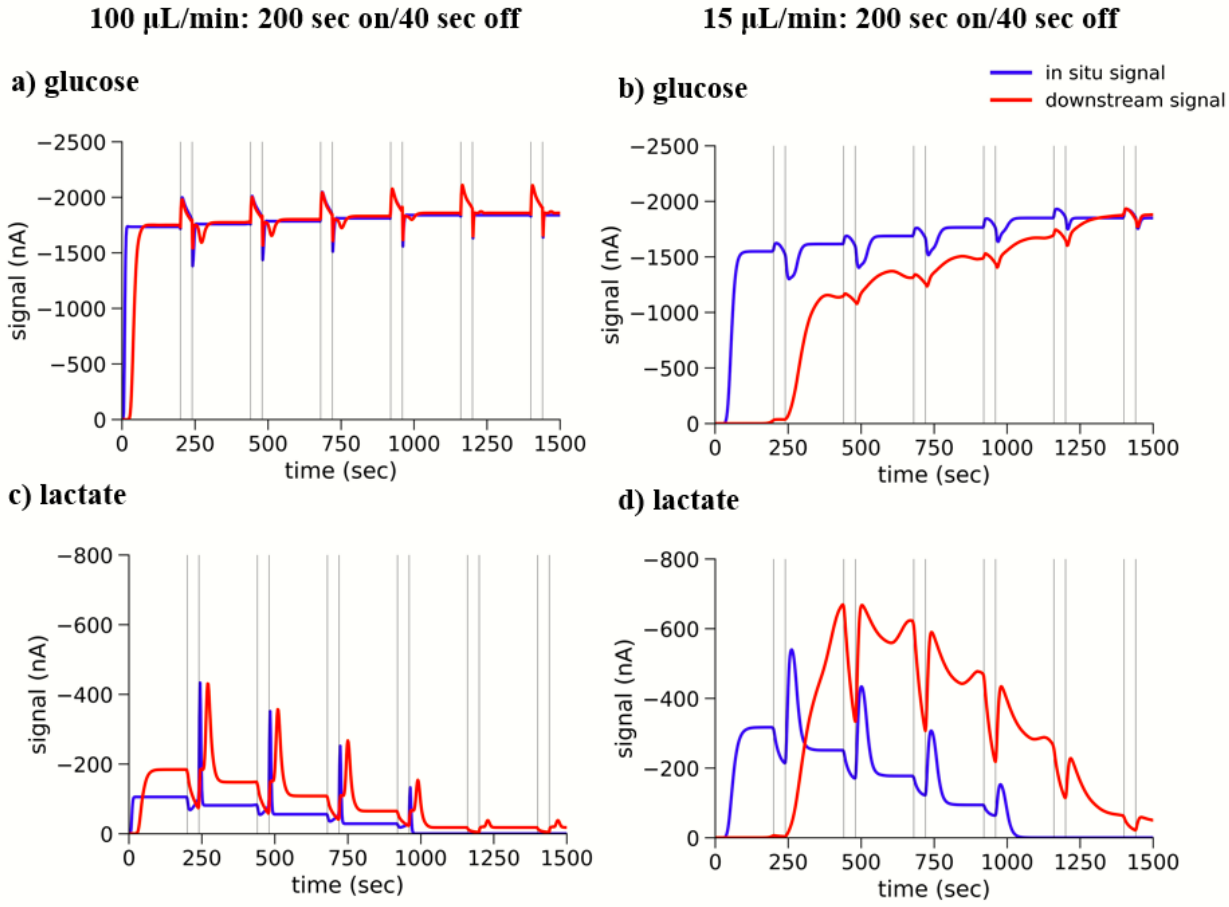

Figure 4.12 Impact of flow rates under same stop/flow protocol. The flow sensitivity is prominent with a flow rate of 100 µL/min as seen in the sharp drop in the glucose signal at the moment of stopping the flow. Unlike the high flow rate condition, when the flow protocol was changed to 15 µL/min with the same stop-flow cycles (200s on/40s off), the flow sensitivity was decreased; with low flow rates, the sharp peaks were no more observed. 15 µL/min appears to be much slower flow for the complete flush in the flow phase, resulting is overlapped signal for lactate.

In this modeling effort, a µCA was used as a representative cell chamber upstream. It also allowed us for evaluating in-situ measurements to compare with the downstream signals. However, the first chamber could be a wide variety of organotypic cultures from OCMs with much lower volume[16,17,19]. In the modeling, the first chamber geometry was modified to get a volume half of the original volume (original µCA volume = 26 µL. reduced volume = 13 µL). By doing this, it was possible to investigate how the size of the upstream chamber effects the downstream signals. With half of the original volume of the first microchamber, both glucose and lactate signals increased around 40%, as seen in the Figure 4.13.

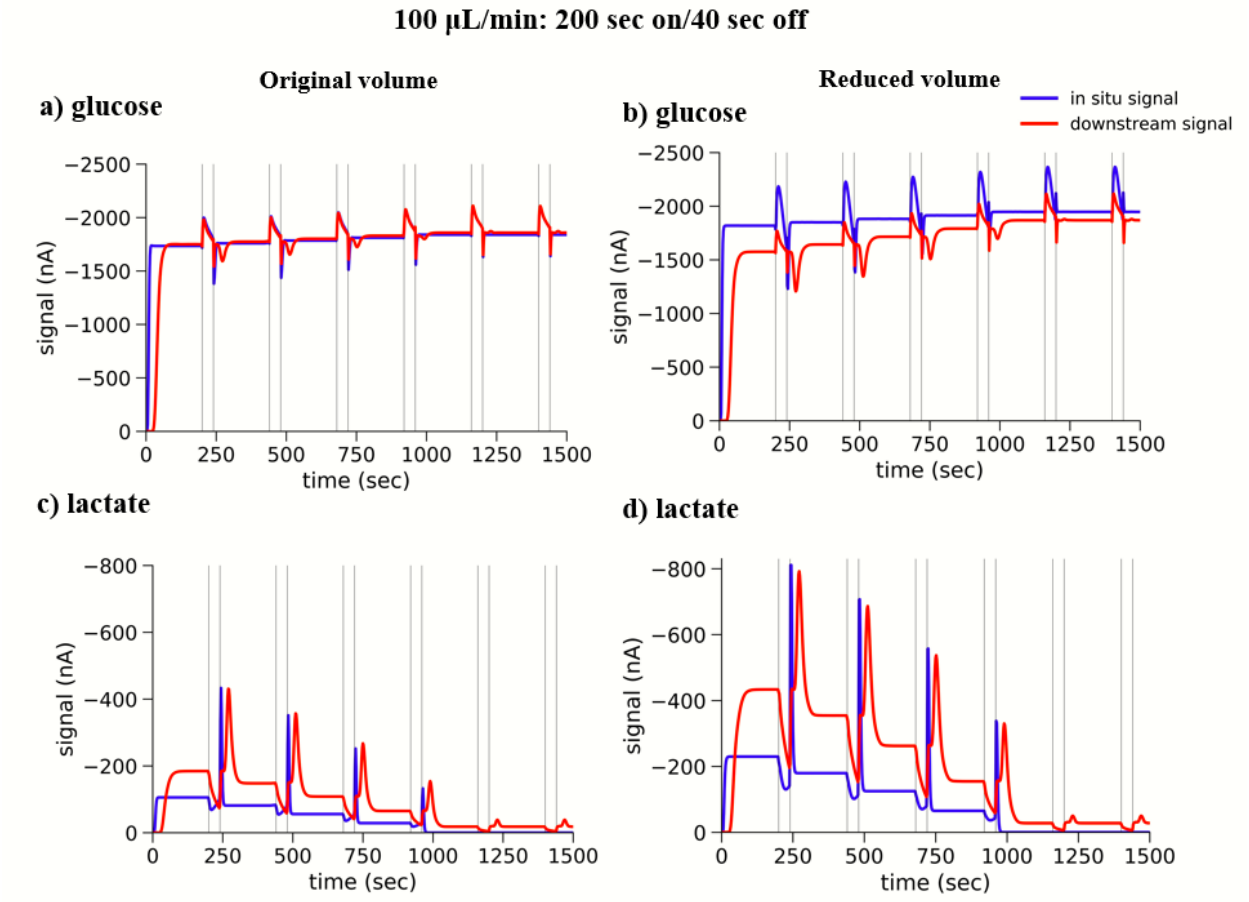

Figure 4.13 Impact of the size of the upstream chamber: a, b) glucose signal. c. d) lactate signal. with a cell chamber volume (original volume = 26 µL. reduced volume = 13 µL), reduced to half of the original upstream chamber, glucose and lactate signals increased around 40%.

4.7. Discussion

A computational framework has been developed that is capable of modeling the dynamics of *in situ* and downstream measurement using μCA under continuous and stop-flow conditions. A numerical technique has been employed to accurately predict the kinetic parameters needed to model the enzymatic reactions. The modeling of metabolic signals under continuous perfusion focused on few previous studies. The goal was to recreate some of the previous studies and extend those to the application of μCA. This approach will be a guide to the design and protocol for future application of μCA. The results showed that *in situ* and downstream consumption using μCA were consistent under continuous exposure at 20 μL/min. In the previous studies, calibrations are often done at 100 μL/min, when the actual measurement are conducted at much lower flow rates[46,111,115]. The model showed that the calibration curve generated at 10 μL/min is only valid for 100 μL/min at low concentration. In the situation where higher concentration of chemicals is relevant, the decision of choosing the flow rates for experiments and calibration is critical. For simultaneous measurement of glucose consumption and lactate production, one has to be aware of the placement of sensors in the μCA. Glucose signals are usually very large that may cause interference with lactate signals which is what happened in one of the modeling investigations. When their respective sensors were located at one side of the chambers, modeled lactate signal was overestimated due to the crosstalk with glucose signal.

The modeling of metabolic signals under stop-flow condition included various aspects that could impact the measurements. Depending on the flow rate, the duration of the flow phase has to be designed to avoid the overlapping of the signals. A reasonable combination of higher flow rate and longer duration in flow phase is desirable to yield distinct signals with sharp peak, allowing its ability to evaluate the cellular rate. Such cellular rate evaluated from the downstream signal

showed slight discrepancy, may be arising from the diffusional spread. The size of the upstream chamber also has impact on the downstream signal. With lower volume of the cell chamber, the downstream signals are clearer and more distinctive.

4.8. Conclusion

A detailed computational framework has been developed for the detection of cellular metabolism using microclinical analyzer. *In situ* and downstream measurement under different flow conditions were modeled. This predictive modeling provides an understanding of the various factors (flow rates, stop/flow protocol, size of the upstream cell chamber, positioning of sensors for simultaneous measurement) that affect measured signal. In addition, a technique has been established to extract the kinetic parameters for cellular metabolism, which is critical to accurate measurement. Microclinical analyzer showed promises in evaluating the cellular metabolic rates as well. This can be successfully used to determine the metabolic response of different organotypic cultures of organ-on-chip microsystem connected with it, and can potentially play an important role in the assessment of drug and chemical toxicity on organ-on-chip platform.

CHAPTER 5

CONCLUSIONS AND FUTURE DIRECTIONS

5.1. Conclusions

In the screening of chemical toxicity, the strength of organ-on-chip microsystems relies on their ability to reproduce cellular microenvironment – which poses some challenges on how to predict in-device toxicokinetics and how to detect cellular metabolic changes in response to toxic exposure. These research questions were computationally explored in the dissertation.

Under aim 1, a toxicokinetic model was developed that demonstrated how to model the impact of chemical-PDMS interactions to estimate in-device cellular exposures in organ-on-chip microsystems. Chemical-PDMS interactions were assessed for the wider range of chemicals to describe their partitioning into PDMS, as well as chemical sequestration via reaction rates and chemical-specific carrying capacities were quantified and readily measurable parameters. These parameters were used in computational fluid dynamics models to predict in-device effects of PDMS-chemical interactions on chemical bioavailability. This research provided new insights into how one can quantify and account for chemical-PDMS interactions to calculate in-device toxicokinetics. The modeling strategies, once optimized and validated against real measurements, could be widely adopted in the field of polymer-based microfluidics for the improved prediction of human-chemical dose responses using organ-on-chip microsystems.

At the end of aim 2, a detailed computational framework was developed for the detection of cellular metabolism via enzyme-based sensors in microclinical analyzer. *In situ* and downstream measurements under different flow conditions were modeled. This predictive modeling provided an understanding of the various factors that affect measured signal. In addition, a technique was

established to extract the kinetic parameters for cellular metabolism, which is critical to the accurate measurement. Microclinical analyzer showed promises in evaluating the cellular metabolic rates as well. This computational approach allows for further analysis and testing of application of microclinical analyzer. If the model predicts any detection limitation for using sensors downstream of the cellular construct, this can be computationally explored to identify the alternative operating conditions for improved detection with higher spatiotemporal resolution. This computational effort will guide the researchers on design improvement for the next generation device for metabolite detection for its application to organ-on-chip microsystems.

5.2. Future Directions

5.2.1. In-device toxicokinetics

In the model development of in-device toxicokinetics, some challenges have surfaced in performing the validation experiments. The extended modeling approach worked well for disk soak and channel soak experiments, but was not validated against channel flow model with measurements in perfused organ-on-chip devices. The original modeling approach considered a compound surface binding capacity that cannot separate the contribution of chemical binding onto PDMS surface and diffusion of that chemical into PDMS bulk. The binding capacities for some of the chemical in the prior work were too large to represent a true surface carrying capacity which implies a significant diffusion into the PDMS bulk. Thus, the combined contribution of surface partitioning and diffusion into the PDMS bulk may be an inadequate descriptor of the appropriate phenomena involved in chemical-PDMS interaction in different time and length scales.

This discrepancy led to further analysis on how the model can be extended and validated with the experimental observation. Instead of using the prior modeling approach with compound

surface binding parameter, a hybrid model should be developed that includes the distinct contribution of the binding and unbinding kinetics with more realistic surface binding capacity and the appropriate diffusion coefficient into the PDMS. This challenge certainly provides provision for future experimental approach in order to find out the diffusion coefficient for the chemicals under fluidic condition.

With appropriate diffusion coefficient experimentally measured, the model can be run with kinetic parameters to obtain the range of surface density results that needs to be consistent with experimental measurements and model observation in different length scales. The models can be compared to find out matching condition under which predicted results diverge – especially on predicting the outlet chemical concentration. The conditions under which model works across different time- and length- scale should be documented. As expected, the model with chemicals' distinct diffusion coefficients would be the appropriate ones to better complement the experiments.

Another potential future work includes the experimental approach for the assessment of surface treatment of PDMS and to examine mitigating behavior of the chemical-PDMS interaction for a wide range of chemical of interest in toxicology study.

5.2.2. Metabolite detection

In developing the computational framework for metabolite detections, two microclinical analyzer were connected so that the upstream chamber can simulate organ-on-chip device. In future, a real device could be modeled and coupled with microclinical analyzer. One of such systems is neurovascular-unit-on-chip[17], developed at the Vanderbilt Institute for Integrative Biosystems Research and Education (VIIBRE). This device replicates a vascular and neuronal chamber separated by a blood-brain barrier to control chemical transport using thin permeable

membrane. The computational approach would allow for the prediction of the chemical/metabolite transport from vascular to neuronal chamber may affect the blood-brain barrier by analyzing whether the chemical was able to cross into the neuronal chamber or if it had any effects on metabolism, and such detection of metabolism would be modeled using a downstream microclinical analyzer.

REFERENCES

1. Davis, A. N., Travis, A. R., Miller, D. R. & Cliffel, D. E. Multianalyte physiological microanalytical devices. *Annu. Rev. Anal. Chem.* **10**, 93–111 (2017).

2. Sung, J. H. *et al.* Microfabricated mammalian organ systems and their integration into models of whole animals and humans. *Lab Chip* **13**, 1201–1212 (2013).

3. Esch, M. B. *et al.* How multi-organ microdevices can help foster drug development. *Adv. Drug Deliv. Rev.* **69**–**70**, 158–169 (2014).

4. Esch, M. B. *et al.* Multi-cellular 3D human primary liver cell culture elevates metabolic activity under fluidic flow. *Lab Chip* **15**, 2269–2277 (2015).

5. Long, C. *et al.* Design optimization of liquid-phase flow patterns for microfabricated lung on a chip. *Ann. Biomed. Eng.* **40**, 1255–1267 (2012).

6. Kola, I. & Landis, J. Can the pharmaceutical industry reduce attrition rates? *Nature reviews. Drug discovery* **3**, 711–715 (2004).

7. Sung, J. H. & Shuler, M. L. In vitro microscale systems for systematic drug toxicity study. *Bioprocess Biosyst. Eng.* **33**, 5–19 (2010).

8. Abaci, H. E. & Shuler, M. L. Human-on-a-chip design strategies and principles for physiologically based pharmacokinetics/pharmacodynamics modeling. *Integr. Biol. (Camb).* **7**, 383–91 (2015).

9. Sung, J. H., Kam, C. & Shuler, M. L. A microfluidic device for a pharmacokinetic–pharmacodynamic (PK–PD) model on a chip. *Lab Chip* **10**, 446 (2010).

10. Wikswo, J. P. The relevance and potential roles of microphysiological systems in biology and medicine. *Exp. Biol. Med.* **239**, 1061–1072 (2014).

11. Zhang, B., Korolj, A., Lai, B. F. L. & Radisic, M. Advances in organ-on-a-chip engineering. *Nat. Rev. Mater.* **3**, 257–278 (2018).

12. Hutson, M. S. *et al.* Organs-on-Chips as Bridges for Predictive Toxicology. *Appl. Vitr. Toxicol.* **2**, 97–102 (2016).

13. Yu, J. *et al.* Quantitative systems pharmacology approaches applied to microphysiological systems (MPS): Data interpretation and multi-MPS integration. *CPT pharmacometrics Syst. Pharmacol.* **4**, 585–94 (2015).

14. Yu, J. *et al.* Quantitative Systems Pharmacology Approaches Applied to Microphysiological Systems (MPS): Data Interpretation and Multi-MPS Integration. *CPT pharmacometrics Syst. Pharmacol.* **4**, 585–594 (2015).

15. Vernetti, L. *et al.* Functional coupling of human microphysiology systems: intestine, liver, kidney proximal tubule, blood-brain barrier and skeletal muscle. *Sci. Rep.* **7**, 42296 (2017).

16. Gnecco, J. S. *et al.* Instrumenting a fetal membrane on a chip as emerging technology for preterm birth research. *Curr. Pharm. Des.* **23**, 6115–6124 (2018).

17. Brown, J. A. *et al.* Recreating blood-brain barrier physiology and structure on chip: A novel neurovascular microfluidic bioreactor. *Biomicrofluidics* **9**, 054124 (2015).

18. Konar, D., Devarasetty, M., Yildiz, D. V., Atala, A. & Murphy, S. V. Lung-on-a-chip technologies for disease modeling and drug development. *Biomed. Eng. Comput. Biol.* **7s1**, BECB.S34252 (2016).

19. Markov, D. A., Lu, J. Q., Samson, P. C., Wikswo, J. P. & McCawley, L. J. Thick-tissue bioreactor as a platform for long-term organotypic culture and drug delivery. *Lab Chip* **12**, 4560 (2012).

20. Wikswo, J. P. *et al.* Scaling and systems biology for integrating multiple organs-on-a-chip. *Lab Chip* **13**, 3496 (2013).

21. Toepke, M. W. & Beebe, D. J. PDMS absorption of small molecules and consequences in microfluidic applications. *Lab Chip* **6**, 1484–1486 (2006).

22. Berthier, E., Young, E. W. K. & Beebe, D. Engineers are from PDMS-land, biologists are from Polystyrenia. *Lab Chip* **12**, 1224 (2012).

23. Sia, S. K. & Whitesides, G. M. Microfluidic devices fabricated in poly(dimethylsiloxane) for biological studies. *Electrophoresis* **24**, 3563–3576 (2003).

24. Jo, B. H., Van Lerberghe, L. M., Motsegood, K. M. & Beebe, D. J. Three-dimensional micro-channel fabrication in polydimethylsiloxane (PDMS) elastomer. *J. Microelectromechanical Syst.* **9**, 76–81 (2000).

25. Yeung, T. *et al.* Effects of Substrate Stiffness on Cell Morphology. *Cell Motil. Cytoskelet.* **60**, 24–34 (2005).

26. Murphy, W. L., McDevitt, T. C. & Engler, A. J. Material as stem cell regulators. *Nat Mater* **13**, 547–557 (2014).

27. Baltussen, E., Sandra, P., David, F. & Cramers, C. Stir bar sorptive extraction (SBSE), a novel extraction technique for aqueous samples: Theory and principles. *J. Microcolumn Sep.* **11**, 737–747 (1999).

28. and, J. C. M. & Whitesides, G. M. Poly(dimethylsiloxane) as a material for fabricating microfluidic devices. (2002). doi:10.1021/AR010110Q

29. Adiraj Iyer, M. & Eddington, D. T. Storing and releasing rhodamine as a model hydrophobic compound in polydimethylsiloxane microfluidic devices. *Lab Chip* **19**, 574–579 (2019).

30. van Meer, B. J. *et al.* Small molecule absorption by PDMS in the context of drug response bioassays. *Biochem. Biophys. Res. Commun.* **482**, 323–328 (2017).

31. Wang, J. D., Douville, N. J., Takayama, S. & ElSayed, M. Quantitative analysis of molecular absorption into PDMS microfluidic channels. *Ann. Biomed. Eng.* **40**, 1862–1873 (2012).

32. Nianzhen Li, N., Schwartz, M. & Ionescu-Zanetti, C. PDMS compound adsorption in context. *J. Biomol. Screen.* **14**, 194–202 (2009).

33. Moore, T. A., Brodersen, P. & Young, E. W. K. Multiple myeloma cell drug responses differ in thermoplastic vs PDMS microfluidic devices. *Anal. Chem.* **89**, 11391–11398 (2017).

34. Shirure, V. S. & George, S. C. Design considerations to minimize the impact of drug absorption in polymer-based organ-on-a-chip platforms. *Lab Chip* **17**, 681–690 (2017).

35. Auner, A., Tasneem, K. M., Markov, D. A., McCawley, L. J. & Hutson, M. S. Chemical-PDMS Binding Kinetics and Implications for Bioavailability in Microfluidic Devices. *Lab Chip* (2019). doi:10.1039/C8LC00796A

36. Wang, J. D., Douville, N. J., Takayama, S. & ElSayed, M. Quantitative analysis of molecular absorption into PDMS microfluidic channels. *Ann. Biomed. Eng.* **40**, 1862–1873 (2012).

37. Toepke, M. W. & Beebe, D. J. PDMS absorption of small molecules and consequences in microfluidic applications. *Lab Chip* **6**, 1484 (2006).

38. Huang, M., Fan, S., Xing, W. & Liu, C. Microfluidic cell culture system studies and computational fluid dynamics. *Math. Comput. Model.* **52**, 2036–2042 (2010).

39. Adeosun, J. T. & Lawal, A. Numerical and experimental studies of mixing characteristics in a T-junction microchannel using residence-time distribution. *Chem. Eng. Sci.* **64**, 2422–2432 (2009).

40. Bhatia, S. N. & Ingber, D. E. Microfluidic organs-on-chips. *Nat. Biotechnol.* **32**, 760–772 (2014).

41. Oleaga, C. *et al.* Long-Term Electrical and Mechanical Function Monitoring of a Human-on-a-Chip System. *Adv. Funct. Mater.* **29**, 1805792 (2019).

42. McAleer, C. W. *et al.* Multi-organ system for the evaluation of efficacy and off-target toxicity of anticancer therapeutics. *Sci. Transl. Med.* **11**, eaav1386 (2019).

43. Auner, A. W., Tasneem, K. M., Markov, D. A., McCawley, L. J. & Hutson, M. S. Chemical-PDMS binding kinetics and implications for bioavailability in microfluidic devices. *Lab Chip* (2019). doi:10.1039/C8LC00796A

44. Weltin, A., Kieninger, J. & Urban, G. A. Microfabricated, amperometric, enzyme-based biosensors for in vivo applications. *Anal. Bioanal. Chem.* **408**, 4503–4521 (2016).

45. Whiteley, J. P., Gavaghan, D. J. & Hahn, C. E. W. Some factors affecting oxygen uptake by red blood cells in the pulmonary capillaries. *Math. Biosci.* **169**, 153–172 (2001).

46. Miller, D. R., McClain, E. S. & Cliffel, D. E. Electrochemical microphysiometry detects cellular glutamate uptake. *J. Electrochem. Soc.* **165**, G3120–G3124 (2018).

47. Schultz, J., Uddin, Z., Singh, G. & Howlader, M. M. R. Glutamate sensing in biofluids: recent advances and research challenges of electrochemical sensors. *Analyst* **145**, 321–347 (2020).

48. Eklund, S. E., Taylor, D., Kozlov, E., Prokop, A. & Cliffel, D. E. A microphysiometer for simultaneous measurement of changes in extracellular glucose, lactate, oxygen, and

acidification rate. *Anal. Chem.* **76**, 519–527 (2004).

49. Kimmel, D. W., LeBlanc, G., Meschievitz, M. E. & Cliffel, D. E. Electrochemical sensors and biosensors. *Anal. Chem.* **84**, 685–707 (2012).

50. Hiramoto, K., Ino, K., Nashimoto, Y., Ito, K. & Shiku, H. Electric and Electrochemical Microfluidic Devices for Cell Analysis . *Frontiers in Chemistry* **7**, 396 (2019).

51. Grieshaber, D., MacKenzie, R., Vörös, J. & Reimhult, E. Electrochemical Biosensors - Sensor Principles and Architectures. *Sensors* **8**, 1400–1458 (2008).

52. Snider, R. M. *et al.* The effects of cholera toxin on cellular energy metabolism. *Toxins (Basel).* **2**, 632–648 (2010).

53. McKenzie, J. R., Palubinsky, A. M., Brown, J. E., McLaughlin, B. & Cliffel, D. E. Metabolic multianalyte microphysiometry reveals extracellular acidosis is an essential mediator of neuronal preconditioning. *ACS Chem. Neurosci.* **3**, 510–8 (2012).

54. McKenzie, J. R., Cognata, A. C., Davis, A. N., Wikswo, J. P. & Cliffel, D. E. Real-time monitoring of cellular bioenergetics with a multianalyte screen-printed electrode. *Anal. Chem.* **87**, 7857–7864 (2015).

55. Kieninger, J., Weltin, A., Flamm, H. & Urban, G. A. Microsensor systems for cell metabolism – from 2D culture to organ-on-chip. *Lab Chip* **18**, 1274–1291 (2018).

56. Frey, O., Misun, P. M., Rothe, J. & Hierlemann, A. Real-time in-situ lactate monitoring in 3D multi-cellular spheroid cultures by using enzyme-based biosensors in hanging drop networks. in *Procedia Engineering* **87**, 96–99 (Elsevier Ltd, 2014).

57. Zhang, Y. S. *et al.* Multisensor-integrated organs-on-chips platform for automated and continual in situ monitoring of organoid behaviors. *Proc. Natl. Acad. Sci.* **114**, E2293 LP-E2302 (2017).

58. Wikswo, J. P. The relevance and potential roles of microphysiological systems in biology and medicine. *Exp. Biol. Med.* **239**, 1061–1072 (2014).

59. Saadin, K., Burke, J. M., Patel, N. P., Zubajlo, R. E. & White, I. M. Enrichment of tumor-initiating breast cancer cells within a mammosphere-culture microdevice. *Microdevices* **15**, 645–655 (2013).

60. Konar, D., Devarasetty, M., Yildiz, D. V., Atala, A. & Murphy, S. V. Lung-On-A-Chip Technologies for Disease Modeling and Drug Development. *Biomed. Eng. Comput. Biol.* **7**, 17–27 (2016).

61. Domansky, K. *et al.* Perfused multiwell plate for 3D liver tissue engineering. *Lab Chip* **10**, 51–58 (2010).

62. Bhatia, S. N. & Ingber, D. E. Microfluidic organs-on-chips. *Nat. Biotechnol.* **32**, 760 (2014).

63. Wikswo, J. P. *et al.* Scaling and systems biology for integrating multiple organs-on-a-chip. *Lab Chip* **13**, 3496–3511 (2013).

64. Jo, B. H., Van Lerberghe, L. M., Motsegood, K. M. & Beebe, D. J. Three-dimensional

micro-channel fabrication in polydimethylsiloxane (PDMS) elastomer. *J. Microeletromech. Syst.* **9**, 76–81 (2009).

65. Martin, M. T. *et al.* Predictive model of rat reproductive toxicity from ToxCast high throughput screening. *Biol. Reprod.* **85**, 327–339 (2011).

66. Klaunig, J. E. *et al.* PPARalpha agonist-induced rodent tumors: modes of action and human relevance. *Crit. Rev. Toxicol.* **33**, 655–780 (2003).

67. D., H. N. & A., F. P. Comparison of in vitro cytotoxicity, estrogenicity and anti-estrogenicity of triclosan, perfluorooctane sulfonate and perfluorooctanoic acid. *J. Appl. Toxicol.* **33**, 265–272 (2011).

68. Lau, C. *et al.* Synergistic interactions between commonly used food additives in a developmental neurotoxicity test. *Toxicol. Sci.* **90**, 508–510 (2006).

69. Yang, C., Tan, Y. S., Harkema, J. R. & Haslam, S. Z. Differential effects of peripubertal exposure to perfluorooctanoic acid on mammary gland development in C57Bl/6 and Balb/c mouse strains. *Reprod. Toxicol.* **27**, 299—306 (2009).

70. Macon, M. B. *et al.* Prenatal Perfluorooctanoic Acid Exposure in CD-1 Mice: Low-Dose Developmental Effects and Internal Dosimetry. *Toxicol. Sci.* **122**, 134–145 (2011).

71. Dixon, D. *et al.* Histopathologic Changes in the Uterus, Cervix and Vagina of Immature CD-1 Mice Exposed to Low Doses of Perfluorooctanoic Acid (PFOA) in a Uterotrophic Assay. *Reprod. Toxicol.* **33**, 506–512 (2012).

72. Biegel, L. B., Liu, R. C., Hurtt, M. E. & Cook, J. C. Effects of ammonium perfluorooctanoate on Leydig cell function: in vitro, in vivo, and ex vivo studies. *Toxicol. Appl. Pharmacol.* **134**, 18–25 (1995).

73. Markey, C. M., Luque, E. H., Munoz De Toro, M., Sonnenschein, C. & Soto, A. M. In utero exposure to bisphenol A alters the development and tissue organization of the mouse mammary gland. *Biol. Reprod.* **65**, 1215–1223 (2001).

74. Vandenberg, L. N. *et al.* Perinatal exposure to the xenoestrogen bisphenol-A induces mammary intraductal hyperplasias in adult CD-1 mice. *Reprod. Toxicol.* **26**, 209–210 (2008).

75. Bhattacharya, P. & Keating, A. F. Impact of environmental exposures on ovarian function and role of xenobiotic metabolism during ovotoxicity. *Toxicol. Appl. Pharmacol.* **261**, 227–235 (2012).

76. Quignot, N. *et al.* Characterization of endocrine-disrupting chemicals based on hormonal balance disruption in male and female adult rats. *Reprod. Toxicol.* **33**, 339–352 (2012).

77. Richter, C. A. *et al.* In vivo effects of bisphenol A in laboratory rodent studies. *Reprod. Toxicol.* **24**, 199–224 (2007).

78. Munoz-de-Toro, M. *et al.* Perinatal exposure to bisphenol-A alters peripubertal mammary gland development in mice. *Endocrinology* **146**, 4138–4147 (2005).

79. Tharp, A. P. *et al.* Bisphenol A alters the development of the rhesus monkey mammary

gland. *Proc. Natl. Acad. Sci.* **109**, 8190 LP – 8195 (2012).

80. Jenkins, S. *et al.* Oral exposure to bisphenol a increases dimethylbenzanthracene-induced mammary cancer in rats. *Environ. Heal. Perspect.* **117**, 910–915 (2009).

81. Betancourt, A. M., Eltoum, I. A., Desmond, R. A., Russo, J. & Lamartiniere, C. A. In Utero Exposure to Bisphenol A Shifts the Window of Susceptibility for Mammary Carcinogenesis in the Rat. *Environ. Health Perspect.* **118**, 1614–1619 (2010).

82. Hilakivi-Clarke, L. Maternal exposure to diethylstilbestrol during pregnancy and increased breast cancer risk in daughters. *Breast Cancer Res* **16**, 208 (2014).

83. Pei, R.-J. *et al.* Effect of prenatal and prepubertal genistein exposure on N-methyl-N-nitrosourea-induced mammary tumorigenesis in female Sprague-Dawley rats. *In Vivo* **17**, 349—357 (2003).

84. Whitsett, T. G. & Lamartiniere, C. A. Genistein and resveratrol: mammary cancer chemoprevention and mechanisms of action in the rat. *Expert Rev. Anticancer Ther.* **6**, 1699–1706 (2006).

85. Fritz, W. A., Coward, L., Wang, J. & Lamartiniere, C. A. Dietary genistein: perinatal mammary cancer prevention, bioavailability and toxicity testing in the rat. *Carcinogenesis* **19**, 2151–2158 (1998).

86. Lamartiniere, C. A. Timing of Exposure and Mammary Cancer Risk. *J. Mammary Gland Biol. Neoplasia* **7**, 67–76 (2002).

87. Tou, J. C. L. & Thompson, L. U. Exposure to flaxseed or its lignan component during different developmental stages influences rat mammary gland structures. *Carcinogenesis* **20**, 1831–1835 (1999).

88. Dieras, V. Review of docetaxel/doxorubicin combination in metastatic breast cancer. *Oncology* **11**, 31–33 (1997).

89. Magut, P. K. S. *et al.* Tunable Cytotoxicity of Rhodamine 6G via Anion Variations. *J. Am. Chem. Soc.* **135**, 15873–15879 (2013).

90. Gupta, R. S. & Dudani, A. K. Species-specific differences in the toxicity of rhodamine 123 toward cultured mammalian cells. *J. Cell. Physiol.* **130**, 321–327 (2018).

91. Comptox.epa.gov. EPA Chemical Database. *comptox.epa.gov*

92. Jewell, W. T., Hess, R. A. & Miller, M. G. Testicular Toxicity of Molinate in the Rat: Metabolic Activation via Sulfoxidation1. *Toxicol. Appl. Pharmacol.* **149**, 159–166 (1998).

93. Zhu, W. *et al.* Stereoselective toxicokinetics and tissue distribution of ethofumesate in rabbits. *Chirality* **19**, 632–637 (2007).

94. Www.t3db.ca. Toxin Exposome Database.

95. Http://sitem.herts.ac.uk/aeru/ppdb/en. Pesticide Properties Database.

96. Rothwell, J. A., Day, A. J. & Morgan, M. R. A. Experimental Determination of Octanol−Water Partition Coefficients of Quercetin and Related Flavonoids. *J. Agric. Food*

Chem. **53**, 4355–4360 (2005).

97. Gao, X. & Chorover, J. Adsorption of perfluorooctanoic acid and perfluorooctanesulfonic acid to iron oxide surfaces as studied by flow-through ATR-FTIR spectroscopy. *Environ. Chem.* **9**, 148–157 (2012).

98. Squires, T. M., Messinger, R. J. & Manalis, S. R. Making it stick: convection, reaction and diffusion in surface-based biosensors. *Nat. Biotechnol.* **26**, 417–426 (2008).

99. Gervais, T. & Jensen, K. F. Mass transport and surface reactions in microfluidic systems. *Chem. Eng. Sci.* **61**, 1102–1121 (2006).

100. Goldstein, B., Coombs, D., He, X., Pineda, A. R. & Wofsy, C. The influence of transport on the kinetics of binding to surface receptors: application to cells and BIAcore. *J. Mol. Recognit.* **12**, 293–299 (1999).

101. Lionello, A., Josserand, J., Jensen, H. & Girault, H. H. Dynamic protein adsorption in microchannels by 'stop-flow' and continuous flow. *Lab Chip* **5**, 1096–1103 (2005).

102. Vijayendran, R. A., Ligler, F. S. & Leckband, D. E. A Computational Reaction−Diffusion Model for the Analysis of Transport-Limited Kinetics. *Anal. Chem.* **71**, 5405–5412 (1999).

103. DiFilippo, E. L. & Eganhouse, R. P. Assessment of PDMS-water partition coefficients: implications for passive environmental sampling of hydrophobic organic compounds. *Environ. Sci. Technol.* **44**, 6917–6925 (2010).

104. Plessis, J. D., Pugh, W. J., Judefeind, A. & Hadgraft, J. Physico-chemical determinants of dermal drug delivery: effects of the number and substitution pattern of polar groups. *Eur. J. Pharm. Sci* **15**, 63–69 (2002).

105. Jenke, D. R. & Rabinow, B. E. Proper Accounting for Surface Area to Solution Volume Ratios in Exaggerated Extractions. *PDA J. Pharm. Sci. Technol.* **71**, 225–233 (2017).

106. Velkovsky, M., Snider, R., Cliffel, D. E. & Wikswo, J. P. Modeling the measurements of cellular fluxes in microbioreactor devices using thin enzyme electrodes. *J. Math. Chem.* **49**, 251–275 (2011).

107. Eluvathingal, S. J., Dri, N. A. N., Stremler, M. A., Cliffel, D. & Wikswo, J. P. Computational modeling of a cell-based microphysiometer. in *Proceedings of FEDSM: 2nd Joint U.S-European Fluids Engineering Summer Meeting* (2006).

108. van Stroe-Biezen, S. A. M., Everaerts, F. M., Janssen, L. J. J. & Tacken, R. A. Diffusion coefficients of oxygen, hydrogen peroxide and glucose in a hydrogel. *Anal. Chim. Acta* **273**, 553–560 (1993).

109. Tric, M. *et al.* Optical biosensor optimized for continuous in-line glucose monitoring in animal cell culture. *Anal. Bioanal. Chem.* **409**, 5711–5721 (2017).

110. Gibson, Q. H., Swoboda, B. E. & Massey, V. Kinetics and mechanism of action of glucose oxidase. *J. Biol. Chem.* **239**, 3927–3934 (1964).

111. Melow, S. L., Miller, D. R., Gizzie, E. A. & Cliffel, D. E. A low-interference, high-resolution multianalyte electrochemical biosensor. *Anal. Methods* **12**, 3873–3882 (2020).

112. Vander Heiden, M. G., Cantley, L. C. & Thompson, C. B. Understanding the Warburg effect: the metabolic requirements of cell proliferation. *Science* **324**, 1029–1033 (2009).

113. Byatt, D., Coope, I. & Prince, C. 40 Years of the Nelder-Mead Algorithm. *University of Canterbury, New Zealand* (2003). Available at: http://wayback.cecm.sfu.ca/AAS/coope.pdf. (Accessed: 1st June 2021)

114. Gavin, H. The Nelder-Mead Algorithm in Two Dimensions. (2020). Available at: http://people.duke.edu/~hpgavin/cee201/Nelder-Mead-2D.pdf. (Accessed: 1st April 2021)

115. Eklund, S. E. *et al.* Metabolic discrimination of select list agents by monitoring cellular responses in a multianalyte microphysiometer. *Sensors (Basel).* **9**, 2117–2133 (2009).

APPENDIX A Supplementary materials for Chapter 2

Supplementary Section S.1

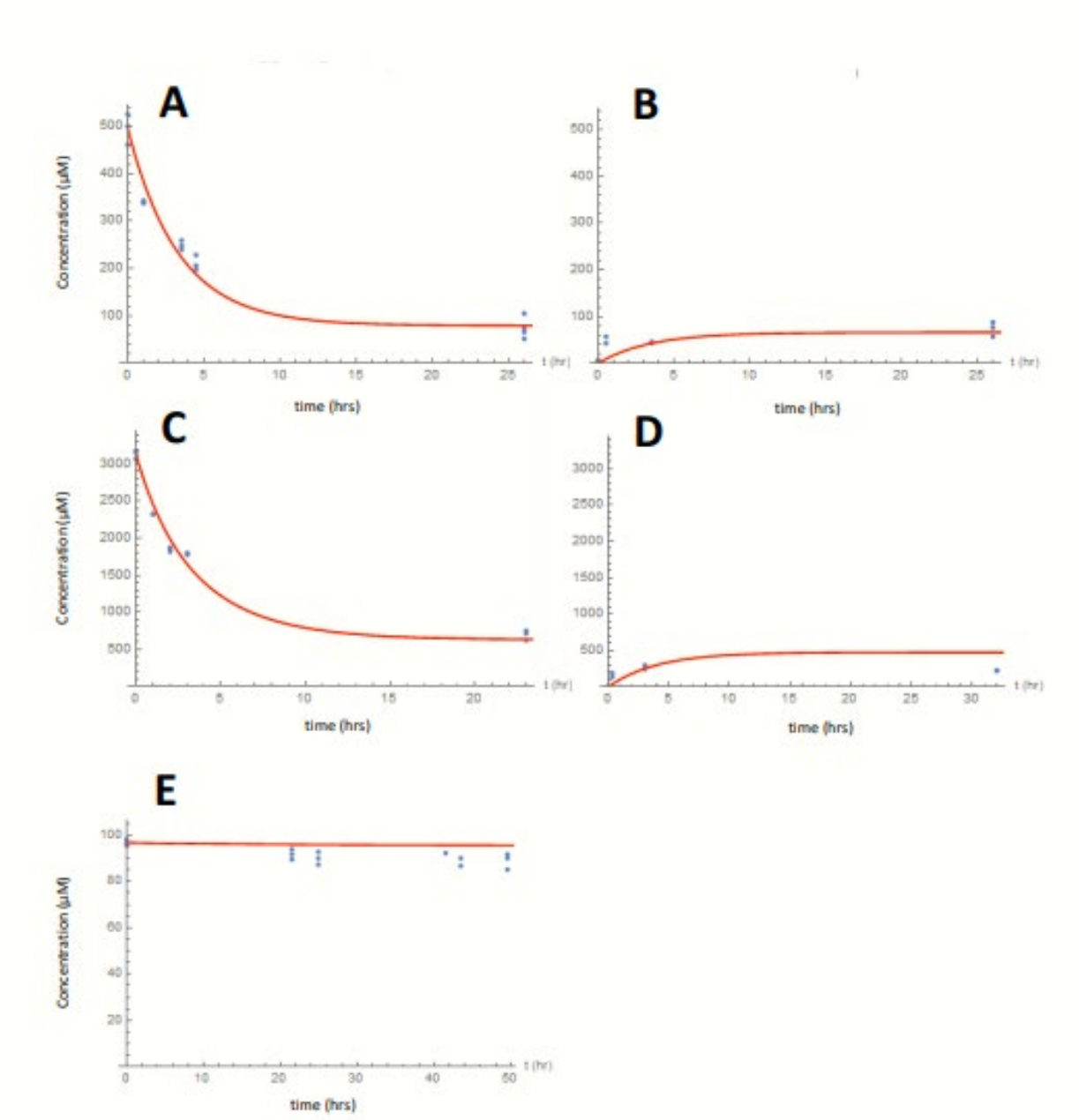

Figure S1: Simultaneous fit of microscopic model for binding kinetics (Equation 2.3) to all bisphenol A experiments. (A, B) Adsorption and desorption, respectively, for 488 μM channel experiment, (C,D) adsorption and desorption for 3000 μM channel experiment and (E) adsorption for disk experiment.

APPENDIX B Supplementary materials for Chapter 3

Supplementary Section S.2

The mathematical formulation for partitioning coefficient

Simulation for disk-soak experiment (Bisphenol A)

Concentration in solution phase = C_s

Concentration in PDMS = C_p

Volume of the PDMS = V_p

$V_p = \pi r^2 h = \pi\,(3)^2\,5\,mm^3 = 141.37 \times 10^{-9}\,m^3$

Volume in the cuvette = V_s

$V_s = 40 \times 10 \times 10 \times 10^{-9}\,m^3 - 141.37 \times 10^{-9}\,m^3 = 3858.63 \times 10^{-9}\,m^3$

Total moles = $N = N_s + N_p = C_s V_s + C_p V_p = C_s V_s + K C_s V_p = (V_s + K V_p)\,C_s$

Let C_s = 97 μM = $97 \times 10^{-3}\,mM = \mathbf{97 \times 10^{-3}\ \frac{mol}{m^3}}$

At t = 48 h, $C_s = 95.9 \times 10^{-3}\ \frac{mol}{m^3}$

Total mole reduction = $(97 - 95.5) \times 10^{-3}\ \frac{mol}{m^3} \times 3858.63 \times 10^{-9}\,m^3 = 5.8 \times 10^{-9}\,mole$

So, at t = 48 h, $C_p = \frac{5.8 \times 10^{-9}\ moles}{141.37 \times 10^{-9}\ m^3} = \mathbf{0.04\ \frac{mole}{m^3}}$

Implementing partitioning coefficient: $C_p = K C_s$

From the above equation: **K = 0.44**

Supplementary Section S.3

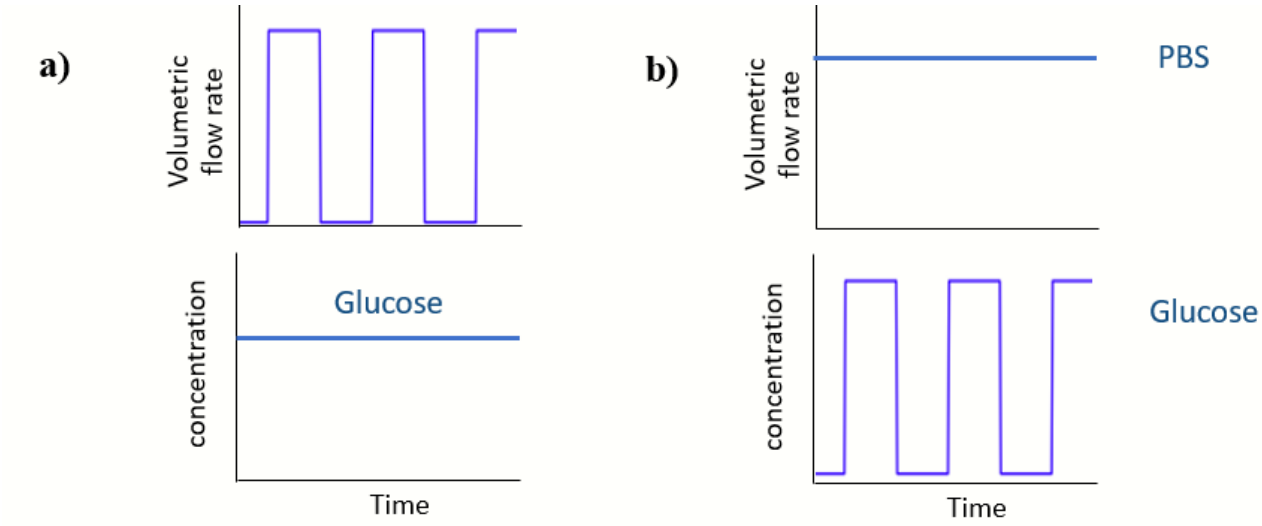

Figure S.3 a) stop flow system with intermittent flow of glucose; b) continuous flow system with continuous flow of PBS buffer and intermittent flow of glucose

Supplementary Section S.4

Table S.4. Modeling the Consumption of Ferricyanide by Upstream µCA Electrode. The upstream microclinical analyzer (µCA) was used to simulate cellular uptake within an organotypic device through the reduction of ferricyanide. A two-µCA setup was used for the experiments, with the upstream µCA simulating an OCM device and the downstream µCA used for quantification. The redox couple of ferricyanide/ferrocyanide was used to simulate consumption/production of metabolites within the upstream system, with the changes then measured at the downstream µCA.

Flow rate (µL/min)	% current reduction due to consumption in upstream µCA					
	Electrode 1		Electrode 2		Electrode 3	
	experimental	modeled	experimental	modeled	experimental	modeled
200	4.0	4.9	3.47	4.91	2.88	4.89
20	16.39	13.22	15.62	15.07	16.16	15.15
2	47.62	37.31	47.10	37.21	--	37.29

Supplementary Section S.5

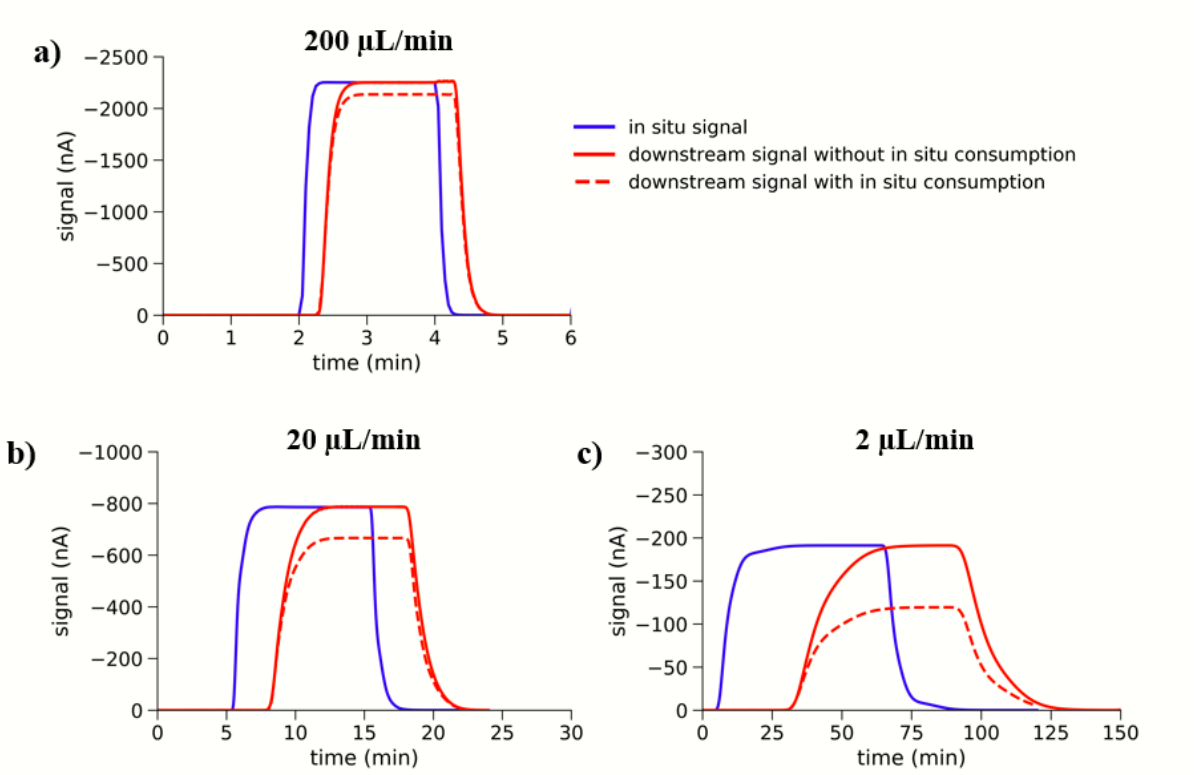

Figure S.5 Simulation of consumption of chemical in upstream µCA and detection using downstream µCA, with continuous flow of ferricyanide at a) 200. b) 20, c) 2 µL/min. Maximum diffusional spread with the maximum current reduction at 2 µL/min

Supplementary Section S.6

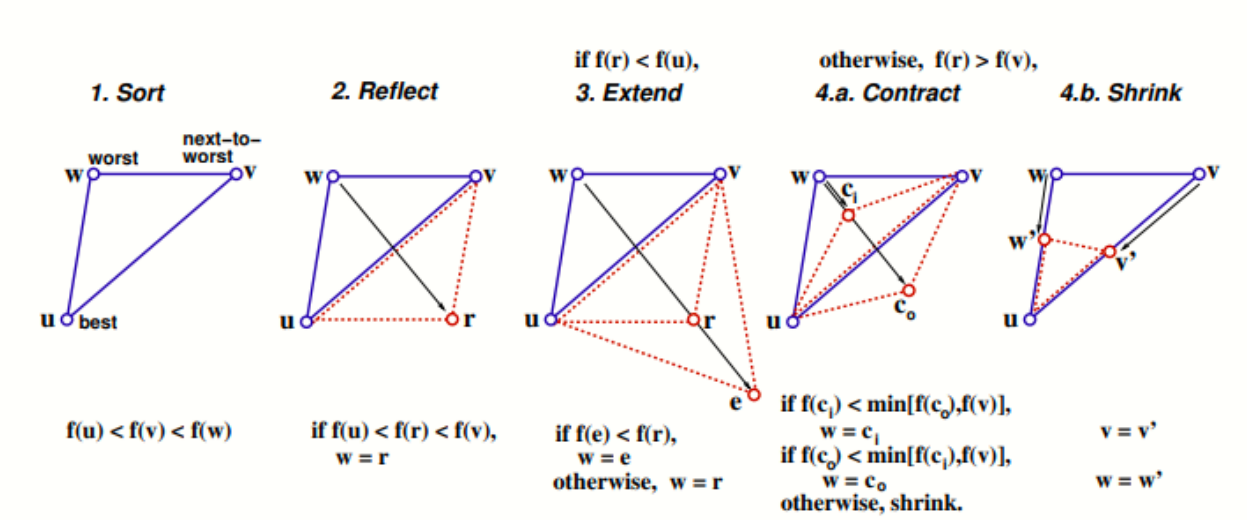

Figure S.6: Illustration of the sequence of steps in one iteration of the Nelder-Mead Simplex method with two parameters (n = 2)[87]

Note: The steps happen in the following order:

- *Reflect* the worst point through the remaining two points.

- If the reflected point is now the second-best point, accept it.

- If the reflected point is now the best point, try *extending* the reflection further.

- If the *extended* point is even better than the reflected point take the extended point. Otherwise, accept the *reflected* point.

- If the reflected point is still the worst performing of the three points, try two *contracted* locations.

- If the better of the contracted locations is now the second-best point, accept the *contracted* point.

- If the contracted locations are still the worst of the three points, *shrink* the simplex.

Supplementary Section S.7

Table S.7 Glucose Parameter Fitting using Nelder-Mead Simplex Method

Trials		Km	Vmax	Function: Sum of Squared Residual (SSR)	avg of function	% change from average
initial	worst	30	1.5	1859829	970489	-91.6383
	next-to-worst	25	1.7	645072		33.53124
	best	25	1.5	406566		58.1071
1	worst	27.5	1.5	982696	552389.3	-77.8992
	next-to-worst	25	1.5	406566		26.39865
	best	25	1.6	267906		51.50051
2	worst	25	1.5	406566	315082.3	-29.0348
	next-to-worst	24.17	1.57	270775		14.06214
	best	25	1.6	267906		14.9727
3	worst	24.17	1.57	270775	263588.7	-2.72634
	next-to-worst	25	1.6	267906		-1.63791
	best	24.72	1.56	252085		4.364249
4	worst	25	1.6	267906	258963	-3.45339
	next-to-worst	25.55	1.59	256898		0.797411
	best	24.72	1.56	252085		2.655978
5	worst	25.55	1.59	256898	253708.7	-1.25708
	next-to-worst	25.09	1.583	252143		0.617112
	best	24.72	1.56	252085		0.639973
6	worst	25.09	1.583	252143	251980.7	-0.06442
	next-to-worst	24.72	1.56	252085		-0.04141
	best	**24.69**	**1.565**	251714		0.105828

Supplementary Section S.8

Table S.8 Lactate Parameter Fitting using Nelder-Mead Simplex Method

Trials		Km	Vmax	Function	Error
initial	worst	0.6	0.282921	11811.13	4127.365
	next-to-worst	0.67	0.282921	14924.71	
	best	0.6	0.273795	8558.645	
1	worst	0.615	0.279	9598.033	1971.774
	next-to-worst	0.6	0.28	11811	
	best	0.6	0.274	8558	
2	worst	0.60375	0.278	9196.278	704.509
	next-to-worst	0.615	0.279	9598	
	best	0.6	0.274	8558	
3	worst	0.6	0.274	8558	1150.64
	next-to-worst	0.60375	0.278	9196.28	
	best	0.58	0.2715	7504.512	
4	worst	0.58	0.2715	7504.51	1195.337
	next-to-worst	0.6	0.274	8558	
	best	0.5625	0.26225	6665.317	
5	worst	0.5625	0.26225	6665.317	2539.284
	next-to-worst	0.58	0.2715	7504.51	
	best	0.51375	0.252625	4003.374	
6	worst	0.517	0.25	5181.85	1680.749
	next-to-worst	0.5625	0.26225	6665.317	
	best	0.51375	0.252625	4003.374	
7	worst	0.51375	0.252625	4003.374	2184.763
	next-to-worst	0.517	0.25	5181.85	
	best	0.42	0.232	1982.52	
8	worst	0.417	0.233	2174.44	1171.99
	next-to-worst	0.51375	0.252625	4003.374	
	best	0.42	0.232	1982.52	
9	worst	0.419	0.2325	2066.22	120.8842
	next-to-worst	0.417	0.233	2174.44	
	best	0.42	0.232	1982.52	

Supplementary Section S.9

Table S.9 Glutamate Parameter Fitting using Nelder-Mead Simplex Method

Trials		Km	Vmax	Function
initial	worst	5.3	0.257201	14037.26
	next-to-worst	5.3	0.231481	1956.564
	best	5	0.231481	824.9467
1	worst	5.15	0.244	4927.45
	next-to-worst	5.15	0.231	878.43
	best	5	0.231	824.95
2	worst	5.15	0.231	878.43
	next-to-worst	5.1	0.234	844
	best	5	0.231	824.95
3	worst	5.1	0.234	844
	next-to-worst	5	0.231	824.95
	best	5.08	0.232	674.74
4	worst	5.08	0.232	675
	next-to-worst	4.98	0.229	593.5
	best	4.86	0.224	582.64